

DEVELOPMENT AND ASSESSMENT OF POLARIZED HEAD MOUNTED
PROJECTION DISPLAYS

by

Rui Zhang

A Dissertation Submitted to the Faculty of the

COLLEGE OF OPTICAL SCIENCES

In Partial Fulfillment of the Requirements
For the Degree of

DOCTOR OF PHILOSOPHY

In the Graduate College

THE UNIVERSITY OF ARIZONA

2010

THE UNIVERSITY OF ARIZONA
GRADUATE COLLEGE

As members of the Dissertation Committee, we certify that we have read the dissertation prepared by Rui Zhang

entitled DEVELOPMENT AND ASSESSMENT OF POLARIZED HEAD MOUNTED PROJECTION DISPLAYS

and recommend that it be accepted as fulfilling the dissertation requirement for the

Degree of Doctor of Philosophy

_____ Date: May 5, 2010
Hong Hua

_____ Date: May 5, 2010
Russell Chipman

_____ Date: May 5, 2010
Harrison Barrett

_____ Date:

_____ Date:

Final approval and acceptance of this dissertation is contingent upon the candidate's submission of the final copies of the dissertation to the Graduate College.

I hereby certify that I have read this dissertation prepared under my direction and recommend that it be accepted as fulfilling the dissertation requirement.

_____ Date: June 17, 2010
Dissertation Director: Hong Hua

STATEMENT BY AUTHOR

This dissertation has been submitted in partial fulfillment of requirements for an advanced degree at the University of Arizona and is deposited in the University Library to be made available to borrowers under rules of the Library.

Brief quotations from this dissertation are allowable without special permission, provided that accurate acknowledgment of source is made. Requests for permission for extended quotation from or reproduction of this manuscript in whole or in part may be granted by the head of the major department or the Dean of the Graduate College when in his or her judgment the proposed use of the material is in the interests of scholarship. In all other instances, however, permission must be obtained from the author.

SIGNED: Rui Zhang

ACKNOWLEDGMENT

I am deeply grateful to my advisor Dr. Hong Hua for her over 5 year's mentorship. When I started to work in Dr. Hua's group, my academic background was mainly in Physics. Dr. Hua introduced me into the field of optical engineering and three dimensional displays. She gave me the opportunity to work on a challenging and interesting project, development and assessment of a polarized head mounted projection displays, which is also the work covered in this dissertation. In every stage of the project, Dr. Hua showed great patience and inspired me to explore new solutions and make new findings. I really enjoyed working with Dr. Hua. Undoubtedly, what I have learned from Dr. Hua will benefit me through my whole career.

I appreciate the help from others members of my dissertation committee, Dr. Russell Chipman and Dr. Harry Barrett. Both professors reviewed my dissertation carefully and provided me lots of comments and suggestions, which is a great help to my work and my writing.

I would also thank my lab colleagues I have been working with, Craig, Sheng, Nick, Lennie, Dewen, Chunyu, Sang Yoon, Xinda, Ji-young, Xiaorui and Zhenrong for their help to my work. It was also great fun to work with them.

Finally, I express my sincere gratitude to my family for their unconditional love and support in every step of my life. Without their support and encouragement, I would not have done this.

TABLE OF CONTENTS

LIST OF FIGURES.....	9
LIST OF TABLES	13
ABSTRACT	14
CHAPTER 1 INTRODUCTION.....	16
1.1 MOTIVATION AND PROBLEM STATEMENT.....	16
1.2 OVERVIEW OF THE WORK IN THE DISSERTATION.....	19
1.3 ORGANIZATION OF THE DISSERTATION.....	21
CHAPTER 2 BACKGROUND.....	23
2.1 HUMAN VISUAL SYSTEM.....	23
2.2 OVERVIEW OF HEAD MOUNTED DISPLAYS.....	25
2.2.1 HMD designs.....	25
2.2.2 Classifications of HMD systems.....	28
2.3 HEAD MOUNTED PROJECTION DISPLAYS.....	30
2.4 POLARIZED HEAD MOUNTED PROJECTION DISPLAYS.....	34
2.5 APPLICATIONS OF HMPD TECHNOLOGIES.....	36
2.6 SUMMARY.....	38
CHAPTER 3 POLARIZATION CHARACTERIZATION IN A P-HMPD	39
3.1 POLARIZATION REPRESENTATION.....	39
3.1.1 Stokes vector.....	39
3.1.2 Mueller matrix.....	41
3.1.3 Mueller matrix decomposition.....	41
3.2 POLARIZATION ELEMENTS IN THE P-HMPD SYSTEM.....	43
3.2.1 Selection of retarder.....	44
3.2.2 Selection of PBS.....	46
3.3 MEASUREMENT METHOD.....	47
3.3.1 Axometrics polarimeter.....	47
3.3.2 Experimental setup.....	48
3.4 EXPERIMENTAL RESULTS.....	51
3.4.1 PBS and beamsplitters.....	51
3.4.2 Retarder.....	56
3.4.3 Retroreflective screen.....	56
3.5 Analysis of overall system performance.....	60

3.5.1	Luminous transfer efficiency.....	61
3.5.2	Uniformity.....	63
3.5.3	Contrast.....	64
3.5.4	Colorimetric characteristics.....	65
3.6	SUMMARY.....	66
CHAPTER 4 DESIGN OF A P-HMPD SYSTEM USING FLCOS MICRODISPLAYS.....		68
4.1	SELECTION OF MICRODISPLAYS.....	68
4.2	SYSTEM DESIGN OVERVIEW.....	71
4.3	DESIGN OF AN ILLUMINATION UNIT.....	73
4.3.1	Light source and source modeling.....	73
4.3.2	Light engine designs.....	75
4.3.2.1	Design I: Double telecentric design.....	76
4.3.2.2	Design II: Image space telecentric design.....	80
4.3.2.3	Further analysis of Design II.....	86
4.4	DESIGN OF A PROJECTION LENS.....	89
4.4.1	Lens specification.....	89
4.4.2	Lens design and optimization.....	91
4.4.2.1	Starting point.....	91
4.4.2.2	Optimization process.....	93
4.4.3	Performance analysis of the projection lens.....	96
4.4.3.1	DOE efficiency.....	97
4.4.3.2	System performance in the microdisplay space.....	98
4.4.3.3	Tolerance analysis.....	100
4.5	TESTING OF THE PROJECTION LENS.....	102
4.5.1	MTF testing of the lens.....	102
4.5.2	Polarization measurement of the plastic lens.....	102
4.6	P-HMPD PROTOTYPE AND ITS PERFORMANCE.....	112
4.7	SUMMARY.....	116
CHAPTER 5 CALIBRATION OF A P-HMPD.....		117
5.1	COLOR CALIBRATION.....	117
5.1.1	Mathematical model.....	117
5.1.2	Colorimetric characterization.....	119
5.1.3	Model evaluation.....	124
5.2	CALIBRATION OF THE FOCUSING PLANE.....	125
5.3	GEOMETRICAL CALIBRATION.....	128
5.4	SUMMARY.....	134
CHAPTER 6 IMAGING PROPERTIES OF A RETROREFLECTIVE SCREEN.....		135
6.1	INTRODUCTION.....	135

6.2	RELATED WORK.....	136
6.3	BASIC PROPERTIES OF A SINGLE CCR.....	138
6.3.1	Geometrical imaging properties of a single CCR.....	138
6.3.2	Effective area of a CCR.....	140
6.3.3	Diffraction pattern of a CCR.....	143
6.4	IMAGING PROPERTIES OF A CCR ARRAY BASED RETROREFLECTIVE SCREEN.....	148
6.4.1	Geometrical imaging effect.....	150
6.4.2	Diffraction pattern of a retroreflective screen.....	154
6.5	IMAGE RESOLUTION OF A RETROREFLECTIVE SCREEN IN AN HMPD SYSTEM.....	157
6.5.1	Image resolution analysis method.....	157
6.5.2	Image resolution calculation.....	162
6.5.3	Tolerance distance in an HMPD.....	166
6.5.4	Optimization of the corner cube size.....	168
6.6	SUMMARY.....	168
CHAPTER 7 ASSESSMENT OF A P-HMPD SYSTEM.....		170
7.1	ASSESSMENT OF PERCEIVED SPATIAL RESOLUTION.....	170
7.1.1	Introduction.....	170
7.1.2	Related work.....	172
7.1.3	Experimental design.....	173
7.1.3.1	Visual stimuli design.....	174
7.1.3.2	Variables and hypotheses.....	176
7.1.3.3	Subject.....	179
7.1.3.4	Experiment procedure.....	179
7.1.3.5	Experiment setup.....	179
7.1.3.6	Scoring method.....	180
7.1.4	Results and discussion.....	182
7.1.5	Summary.....	188
7.2	DEPTH PERCEPTION ASSESSMENT.....	189
7.2.1	Introduction.....	189
7.2.2	Contributing factors to depth perception accuracy.....	190
7.2.2.1	Depth cues.....	191
7.2.2.2	Stereoacuity.....	192
7.2.2.3	Display pixel resolution.....	193
7.2.2.4	IPD mismatch.....	194
7.2.3	Depth perception assessment methods.....	196
7.2.4	Experiment design.....	198
7.2.4.1	Experiment task.....	198
7.2.4.2	Variables.....	199
7.2.4.3	Experiment setup.....	201
7.2.4.4	System calibration.....	203
7.2.4.5	Subject.....	206

	7.2.4.6	Test procedure.....	205
	7.2.5	Result analysis and discussion.....	206
		7.2.5.1 Overall performance.....	207
		7.2.5.2 Effect of the retroreflective screen.....	209
	7.2.6	Discussion.....	213
	7.2.7	Summary.....	215
CHAPTER 8		CONCLUSIONS AND SUGGESTIONS OF FUTURE WORK.....	216
	8.1	CONCLUSIONS.....	216
	8.2	SUGGESTIONS OF FUTURE WORK.....	217
APPENDIX A		CALCULATION OF THE EFFECTIVE AREA OF A CCR.....	219
REFERENCE.....			229

LIST OF FIGURES

Figure 1.1	Proof-of-concept demonstration for medical training applications using an HMPD.....	17
Figure 2.1	Monocular schematic setup of (a) an immersive HMDs and (b) optical STHMD using eyepiece type optics.....	29
Figure 2.2	Monocular schematic design of an HMPD.....	31
Figure 2.3	Natural occlusion of the computer-generated object (bone) by the real object (hand) through an HMPD.....	33
Figure 2.4	(a) First-generation HMPD prototype and (b) Second-generation HMPD prototype.....	34
Figure 2.5	Schematic design of a polarized HMPD.....	36
Figure 2.6	(a) Dimensions for the SCAPE (b) Setups for the SCAPE.....	37
Figure 2.7	(a) Sample view for the workbench applications; (b) Sample view through the surrounding wall display.....	38
Figure 3.1	Schematic design of a p-HMPD system.....	44
Figure 3.2	Structure of a wire-grid PBS.....	46
Figure 3.3	Schematic structure of Axometrics polarimeter.....	48
Figure 3.4	Polarimeter setup for polarization measurements of (a) Transmittance of a retarder; (b) Transmittance of a PBS or a beamsplitter; (c) Reflectance of a PBS or a beamsplitter; and (d) Retroreflectance of a retroreflective screen.....	50
Figure 3.5	Characterizing the PBS: (a) Reflectance of S-polarized light; (b) Transmittance of P-polarized light.....	52
Figure 3.6	Characterizing a beamsplitter: (a) Reflectance and (b) Transmittance of S-polarized light; and (c) Reflectance and (d) Transmittance of P-polarized light.....	54
Figure 3.7	Characterizing a retarder: (a) Transmittance; (b) Retardance; and (c) Fast-axis direction.....	55
Figure 3.8	Normalized Mueller matrix plot for the retroreflection of a retroreflective screen at the wavelength of 550nm. The incident angle is from -28° to 28°	57
Figure 3.9	Diattenuation of a retroreflective screen.....	58
Figure 3.10	Retardance of a retroreflective screen.....	59
Figure 3.11	Depolarization index versus incident angles.....	60
Figure 3.12	Luminance efficiency of a p-HMPD and a non-polarizing HMPD at the wavelength of (a) 450nm (b) 550nm and (c) 650nm. (d) The ratio of the luminance efficiency of a p-HMPD to an HMPD.....	64
Figure 4.1	(a) Photos of a 0.5" Alphasight LED illuminator (b) Structure of the LED illuminator (Courtesy of Teledyne)	74
Figure 4.2	Angular distribution of the light as a function of angle.....	74
Figure 4.3	Design I: Double telecentric design of a light engine for an FLCOS microdisplay.....	76

LIST OF FIGURES—Continued

Figure 4.4	Illuminance distribution on the microdisplay for design I.....	80
Figure 4.5	Luminance distribution of the LED illuminator as a function of emission angle.....	80
Figure 4.6	Schematic design of the light engine design II.....	81
Figure 4.7	Simplified optical setup of the light engine design II.....	81
Figure 4.8	Tapered light pipe with mirrors: (a) Schematic design and (b) Prototype picture.....	84
Figure 4.9	Effects of the mirror tilt angle on the (a) Non-uniformity and (b) Optical efficiency of the light engine.....	85
Figure 4.10	Effects of the mirror length on the (a) Non-uniformity and (b) Optical efficiency of the light engine.....	86
Figure 4.11	Simulated illuminance distribution on the display (a) Without light pipe and (b) With the light pipe.....	86
Figure 4.12	Reduced contrast due to polarization leakage in the light engine.....	88
Figure 4.13	Layout of the starting patent lens.....	92
Figure 4.14	Starting lens: (a) Layout and (b) MTF performance.....	93
Figure 4.15	Intermediate compact design: (a) Layout and (b) MTF performance.....	95
Figure 4.16	Layout of the final design of a projection lens.....	97
Figure 4.17	(a) Diffraction efficiency versus radius and (b) diffraction efficiency versus wavelength.....	98
Figure 4.18	Lens performance of the optimized design: (a) spot diagram; (b) rayfan plot; (c) longitudinal spherical aberration, astigmatism and distortion; and (d) MTF performance.....	100
Figure 4.19	Cumulative probability plot for MTF tolerance.....	101
Figure 4.20	Prototype of the projection lens.....	101
Figure 4.21	Measured MTF performance of the lens prototype for a set of tangential fields.....	102
Figure 4.22	Polarization measurement setup of the projection lens for (a) the on-axis field and (b) the off-axis field.....	105
Figure 4.23	Simplified drawing of the propagation of the polarized light through the projection lens in a p-HMPD.....	108
Figure 4.24	Average optical efficiency of Lens I as a function of rotation angle at five representative field angles for the wavelength of (a)450nm, (b)550nm and (c)650nm, respectively.....	108
Figure 4.25	Average optical efficiency of Lens II as a function of rotation angle at five representative field angles for the wavelength of (a)450nm, (b)550nm and (c)650nm, respectively.....	109
Figure 4.26	Simplified drawing of the propagation of the polarized light through the projection lens with an HWR.....	111
Figure 4.27	Optical efficiency of Lens II as a function of rotational angle α at the wavelength of (a)450nm, (b)550nm and (c)650nm after an HWR with its fast axis at 55° was added.....	112

LIST OF FIGURES—Continued

Figure 4.28	Design of a compact p-HMHD prototype: (a) Overall optical layout of the system; (b)-(c) side and front views of the p-HMPD prototype.....	114
Figure 4.29	Photos of the pupil through a p-HMPD prototype type: (a) is taken in a darker environment with longer exposure time and (b) was taken at a brighter environment with shorter exposure time.....	115
Figure 5.1	Color gamuts for (a) the left-eye display and (b) the right-eye display.....	121
Figure 5.2	Tone response curves for R, G, B channels.....	123
Figure 5.3	Nikon D40 on a Tripod was used to capture the image through a p-HMPD.....	126
Figure 5.4	Pictures of a part of ISO 12233 chart when the chart was (a) 102cm, (b)100cm, (c) 98cm and (d) 96cm away from the camera.....	128
Figure 5.5	(a) HiBall IR sensor and (b) HiBall tracker.....	129
Figure 5.6	Simplified view of the image formation in a p-HMPD.....	129
Figure 5.7	EVP coordinate in a p-HMPD system.....	130
Figure 5.8	(a) Image of the checkerboard from the p-HMPD (b) Image of a Real checkerboard captured by a video camera.....	132
Figure 5.9	Experiment setup to capture pictures through p-HMPD.....	133
Figure 6.1	Three types of reflection (a) Diffusing surface, (b) Specular surface (c) Retroreflective surface.....	135
Figure 6.2	Photo of a micro CCR based retroreflective screen.....	136
Figure 6.3	Ray tracing in a corner cube reflector.....	138
Figure 6.4	Effective aperture of a CCR for a normal incident angle.....	142
Figure 6.5	(a) (θ, φ) is defined in the X'Y'Z' coordinate (b) The ratio of the area of the effective aperture to the area of the physical aperture as a function of θ and φ	143
Figure 6.6	Diffraction retroreflected light through a CCR.....	144
Figure 6.7	Diffraction pattern of a CCR for normal incident light.....	147
Figure 6.8	Imaging effect of a CCR array when the object plane coincides with the aperture plane of the CCR array ($ d =0$).....	149
Figure 6.9	Illustration of geometrical imaging effect through a CCR array in a 2D plane.....	151
Figure 6.10	(a) Simulation setup in LightTools® (b) a microscopic image of a CCR array.....	155
Figure 6.11	Amplitude distribution on the object plane (a) through the a retroreflective screen (b) through a single CCR.....	156
Figure 6.12	Simplified view of an HMPD/p-HMPD setup.....	158
Figure 6.13	Imaging by a corner cube array when $ d >d_0$	158
Figure 6.14	Angular resolution at the project image distance z_i of 1m as a function of the distance d and the ray bundle size (RBD) when the corner cube size is equal to (a) 100 μ m and (b) 200 μ m.....	164

LIST OF FIGURES—Continued

Figure 6.15	Angular resolution at the project image distance z_i of 2m as a function of the distance d and the ray bundle size (RBD) when the corner cube size is equal to (a) 100 μ m and (b) 200 μ m.....	164
Figure 6.16	Angular resolution at the project image distance z_i of 4m as a function of the distance d and the ray bundle size (RBD) when the corner cube size is equal to (a) 100 μ m and (b) 200 μ m.....	165
Figure 7.1	Revised Landolt C stimulus in four directions.....	175
Figure 7.2	Eight revised British Standard Institution optotypes.....	176
Figure 7.3	Simplified setup of p-HMPD.....	176
Figure 7.4	Mean VA scores at (a) the contrast of 1 and (b) the contrast of 0.5 using the threshold curve method.....	184
Figure 7.5	Mean VA scores at (a) the contrast of 1 and (b) the contrast of 0.5 using the letter-by-letter method.....	184
Figure 7.6	Results of the threshold curve method for positions 3 and 2.....	185
Figure 7.7	Depth perception error caused by pixel resolution.....	194
Figure 7.8	Depth perception error caused by IPD mismatch.....	195
Figure 7.9	Perceived depth errors related with binocular disparity.....	196
Figure 7.10	(a) Test session 1 for arm length setup (b) Test session 2 for mid-range setup.....	201
Figure 7.11	(a) Experiment setup and (b) Example view through one side of the display: a virtual sphere and a real cylinder.....	202
Figure 7.12	Calibration setup.....	204
Figure 7.13	Judged distance as a function of reference object distance (a) when $z_i=1$ m and (b) when $z_i=2$ m.....	208
Figure 7.14	Standard deviation of judged distance as a function of real object distance (a) when $z_i=1$ m and (b) when $z_i=2$ m.....	209
Figure 7.15	Distance ratio as a function of reference object distance (a) when $z_i=1$ m and (b) when $z_i=2$ m.....	209
Figure 7.16	(a) Signed error and (b) Standard deviation as a function of real object distance when $z_i=1$ m (RR: Retroreflective screen).....	211
Figure 7.17	(a) Signed error and (b) Standard deviation as a function of reference object distance (RR: Retroreflective screen).....	213

LIST OF TABLES

Table 3.1	Uniformity and image contrast: HMPD vs. p-HMPD.....	65
Table 3.2	Colorimetric characteristics: HMPD vs. p-HMPD.....	66
Table 4.1	Properties of microdisplays for HMDs.....	69
Table 4.2	Specifications of the microdisplay and LED illuminator.....	75
Table 4.3	First-order data of the light design.....	78
Table 4.4	Percent of luminance from LED directly.....	88
Table 4.5	Percent of luminance through the microdisplay.....	88
Table 4.6	Specification of the projection lens.....	91
Table 4.7	Estimated errors in the fabrication.....	101
Table 5.1	Color calibration errors for left-eye display over 3x3x3 test patches.....	124
Table 6.1	Ray tracing results for six possible optical paths.....	140
Table 6.2	Simulation results: geometrical imaging effect of a retroreflective screen.....	154
Table 7.1	Eight positions of the retroreflective screen.....	177
Table 7.2	Mean and standard deviation (SD) of visual acuity scores obtained from eight participants (the unit is in arcmin).....	183
Table 7.3	Tukey Grouping results for (a) contrast=1 and (b) contrast=0.5.....	187
Table 7.4	ANOVA results at different reference object distances.....	210

ABSTRACT

Head mounted projection display (HMPD) technology, as an alternative to conventional head mounted displays (HMD), offers a potential of designing wide field-of-view (FOV), low distortion optical see-through HMDs (OST-HMDs). Existing HMPD designs, however, suffer from problems of low luminance and low image resolution, which limits the applications of such information displays for the scenarios which require high luminance and high image fidelity. The design of a polarized head mounted projection display (p-HMPD) was recently proposed to overcome the challenge of low luminous efficiency in existing HMPD designs. Polarization management was employed to reduce the light loss caused by beamsplitting in an HMPD.

The work in this dissertation focuses on the development and evaluation of an SXGA resolution, high efficiency p-HMPD system. The main contributions are as follows. First, the key elements in the polarization management scheme of a p-HMPD were selected and their polarization performances were characterized by measuring their Mueller matrices, based on which the overall display performance of a p-HMPD was analyzed.

Second, based on a pair of ferroelectric liquid-crystal-on-silicon (FLCoS) microdisplays, a compact illumination unit and a light-weight projection system were designed, from which a p-HMPD prototype was built. Following the prototype implementation, a series of calibrations were performed to obtain correct color presentation, desired focusing setting, and optical system characteristics necessary for

achieving accurate registration between virtual objects and their counterparts in the real world.

Third, the imaging properties of a retroreflective screen which is an essential part of a p-HMPD or HMPD were studied and its effects on the image resolution of an HMPD system were further characterized.

Finally, the performance of the system was evaluated through two objective user experiments, including a visual acuity assessment and a depth perception accuracy assessment.

CHAPTER 1

INTRODUCTION

1.1 MOTIVATION AND PROBLEM STATEMENT

Mixed- and augmented reality (MR-AR) technology seeks to selectively supplement, rather than replace, a user's sensory perceptions of the physical world with computer-generated digital information. A wide range of applications has been explored and examples include training and education, medical diagnosis and surgery planning, and scientific visualization (Azuma 1997; Rolland *et al.* 1997).

Among different display technologies used for MR-AR systems, optical see-through head mounted display (OST-HMD) is one of basic approaches by optically combining computer-generated images with real-world scenes through an optical combiner interface such as a beamsplitter. The optical see-through approach allows a user to see the real world without degradation of image resolution and thus is “preferred for tasks where hand-eye coordination or non-blocked real-world view is critical” (Hua, 2006).

Conventionally, eyepiece-type optics is used as the viewing optics in most of such display designs. A head mounted projection display (HMPD) was proposed as an alternative technology to conventional OST-HMDs and CAVE-like projection displays (Cruz-Neira *et al.* 1993). In the HMPD technology, a projection lens is used to replace the eyepiece optics and a retroreflective screen is used instead of a diffusing screen. The key benefits of an HMPD, compared with a conventional OST-HMD, include the capability

of designing wide field-of-view displays with low distortion and achieving natural occlusion of a virtual object by the real object placed between the user and the retroreflective material (Hua *et al.* 2000).

Various applications based on HMPD systems have been explored. Figure 1.1 shows an experimental setup for a proof-of-concept demonstration for medical training applications (Brown & Hua, 2006; Hua, 2006). As shown in Figure 1.1, a live person, covered with a retroreflective screen, lies on a workbench. Through an HMPD, a user is able to view a virtual 3D skeleton model overlaid with a real human body.



Figure 1.1 Proof-of-concept demonstration for medical training applications using an HMPD (Brown & Hua, 2006)

However, as you may notice from the photograph in Figure 1.1, the low image brightness yielded by an HMPD system (Hua *et al.* 2004) imposes significant restrictions on the lighting conditions of the working environment, and eliminates the application scenarios where well illuminated environments are required. In a well-illuminated physical environment, the details in the display's low-brightness images would be washed out, making them hard or even impossible to discern. In fact, it has been a

common problem in OST-HMDs that the displayed images suffer low brightness and low contrast compared with the direct view of the real world. The problem is worsened in HMPDs due to multiple beamsplitting, low luminance of the image source and the relatively low retroreflectivity of available retroreflective screens. In the existing designs of HMPD systems, the overall transfer efficiency of the luminance is approximately 4% or lower. For instance, using a typical miniature backlit active matrix liquid crystal display (AMLCD) as the image source, the luminance of the image observed through an HMPD is about 4cd/m^2 , while the average luminance of a well-lit indoor environment is over 100cd/m^2 . As a result, the low-brightness image will appear washed out in such well-lit environments. In fact, like most OST-HMDs, HMPD typically has to be operated under a dimmed lighting condition. The low brightness limits the feasibility of applying such information displays outdoor or in well-lit environments.

Another challenge of existing HMPD systems is the low image resolution. This problem is basically associated with the resolution of the microdisplay, the magnification and resolvability of the projection optics, and the resolvability of the retroreflective screen. In the existing HMPDs, the limited resolution of the LCD microdisplay becomes a major constraint of the overall system, which limits the applications of an HMPD from scenarios which require high image fidelity, such as medical diagnosis.

Furthermore, previous efforts in designing and evaluating HMPD systems mostly neglected the image quality degradation caused by the imaging artifacts of the retroreflective screen. Our experience shows that the image resolution of an HMPD can be further degraded by the retroreflective screen. Thus, it is critical to understand the

image properties of a retroreflective screen and provide guidance on the HMPD design and the system setup of the HMPD application.

1.2 OVERVIEW OF THE WORK IN THE DISSERTATION

To address the problem of high light loss due to multiple beamsplitting in HMPD systems and to develop a display technology that yields higher illumination efficiency which can be used in well-illuminated working environments, a polarized head-mounted projection display (p-HMPD) scheme was previously proposed (Hua and Gao 2005, 2007). By carefully manipulating the polarization states of the light propagating through the system, a p-HMPD can potentially be three times brighter than a traditional non-polarized HMPD design using the same microdisplay technology.

The overall objective of my work is to develop a high performance p-HMPD system with improved brightness, contrast, resolution, and color representation compared with the older prototypes. The rest of this section will briefly introduce the work that has been done in this dissertation to reach the objective.

First, one of the main challenges in designing a high-performance p-HMPD system lies in the polarization management in a wide FOV and broadband system. The performance of polarization elements used in a p-HMPD, such as polarizing beamplitters (PBS) and quarter wave retarders, may have significant variation across the FOV and the visible spectrum. After selecting the best available polarization elements, we characterize the properties of each polarization element by measuring their Mueller matrices and also examine how their angular and chromatic variations affect the system performances.

Such evaluation and analysis help to guide the next-step optical designs for the display system.

Second, in order to build a high performance system it is critical to select the best available microdisplay technology. In the new p-HMPD prototype, a Ferroelectric Liquid Crystal on Silicon (FLCoS) microdisplay is selected as the image source of the system. The new FLCoS reflective microdisplay has an optical efficiency of 60% and image resolution of 1280x1024, and it shows much better performance than the Active Matrix LCD (AMLCD) microdisplay used in our previous prototypes, which has an optical efficiency of lower than 10% and image resolution of 640x480. The use of FLCoS reflective microdisplay brings new challenges to the design of two key optical parts of a p-HMPD, an illumination unit for the microdisplays and a projection lens, both of which require high compactness and high performance. After designing these two optical sub-systems, a p-HMPD prototype is fabricated and assembled in the lab. A series of calibrations are performed on the prototype to obtain correct color and depth rendering as well as focus setting.

Third, as an essential part of an HMPD system, the retroreflective screen plays an important role on the overall image quality. The imaging properties of a retroreflective screen, including geometrical imaging effect and diffraction effect, are examined, and their effects on the image resolution of a p-HMPD system are further analyzed. Based on these effects, we establish the movement range of a p-HMPD user from a retroreflective screen, within which the image resolution degradation caused by a retroreflective screen may be neglected. This knowledge is particularly useful for guiding the configuration of

an HMPD/p-HMPD system to meet different application needs.

Finally, the performance of the system is evaluated as a whole through two objective user experiments, including a visual acuity assessment and a depth perception accuracy assessment.

1.3 ORGANIZATION OF THE DISSERTATION

The rest of my dissertation is organized as follows.

Chapter 2 gives a brief overview of human factors and engineering factors in the design of head mounted displays. The schematic designs of an HMPD and a p-HMPD are introduced in details. Furthermore, the applications of HMPDs are reviewed.

Chapter 3 focuses on the polarization management in a p-HMPD system. The polarization elements are characterized and the overall display performance is analyzed based on the polarization measurement.

Chapter 4 presents the design of a p-HMPD prototype based on the selection of Ferroelectric Liquid Crystal on Silicon (FLCoS) microdisplays. The design and evaluation of an illumination unit and a projection lens, which are two key parts of the system, are described in details.

Chapter 5 summarizes the methods for color calibration, focusing distance calibration and geometrical calibration of a p-HMPD.

Chapter 6 analyzes the imaging properties of a retroreflective screen. Both the geometrical blur and far field diffraction blur of a retroreflective screen are analyzed. The image resolution of a retroreflective screen in a p-HMPD is analyzed using a numerical

method.

Chapter 7 focuses on the objective user assessments of a p-HMPD system. Two tests have been performed. The first test evaluates the resolution performance of a p-HMPD using visual acuity test while the second test evaluates the depth perception accuracy of a p-HMPD.

CHAPTER 2

BACKGROUND

This Chapter provides the background related to the subjects of this dissertation. I will start with a brief summary of the human visual system (HVS) pertinent to HMD systems, followed by an overview of HMD systems. Then the schematic designs of a head mounted projection display (HMPD) and a polarized HMPD (p-HMPD) are introduced and the applications of HMPDs are briefly summarized.

2.1 HUMAN VISUAL SYSTEM

Being the last component in the image chain of a display system, the human visual system (HVS) perceives the images generated through an HMD, and therefore its visual and anatomical properties play critical roles in both design and visual assessment of HMDs (Rolland & Hua, 2005). In this section, the human visual system pertinent to the design of HMD systems is reviewed in terms of its field of view (FOV), visual acuity, the spectral response, the pupil size, and stereoacuity.

The eye's line of sight connects the fixation point of the eye to the center of the entrance pupil, and the center of the exit pupil to the fovea (Schwiegerling, 2004). On average the FOV of a single, stationary eye is 160° in the horizontal direction and 120° in the vertical direction. With two eyes, the overall FOV is approximately 120° vertically and 200° horizontally when the eyes are stationary. With the rotation of eyes, the overall

FOV is about 290° horizontally. The binocular FOV, within which an object is visible to both eyes and stereo vision is available, is about 114° when the eyes converge symmetrically.

The visual acuity is a measure of the resolving power of the HVS. A small region on the retina that corresponds to a field angle of about 5° around the fixation point is known as the fovea. The visual acuity of the HVS in the fovea region is the greatest, which is around 1 arcmin of resolution, as the cone-like photoreceptors dominate the region. The visual acuity degrades significantly beyond a field angle of $10\text{--}15^\circ$ from the fovea as rod-like photoreceptors become dominant.

The photopic spectrum of the eye spans from 400nm to 700 nm. The curve peaks at 555 nm, which potentially guides us in the optical design of HMDs. A higher weighting factor is often assigned to the green light in the optimization process of the lens design.

The entrance pupil is the optical aperture of the human eye. Under different light levels, the diameter of the pupil changes through dilation and contraction of the muscles that control the iris. The diameter of the pupil changes from 2 mm under sunlight to about 8 mm in the dark. When viewing typical HMD-like displays, the eye pupil diameter is around 3-4mm. However, a larger pupil diameter (preferably 10mm or larger) is required when designing HMD optics to account for the swiveling of the eyes in their sockets without causing vignetting or losing image and to offer a good tolerance of the interpupillary distances (IPD) among different users without the need to mechanically adjust the IPD of the binocular optics.

Most HMDs present users two different images with binocular disparities. By fusing

the two images users are able to view a stereoscopic image. The stereoacuity, which is defined as the depth discrimination threshold expressed in angular terms, varies widely from about 2 arcsec to 130 arcsec among different users. A typical value may be chosen to be 30 arcsec. The interpupillary distance (IPD) is another important parameter that associates with binocular visualization. A variation in IPDs ranging from 55mm to 75mm includes the 95 percentile of values across White, Black, and Asian populations combined (Rolland & Hua, 2005). A mean IPD value of 64 or 65mm is commonly used in engineering investigations and generally IPD adjustment is allowed in HMD systems.

2.2 OVERVIEW OF HEAD MOUNTED DISPLAYS

In the simplest form, an HMD consists of an image source, collimating optics and a housing structure which could be mounted on a user's head. The image source used in an HMD can be either a microdisplay or a modulated laser source. The collimating optics can be a magnifier, a compound eyepiece or a projection lens system. Through the collimating optics, an HMD user is able to view a magnified image. In order to create appropriate views to HMD users based on their head position and possibly gaze point, a tracking system should be employed (Rolland & Hua, 2005).

2.2.1 HMD designs

An HMD will be successful only if full consideration is given to the characteristics and tasks of the user (Melzer & Moffitt, 1997). The design process should consider both engineering factors and human factors including the parameters of human visual system.

In order to design an HMD with high performance and high viewing comfort, the following parameters should be well considered and optimized in the HMD designs:

- Field of view
- Image resolution
- Eye clearance
- Entrance pupil
- Luminance
- IPD

It is desirable that the FOV of an HMD matches that of human eyes especially in an immersive 3D environment. However, due to the limited resolution of a microdisplay, there exists a trade-off between FOV and image angular resolution which is the subtended angle of each pixel. The angular resolution is given by

$$\eta_0 = \frac{\text{FOV}}{N} \quad (2.1)$$

where η_0 is the image angular resolution and N is the total pixel count of the microdisplay along the dimension of interest. A larger FOV would lower the angular resolution if the microdisplay remains the same. In HMD designs, the tradeoff between FOV and image resolution should be balanced to address the need of a specific application.

In a typical HMD design, a microdisplay, which is used as the image source, is placed close to the focal plane of its optical system so that a magnified image can be viewed by the human eye. With a determined FOV, the focal length of the collimation can be obtained through

$$f = \frac{D}{2} \cdot \cot\left(\frac{FOV}{2}\right) \quad (2.2)$$

where f is the effective focal length of the lens and D is the dimension of the active area of the selected microdisplay.

The eye clearance is defined as the closest approach between the entrance pupil of the eye and the HMD which could be either the nearest element of the HMD optics or supporting structure. In the HMD design, it is desirable to have an adequate eye clearance so that the eyebrow or eyeglasses would not touch the HMD optics. The smallest eye clearance value allowable for the wear of low-profile eyeglasses is 17 mm. It is recommended to have an eye clearance of 23mm to accommodate most eyeglasses. The requirement places a constraint on the design of an eyepiece or objective/eyepiece optics since the exit pupil position of eyepiece is outside of the lens. However, for a projection lens, we can adjust the eye clearance by simply adjusting the position of the beamsplitter placed after the projection lens.

The entrance pupil of the HMD should be larger than the effective pupil of the eye to allow for natural eye movements. To allow the user to rotate the eye without causing vignetting effects, the recommended value for the pupil is about 10mm~12mm. This range of pupil size allows an eye swivel of about $\pm 21^\circ$ up to 26.5° within the eye sockets without causing vignetting or loss of image with a typical 3-mm eye pupil in the lighting conditions provided by HMDs.

The luminance level of a displayed image is an important issue for the HMD design and the specific requirement is commanded by the aimed applications. Generally, the luminance of a white paper under a good reading light is about 170cd/m^2 , peak luminance

of a good rear projection home television is about 1700cd/m^2 . Human vernier acuity is close to its best when the luminance level is equal to or greater than 17cd/m^2 . This implies that it is desirable that the luminance of the HMD is at least 17cd/m^2 assuming that the HMD is used in a controlled lighting environment. Moreover, in AR applications, through a beamsplitter computer generated images are combined with the real view of the world. It requires that the luminance of the computer generated image should be at the same level as the luminance of the real world. Currently, most optical see-through HMDs suffer the problem of low luminance due to the low luminance of the microdisplay and the light loss through beamsplitting.

The optical separation between the left and right eye in a binocular HMD should match a user's interpupillary distance (IPD) to avoid visual discomfort. The IPD mismatch would cause an inaccurate depth representation of the rendered image through an HMD. In the extreme mismatch, headaches and nausea may even occur.

2.2.2 Classifications of HMD systems

From the application point of view, HMDs may be categorized as immersive and see-through systems (ST-HMDs). An immersive HMD blocks the real-world view and immerses a user in a computer-generated world, while a ST-HMD superimposes virtual objects upon a real scene to enhance rather than replace the real scene. Immersive HMDs are typically used in Virtual Reality (VR) applications, while ST-HMDs are typically used in the Augmented Reality applications in which the real world view is supplemented by the virtual images. There are two approaches to ST-HMD designs, video see-through

and optical see-through. A video ST-HMD uses one or two miniature video cameras to capture the images of the real world and the captured images are electronically combined with simulated virtual images. The major drawback of a video ST-HMD is that the resolution of the real world is degraded to the pixel resolution of the video camera. An optical ST-HMD allows a user to directly see the real world and optically combines the images of a virtual world with the real-world view through an optical combiner, such as beamsplitter. It creates less intrusion into the real scene than does a video see-through approach (Hua *et al.* 2000). Figure 2.1 (a) and (b) show monocular schematic setups of an immersive HMD and an optical ST-HMD, respectively, both of which use eyepiece type optics.

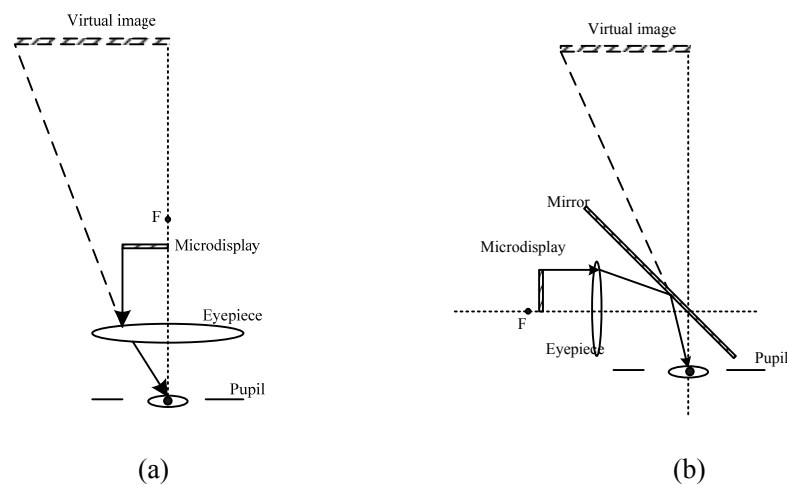


Figure 2.1 Monocular schematic setup of (a) an immersive HMDs and (b) optical STHMD using eyepiece type optics

Based on the type of display optics, HMDs may be classified into non-pupil-forming and pupil-forming systems. In general, HMD optics falls into three types—simple eyepiece magnifier, objective-eyepiece compound magnifier and projection lens. The

simple eyepiece magnifier is considered as a non-pupil-forming system where the eye pupil can be taken as the pupil of the system. In a non-pupil-forming system, there is a large range of eye positions behind the magnifier, known as the eye box, within which the eye can view non-vignetted images. The eye clearance represents the farthest eye position from the optics without introducing additional vignetting effects. The drawback of an eyepiece system is that the ray bundle expands rapidly between the pupil and the lens which makes it hard to design a compact, wide FOV system with acceptable eye clearance especially when a beamsplitter is used for see-through or folding purpose.

Both objective-eyepiece compound system and projection lens are pupil-forming optics. In these systems, the pupil location of the optics should match that of the eye pupil. A pupil mismatch will cause vignetting effects for peripheral fields and even part or the entire virtual image to disappear. The eye clearance represents the nominal eye position from the optics. The eye movement range of a pupil-forming system, which is typically smaller compared with a non-pupil-forming system, is centered at this nominal eye position. Therefore, when designing such systems, the pupil size of the HMD optics should be large enough and the eye clearance should be long enough to account for the effects of eye movements, IPD difference, and pupil position difference among different users. Moreover, the requirements for pupil size should also be “tightly coupled with the overall weight, ergonomics of the system, field of view, and optomechanical design” (Rolland & Hua, 2005).

2.3 HEAD MOUNTED PROJECTION DISPLAYS

Head mounted projection display (HMPD) technology, pioneered by Fisher (Fisher, 1996), Kijima and Ojika (Kijima & Ojika, 1997), and Fergason (Fergason, 1997), has recently been explored extensively as an alternative approach to conventional optical see-through HMD designs (Hua *et al.* 2000, 2001; Rolland & Hua, 2005; Zhang & Hua, 2008). It is considered as a technology lying on the boundary between conventional HMDs and CAVE-like projection displays (Cruz-Neira, *et al.* 1993). Two major aspects distinguish the HMPD technology from conventional HMDs and projection systems: projection optics is used to replace eyepiece-type lens in a typical HMD design and a retroreflective screen is used to substitute a typical diffusing screen in a conventional projection system (Hua, *et al.* 2003).

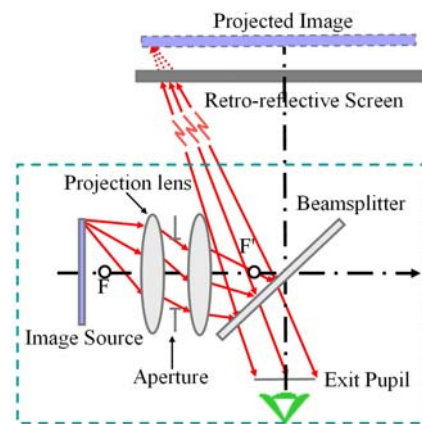


Figure 2.2 Monocular schematic design of an HMPD (Hua, *et al.* 2003)

A monocular configuration of an HMPD is conceptually illustrated in Figure 2.2. Unlike a conventional optical see-through HMD, an HMPD replaces eyepiece-type optics with a projective lens. An image on a miniature display, which is located beyond the focal point of the lens, rather than between the lens and the focal point as in a

conventional HMD, is projected through the lens and thus forms a magnified real image. A beamsplitter, oriented at 45° , reflects the light from the projection lens toward a retroreflective screen. The retroreflective screen, which is typically positioned remotely away from the user, will then redirect the light along its incident direction back the beamsplitter. Thus, the exit pupil of the system, through which the eye views the projected image, forms at the conjugate position of the pupil of the projection lens through the beamsplitter.

Compared with conventional eyepiece based HMDs, an HMPD has three advantages. First, due to its relatively more symmetric lens structure than an eyepiece, the size, weight and distortion of a projection lens do not scale as rapidly as an eyepiece, while it is very challenging to design a wide FOV, compact and low distortion eyepiece optics. Second, in an HMPD system a large eye relief can be achieved by simply adjusting the distance between the projection lens and the beamsplitter without compromising the performance of the projection system, while it is more challenging to design an eyepiece with a large eye relief. Increasing the eye relief of an eyepiece typically results in larger optics, higher distortion, and perhaps compromised FOV. Third, the HMPD technology provides intrinsically correct occlusion of computer generated virtual objects by real objects as demonstrated in Figure 2.3, while in a conventional HMD the virtual image floats on the real object. Moreover, the retroreflective screen can be applied anywhere in physical space and can be tailored to arbitrary shapes without introducing additional distortion over the virtual images.



Figure 2.3 Natural occlusion of the computer-generated object (bone) by the real object (hand) through an HMPD. (Hua, *et al.* 2000)

The HMPD concept has been recently explored extensively by several researchers (Inami *et al.* 1999; Kawakami *et al.* 2000; Hua *et al.* 2000, 2001, 2002, 2003). Large field of view (FOV), lightweight and low distortion optics for HMPD systems have been designed (Hua *et al.* 2001, 2003), and a custom-designed lightweight and compact prototype was developed (Hua *et al.* 2001). There have been several attempts thereafter to explore more compact and brighter HMPD designs. For instance, optical diagnostic and applications laboratory (ODA Lab) has designed a 70-deg wide FOV projection lens (Ha, *et al.* 2002), and has developed an OLED-based (organic light emitting display) 42-deg prototype, collaborating with NVIS Inc. (Rolland and Hua 2005). Hua recently developed a 2nd-generation prototype that is lighter and more compact by employing an optical folding mechanism. A photograph of the 1st generation HMPD prototype is shown in Figure 2.4(a). It weighs about 750 grams. The 2nd generation prototype, using the same projection optics as the first one, is shown in Fig. 2.4(b). Both prototypes achieved 52-degree FOV with 640x480 VGA resolution.



Figure 2.4 (a) First-generation HMPD prototype and (b) Second-generation HMPD prototype (Hua *et al.* 2001, 2003)

However, there exists a low-efficiency problem in an HMPD system in which the projected light is split twice through a beamsplitter as illustrated in Figure 2.2. Using a 50/50 beamsplitter leads to the loss of at least 75% of the light from a displayed image. Moreover, considering the low retroreflectance of typical retroreflective materials, the overall luminous efficiency of an HMPD is around 4%. For instance, with a miniature backlit active matrix liquid crystal display (AMLCD) as the image source, the luminance of the observed image of an HMPD is estimated to be 4cd/m^2 , while the average luminance of a well-lit indoor environment is over 100cd/m^2 . As a result, the image of an HMPD will appear washed out in such well-lit environments. In fact, most OST-HMDs, including the HMPD, typically have to be operated under a dimmed lighting condition (Zhang & Hua, 2007).

2.4 POLARIZED HEAD MOUNTED PROJECTION DISPLAYS

To address the problem of low luminance, a polarized head mounted projection display (p-HMPD) was proposed (Hua & Gao, 2005, 2007). By carefully manipulating the polarization states of the light propagating through the system, a p-HMPD can

potentially be three times brighter than a traditional non-polarized HMPD design using the same microdisplay technologies. A schematic design of a monocular p-HMPD configuration is illustrated in Figure 2.5. The image on a microdisplay is projected through the projection lens, forming an intermediate image. The light from the microdisplay is manipulated to be S-polarized so that its polarization direction matches the high reflection axis of the polarized beamsplitter (PBS). After the projected light is reflected by the PBS, it is retroreflected back to the same PBS by a retroreflective screen. The depolarization effect by the retroreflective screen is less than 15% within ± 20 degrees and is less than 23% up to ± 30 degrees (Zhang & Hua, 2008). As a result, the retroreflected light remains dominantly the same polarization as its incidence light. In order to achieve high transmission through the PBS after the light is retroreflected, a quarter-wave retarder is placed between the PBS and the retroreflective screen. By passing through the quarter wave retarder twice, the incident S-polarized light is converted to P-polarization and transmits through the PBS with high efficiency. Thus, the projected image from the microdisplay can be then observed through the exit pupil of the system where the eye is placed. The work in this dissertation is based on the schematic design of the p-HMPD.

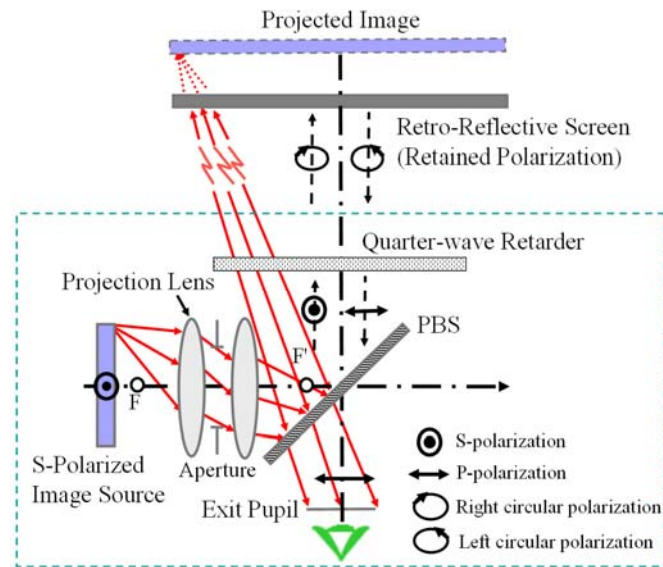


Figure 2.5 Schematic design of a polarized HMPD (Hua and Gao, 2005; 2007)

2.5 APPLICATIONS OF HMPD TECHNOLOGIES

A wide range of applications using HMPDs for 3D visualization has been explored and demonstrated (Parsons and Rolland 1998; Kawakami *et al* 1999; Inami *et al* 2000; Hua *et al* 2001, 2002; Kijima *et al* 2002). For example, Kawakami and Inami developed a system called X'tal Vision and proposed the concepts of object-oriented displays and visual-haptic displays (Kawakami *et al* 1999; Inami *et al* 2000). Parsons and Rolland proposed the HPMD technology as a tool for medical visualization (1998). Besides single-user 3D visualization applications, the HMPD concept intrinsically “enables a shared workspace with an arbitrary number of individual viewpoints, rather than the leader privileged viewing mode of a traditional CAVE-like projection environment” (Hua, 2005). Multiple HMPD-based collaborative spaces have been developed in different forms. For instance, a deployable room coated with retroreflective screens has been

developed (Davis *et al* 2003; Rolland *et al* 2002). Hua *et al.* have developed a multi-scale collaborative infrastructure, referred to as SCAPE, which supports versatile modes of user interaction and collaborative operation in AR applications (Hua, *et al.*, 2003). In the following part, the SCAPE system developed in the 3DVIS Lab is introduced.

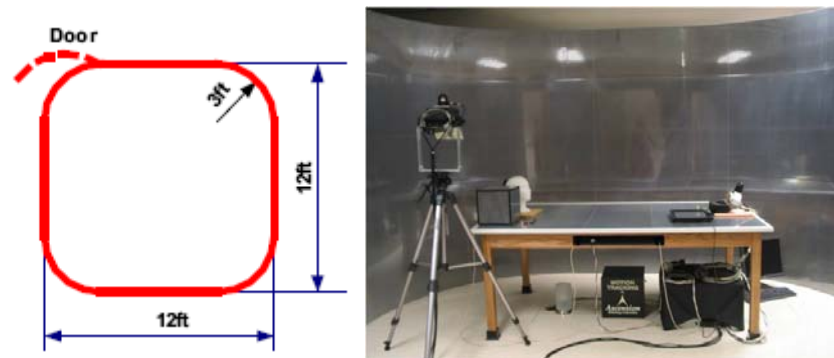


Figure 2.6 (a) Dimensions for the SCAPE (b) Setups for the SCAPE (Hua, *et al.*, 2003; 2004)

The SCAPE combines “a retroreflective workbench allowing exocentric viewing of an augmented dataset with a room display allowing egocentric viewing of life-size virtual environments” (Hua *et al.*, 2003, 2004). As shown in Figure 2.6(a), the side length of the room display is about 12 feet, and the retroreflective screen is attached on the wall of the room to form a virtual environment. The size of the workbench which coated with a retroreflective screen is about 5 feet by 3 feet. A 3D scene graph of the Aztec city was developed based on the SCAPE (Hua *et al.*, 2003). In this application, a computer-generated micro-scene with low details is registered with the workbench and the physical objects on the workbench, while through the surrounding room display an immersive walk-through macro-scene with high details can be viewed. Thus, SCAPE allows “a seamless blending of dual-scale, dual-perspective, virtual and augmented

components, within which multiple users can concurrently interact from their individual viewpoints” (Hua *et al* 2004). Figures 2.7 (a) and (b) show the sample views captured from the display for the workbench and the wall applications, respectively. Moreover, a physical device named magic lens, which is coated with a retroreflective screen, is used to overlay high-resolution “pop-up” views on top of a low-resolution virtual map. Other application examples of SCAPE include the “GO game” and the medical visualization shown in Figure 1.1(Hua *et al.* 2004).

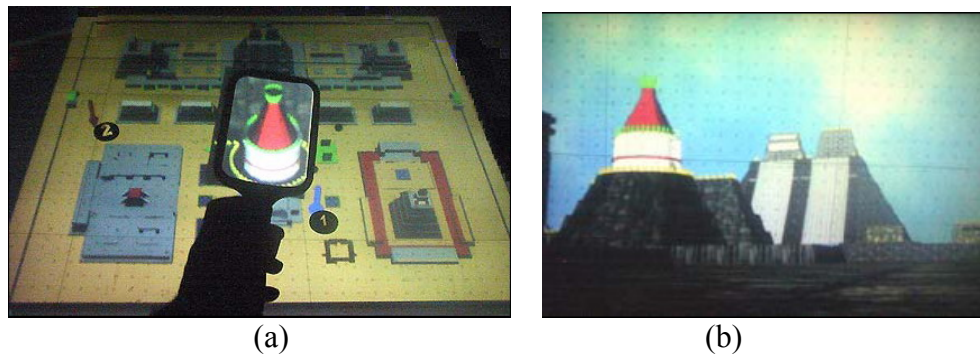


Figure 2.7 (a) Sample view for the workbench applications; (b) Sample view through the surrounding wall display (Hua, *et al.* 2004)

2.6 SUMMARY

In this chapter, the background information related to the work of this dissertation was reviewed, including the human factors and the engineering aspects of an HMD system, the schematic designs of an HMPD and a p-HMPD, and application examples of the HMPD technology.

CHAPTER 3

POLARIZATION CHARACTERIZATION IN A P-HMPD

Chapter 3 is partially based on a published article entitled “Characterizing polarization management in a p-HMPD system” (Zhang & Hua, 2008).

Fundamental to the design of a high-performance p-HMPD system is the quality of polarization management in a wide FOV and broadband system. In this chapter, polarization components are compared and selected for designing a p-HMPD system. Furthermore, the polarization performance of each element in both HMPD and p-HMPD is characterized using the Mueller matrix, based on which the overall imaging performance of the two systems are analyzed.

3.1 POLARIZATION REPRESENTATION

3.1.1 Stokes vector

The Stokes vector is a standard method to characterize the polarization properties of the light, particularly for incoherent light. It can be used to characterize polarized light, unpolarized light and partially polarized light.

The Stokes vector, S , is a vector with four real-valued elements, which are defined by six polarized flux measurements

$$S = \begin{pmatrix} S_0 \\ S_1 \\ S_2 \\ S_3 \end{pmatrix} = \begin{pmatrix} P_H + P_V \\ P_H - P_V \\ P_{45} - P_{135} \\ P_R - P_L \end{pmatrix} \quad (3.1)$$

The element S_0 is the addition of horizontal polarized flux P_H and vertical polarized flux P_V and represents the total irradiance of the beam. The element S_1 is the horizontal polarized flux component minus the vertical flux component. The element S_2 equals to the 45° linear polarized flux component P_{45} subtracted by the 135° linear polarized flux component P_{135} while the element S_3 equals to the right circular polarized flux component P_R minus the left circular polarized flux component P_L . A normalized Stokes vector can be used to study the polarization properties by discarding the flux magnitude information of the light. A normalized vector can be obtained by scaling the vector to total irradiance S_0 to 1.

Based on the Stokes vector, polarization properties of the light can be further characterized. The degree of polarization (DoP), a parameter that characterizes the randomness of polarization states, is defined as

$$DoP = \frac{\sqrt{S_1^2 + S_2^2 + S_3^2}}{S_0}. \quad (3.2)$$

The degree of linear polarization ($DoLP$), which describes the extent to which the polarization light tends to be linear, is defined as

$$DoLP = \frac{\sqrt{S_1^2 + S_2^2}}{S_0}. \quad (3.3)$$

3.1.2 Mueller matrix

Mueller matrix is the principal method for characterizing the various polarization properties of a sample, such as retardance, diattenuation and depolarization. It is a four-by-four matrix with real-valued elements. It is used for polarization characterization when the incident light has a linear interaction with the sample. The Stokes vector of the incident light $S_{Incident}$ can be related with the exiting Stokes vector $S_{Exiting}$ by

$$S_{Exiting} = \begin{bmatrix} S_0 \\ S_1 \\ S_2 \\ S_3 \end{bmatrix} = M \cdot S_{Incident} = \begin{bmatrix} m_{00} & m_{01} & m_{02} & m_{03} \\ m_{10} & m_{11} & m_{12} & m_{13} \\ m_{20} & m_{21} & m_{22} & m_{23} \\ m_{30} & m_{31} & m_{32} & m_{33} \end{bmatrix} \cdot \begin{bmatrix} S_0 \\ S_1 \\ S_2 \\ S_3 \end{bmatrix}. \quad (3.4)$$

For a beam passing through a sequence of polarization elements $q=1, 2, \dots, n$, the final Mueller matrix M can be calculated by multiplying the matrices from right to left as

$$M = M_n M_{n-1} \cdots M_2 M_1. \quad (3.5)$$

Each Mueller matrix contains 16 degrees of freedom (DOFs), among which seven DOFs are associated with non-depolarizing processes, such as diattenuation, retardance, and polarization-independent loss such as absorption, and the other nine DOFs are associated with depolarization and describe how different states of polarization are depolarized (Chipman 2005).

3.1.3 Mueller matrix decomposition

A Mueller matrix can be decomposed into a sequence of three matrices representing a diattenuator, a retarder and a depolarizer respectively, as described in

$$M = M_{\Delta} M_R M_D \quad (3.6)$$

Where M_{Δ} represents a depolarizer, M_R represents a retarder and M_D represents a diattenuator.

The intensity transmission of a diattenuator depends on the incident polarization state. A diattenuation vector \vec{D} is defined as

$$\vec{D} = \begin{pmatrix} D_H \\ D_{45} \\ D_C \end{pmatrix} \quad (3.7)$$

where D_H is horizontal diattenuation, D_{45} is 45° linear diattenuation and D_C is circular diattenuation. The diattenuation magnitude of a diattenuator is defined as

$$D = \frac{T_{\max} - T_{\min}}{T_{\max} + T_{\min}} \quad (3.8)$$

in which T_{\max} is the maximum transmission and T_{\min} is the minimum transmission.

The first row of a Mueller matrix completely determines the intensity transmittance of an incident beam and the diattenuation vector \vec{D} is given by

$$\vec{D} = \begin{pmatrix} D_H \\ D_{45} \\ D_C \end{pmatrix} = \frac{1}{m_{00}} \begin{pmatrix} m_{01} \\ m_{02} \\ m_{03} \end{pmatrix} \quad (3.9)$$

and the diattenuation magnitude is given by

$$D = \frac{1}{m_{00}} \sqrt{m_{01}^2 + m_{02}^2 + m_{03}^2} \quad (3.10)$$

Similarly the retardance vector and the retardance are given by

$$\vec{R} = \begin{pmatrix} R_H \\ R_{45} \\ R_C \end{pmatrix} \quad \text{and} \quad R = \sqrt{R_H^2 + R_{45}^2 + R_C^2} \quad (3.11)$$

where R_H , R_{45} and R_C represent horizontal, 45°-linear, and circular retardance components, respectively. Through the decomposition of a Mueller Matrix, the corresponding retardance values can be obtained (Lu & Chipman, 1996)

The depolarization refers to the conversion of polarized light into unpolarized light or partially polarized light. A pure depolarizer, an element with zero diattenuation or retardance is given by

$$\begin{bmatrix} 1 & 0 & 0 & 0 \\ 0 & a & 0 & 0 \\ 0 & 0 & b & 0 \\ 0 & 0 & 0 & c \end{bmatrix} \quad |a|, |b|, |c| < 1. \quad (3.12)$$

The depolarization index (Dep) is defined as a figure of merit for the depolarization magnitude and can be obtained through:

$$Dep = 1 - \frac{[\sum_{i,j} m_{ij}^2 - m_{00}^2]^{1/2}}{\sqrt{3}m_{00}}. \quad (3.13)$$

Dep measures how close a Mueller Matrix is to a non-depolarizing Mueller matrix. Dep equals 1 for an ideal depolarizer and equals zero for non-depolarizing Mueller matrices.

3.2 POLARIZATION ELEMENTS IN THE P-HMPD SYSTEM

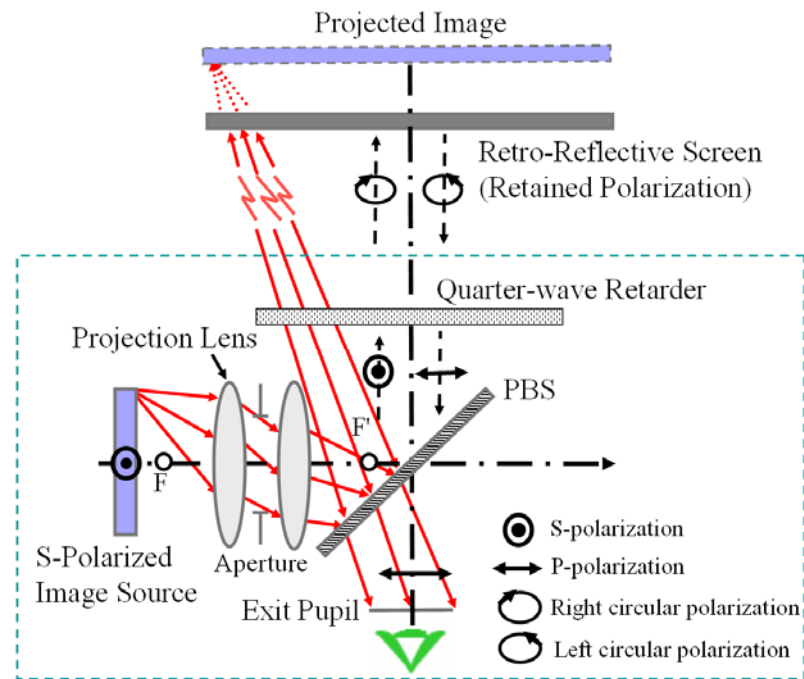


Figure 3.1 Schematic design of a p-HMPD system (Hua & Gao, 2005;2007)

As shown in the schematic design of a p-HMPD in Figure 3.1, the polarization state of the light emitted from the projection lens is manipulated by a polarized beamsplitter (PBS) and a quarter-wave retarder (QWR). To build a high performance p-HMPD system, it is important to implement high quality polarization elements. However, most polarization elements demonstrate considerable variations across a range of incident angles and wavelengths. The angular and chromatic dependence can significantly reduce the overall luminance transfer efficiency and degrade the uniformity of a projected image across the FOV, creating vignetting-like visual artifacts. It can also cause different color shifts in the final image across the FOV, yielding inconsistent color representations. In the following section, different types of QWR and PBS are compared and the components with the best performance are selected for our system.

3.2.1 Selection of retarder

Different quarter-wave plates perform differently as a function of wavelength and incident angle. Our goal is to select a QWR with small variation of retardance across the FOV and the visible spectrum. Meanwhile, the vendor should also be able to fabricate the retarder with the desired size.

Birefringent materials such as mica and quartz are widely used for the retarder. However, the performance of those crystal retarders highly depends on the incident angle and wavelength. For example, the retardance of a quarter-wave Mica retarder can be as high as a half wave for the light with a wavelength of 450nm and an incident angle of 30°. If a mica retarder is used in a p-HMPD system, it yields almost zero efficiency for the light with the wavelength of 450nm and a large incident angle, while it produces much higher efficiency for light with a wavelength of 550nm and a normal incident angle. The projected image would appear not only severely vignetted from the center FOV to the edge, but also in incorrect colors.

By combining two crystals, such as quartz and magnesium fluoride, an achromatic retarder can be made. The bi-crystalline retarder, however, has a small FOV ($<10^\circ$) and is hard to fabricate in a large size.

A polymer quarter-wave retarder custom-made by Bolder Vision Optik is selected for a p-HMPD system. It not only has accurate retardance across a large FOV ($\sim 30^\circ$) and the visible spectrum, but is also easy to fabricate at the desired size. To reduce the wavefront distortion and reflection, a polymer retarder is laminated by a pair of flat BK7 glasses,

which are coated by anti-reflection coating. Although a polymer retarder has a lower power threshold value and is more sensitive to the temperature compared with a crystal retarder, it is not an issue for a p-HMPD since both incident power and temperature are far below the threshold values.

3.2.2 Selection of PBS

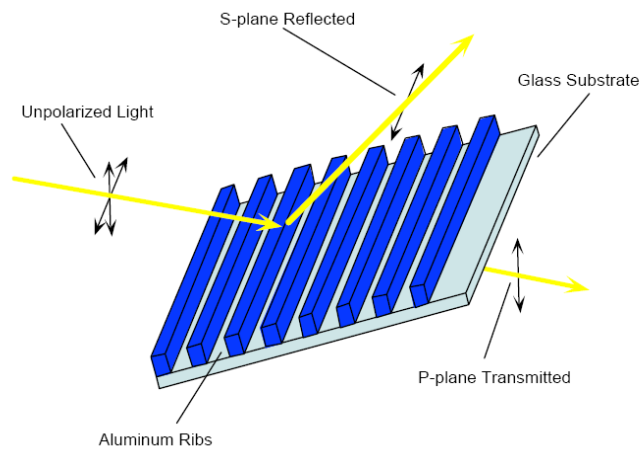


Figure 3.2 Structure of a wire-grid PBS (Courtesy of Moxtek)

A PBS reflects S-polarized light with high reflectivity and allows P-polarized light to transmit with high efficiency. Conventional MacNeille beamsplitters have poor contrast and poor transmission uniformity across FOV, and these weaknesses become increasingly intolerable as the FOV is increased. Moreover, the cube structure of a MacNeille beamsplitter makes it too bulky to be integrated into HMDs. A wire-grid PBS is selected for the p-HMPD application. It has a thin form factor with only 1.6mm thickness and can be custom-made easily. The simplified structure of a wire-grid PBS is shown in Figure 3.2. Aluminum is deposited on a glass substrate and lithographically etched to form a

periodical wire-grid (aluminum rib) structure. The light with polarization parallel to the wire axis, which is s-polarized light, is highly reflected while light with polarization normal to wire axis, which is P-polarized light, is almost totally transmitted. Since the polarization axis is determined by the direction of wire-grid structure, the performance of PBS is much less dependent on the incident angle and wavelength of the incident light. The disadvantage of wire-grid PBS is that the aluminum coating can be easily damaged by finger touch and aberrations can be introduced when the light transmits through the PBS plate with 45 degree tilt angle.

In the following section, the performance of each component in a p-HMPD and HMPD is characterized using Mueller matrix. The overall performance of a p-HMPD and HMPD is analyzed and compared.

3.3 MEASUREMENT METHOD

3.3.1 Axometrics polarimeter

An Axometrics polarimeter was used for Mueller matrix measurements of a sample. As shown in Figure 3.3, it consists of a polarization state generator (PSG) that illuminates a testing sample with the light in a series of calibrated polarization states and a polarization state analyzer (PSA) that collects the light transmitted through or reflected from the sample and analyzes the polarization states. Both the PSG and PSA are constructed from a rotating linear retarder and a stationary linear polarizer. While the polarimeter can be calibrated across a broad range of wavelengths, for each sample we took measurements for three wavelengths, 450nm, 550nm, and 650nm, respectively, to

cover the spectral range of the displays. The beam from the polarization state generator is near collimated and the beam size can be adjusted. Since the cone angle of the ray bundle from the projection lens is small, less than 1° , the overall performance of a p-HMPD at a given FOV can be characterized by a semi-collimating beam at the corresponding field angle from the polarimeter.

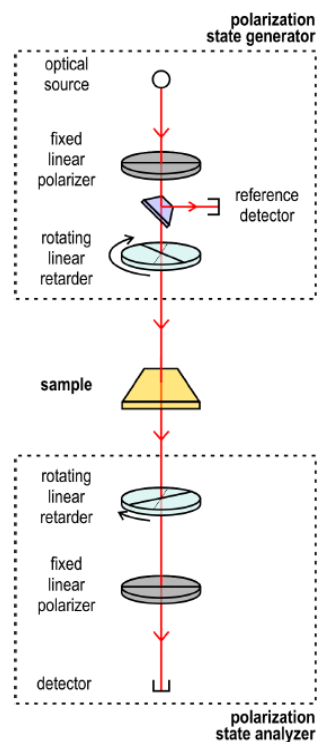


Figure 3.3 Schematic structure of Axometrics polarimeter (Courtesy of Axometrics)

3.3.2 Experimental setup

Considering that the FOV of existing HMPDs is typically limited within 60° due to ergonomic factors and the considerably lower retroreflectance at larger angles (Hua *et al.* 2002), the Mueller matrices of each component from the field angle of -28° to 28° at a 2° increment relative to the on-axis direction were measured.

Ideally, the measurement should be performed across the ϕ - θ space within the FOV

of $\pm 30^\circ$. However, due to limited degrees of freedom of the Axometrics polarimeter, the measurement was only performed in one primary plane of the p-HMPD as shown in Figure 3.1. A more complex measurement that gives results in φ - θ space can be done through a Mueller matrix imaging polarimeter (Pezzaniti & Chipman, 1990) using the similar testing and data processing method as described.

In the measurement, we aim to obtain the Mueller Matrices of the following components through the optical path of a p-HMPD and HMPD:

- Transmission Mueller matrices of the retarder
- Transmission and reflection Mueller matrices of the PBS
- Transmission and reflection Mueller matrices of the beamsplitter
- Retroreflection Mueller matrices of the retroreflective screen

The transmission Mueller matrices of a retarder were directly measured with the setup illustrated in Figure 3.4(a), in which the PSG and PSA are coaxially aligned and the sample is rotated at a 2° increment from its on-axis orientation. The rotation angle θ in each setup in Figure 3.4 refers to the field angle of the system, and the positive rotation angle is consistent with positive direction of the system field angle. For the setup in Figure 3.4(a), counterclockwise rotation of the sample corresponds to the positive field angles and clockwise for negative angles. For instance, the retarder was initially positioned perpendicularly to the optical axis and the measurements were taken for incident angles within $\pm 28^\circ$. Similarly the transmission Mueller matrices of beamsplitters or PBS were measured with the setup in Figure 3.4 (b). The beamsplitters were initially positioned at a 45° angle with the optical axis and the measurements were taken for

incident angles from 17° to 73° . In this case, clockwise rotation of the sample is for the positive field angles and counterclockwise for negative angles.

The reflective Mueller matrices of the beamsplitter and PBS were measured with the setup in Figure 3.4(c), in which the PSG is aligned with the optical axis and both the PSA and the samples are rotated from their on-axis orientations to a certain direction for a given field angle. The samples were initially positioned at -45° with the optical axis, and the PSA was aligned in a 90° angle with the optical axis. As the samples were rotated, the PSA were adjusted accordingly to analyze the reflected light. Clockwise rotation was for the positive field angles and counterclockwise was for the negative field angles.

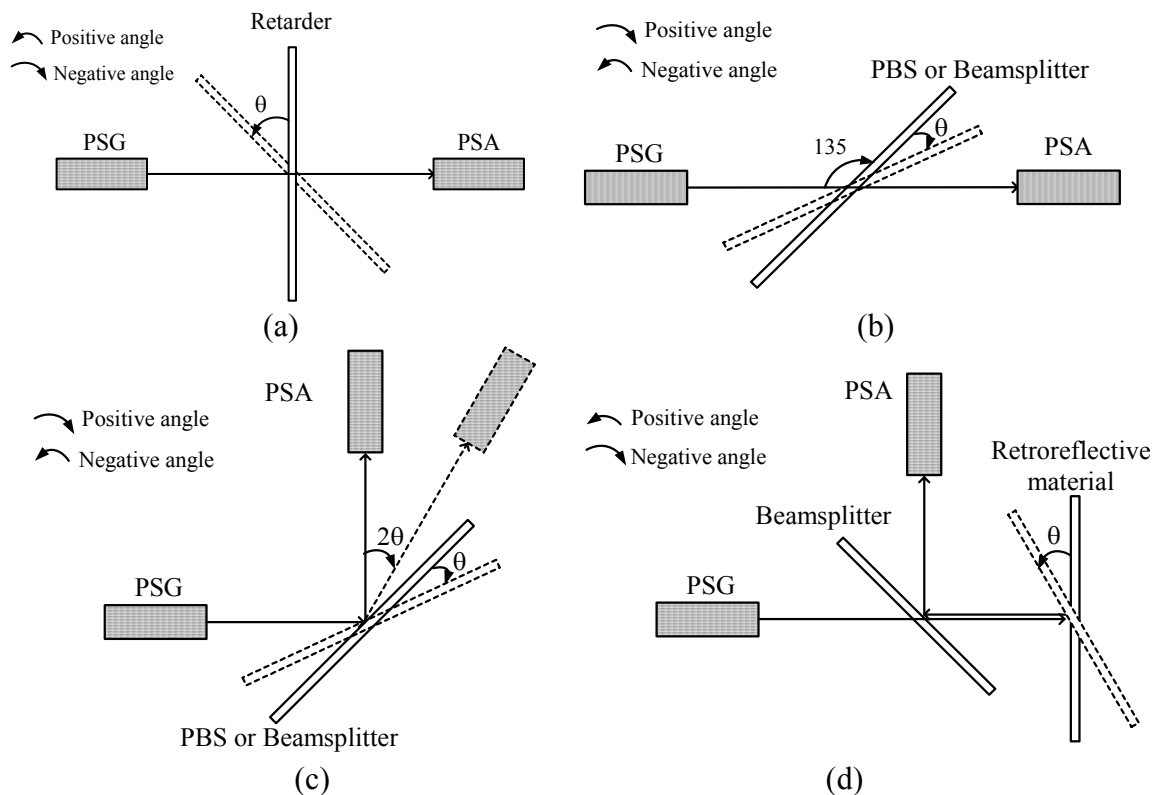


Fig. 3.4 Polarimeter setup for polarization measurements of (a) Transmittance of a retarder; (b) Transmittance of a PBS or a beamsplitter; (c) Reflectance of a PBS or a beamsplitter; and (d) Retroreflectance of a retroreflective screen.

The Mueller matrices of a retroreflective screen were measured with the setup illustrated in Figure 3.4(d), in which the PSG and PSA are aligned in a 90° angle and a non-polarizing beamsplitter was used in the measurement. The reflection and transmission properties of the beamsplitter were characterized following the same procedure described above. The PSG, PSA and beamsplitter remained fixed, while the retroreflective screen was rotated from -28° to 28° relative to the on-axis orientation. Counterclockwise rotation corresponded to the positive field angles and clockwise for negative angles. The Mueller matrix of a retroreflective screen at a given field angle θ and wavelength λ is then given as

$$M_{retro}(\theta, \lambda) = [M_{BS-R}(0^\circ, \lambda)]^{-1} * M_{meas}(\theta, \lambda) * [M_{BS-T}(0^\circ, \lambda)]^{-1} \quad (3.14)$$

where M_{retro} is the retroreflection Mueller matrix of a retroreflective screen, $M_{BS-R}(0^\circ, \lambda)$ and $M_{BS-T}(0^\circ, \lambda)$ are the reflection and transmission Mueller matrices of the beamsplitter at 45° incident angle and at the wavelength of λ , respectively, and $M_{meas}(\theta, \lambda)$ is the Mueller matrix directly measured by the polarimeter in Figure 3.4(d).

3.4 EXPERIMENTAL RESULTS

3.4.1 PBS and non-polarizing beamsplitters

A wire-grid (WG) PBS custom-designed by Moxtek was selected for the p-HMPD system. Based on the transmission Mueller matrices measured at each incidence angle and wavelength, the corresponding transmittance of the PBS for S- and P-polarized incident light are calculated by

$$T_{S-PBS}(\theta, \lambda) = \frac{1}{2}(m_{00} - m_{01} - m_{10} + m_{11}) \quad (3.15)$$

and

$$T_{P-PBS}(\theta, \lambda) = \frac{1}{2}(m_{00} + m_{01} + m_{10} + m_{11}) \quad (3.16)$$

where T_{S-PBS} and T_{P-PBS} are the transmittance of the PBS for the S- and P-polarized light, respectively. Similarly, the reflectance of the PBS for the S- and P-polarized light are calculated by their corresponding reflective Mueller matrices as

$$R_{S-PBS}(\theta, \lambda) = \frac{1}{2}(m_{00} - m_{01} - m_{10} + m_{11}) \quad (3.17)$$

and

$$R_{P-PBS}(\theta, \lambda) = \frac{1}{2}(m_{00} + m_{01} + m_{10} + m_{11}) \quad (3.18)$$

where R_{S-PBS} and R_{P-PBS} are the reflectance of the PBS for the S- and P-polarized light, respectively.

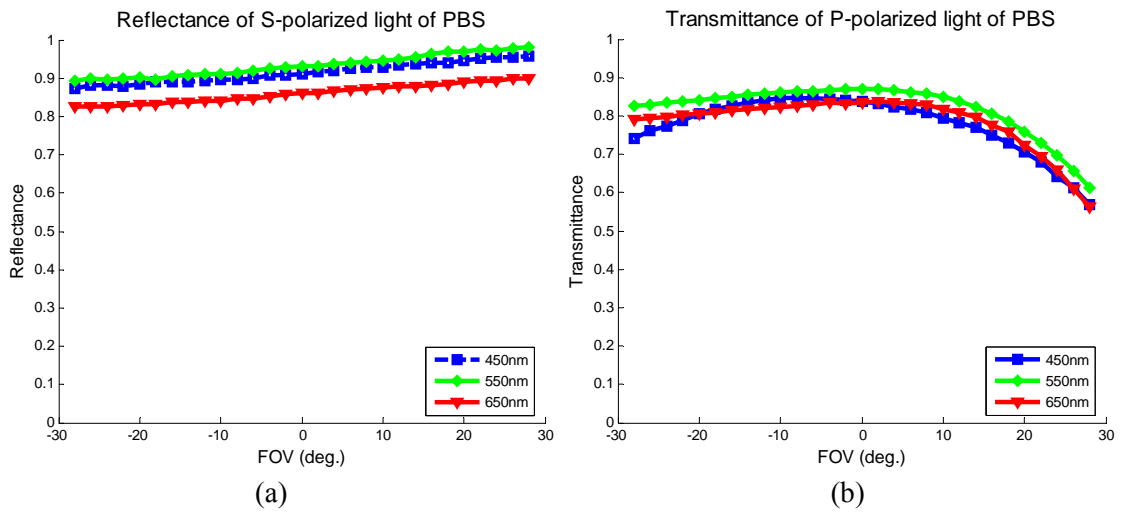
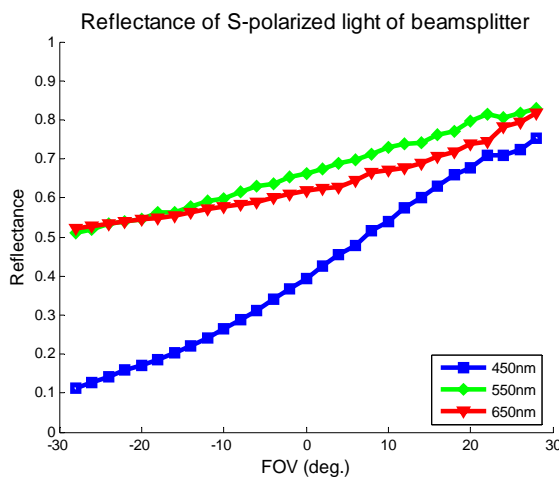
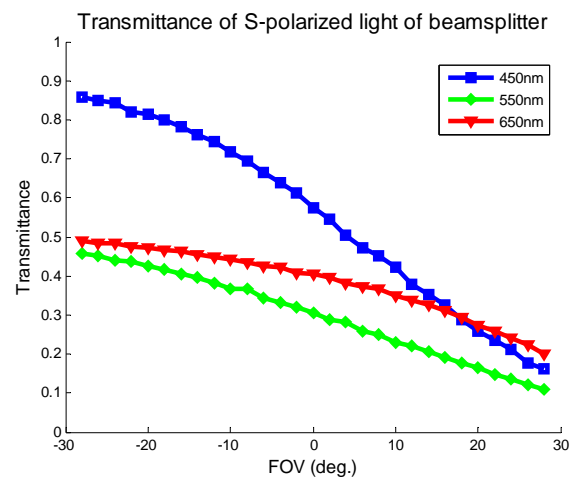


Figure 3.5 Characterizing the PBS: (a) Reflectance of S-polarized light; (b) Transmittance of P-polarized light

The reflection and transmission performance of a WG-PBS is highly dependent on the wire direction relative to the polarization axis and also depends on whether the wire-grid film is facing the incident light. The WG-PBS demonstrates the best performance when the wire direction is parallel to the S-polarization direction of the incident light and the wire coating is facing toward the incident light. In designing a p-HMPD system, the polarization axis of the light from the microdisplays was manipulated to match the high reflection axis of the PBS. Figures 3.5(a) and 3.5(b) plot the reflectance of the S-polarized light and the transmittance of the P-polarized light, respectively, as a function of FOV for the three testing wavelengths. The 0° field angle corresponds to a 45° incidence angle on the PBS. The negative field angle indicates that a ray is incident on the PBS at an angle less than 45° . The reflectance for S-polarized light is approximately 90% on average for the 0° field angle, varying between 82% and 96% for field angles in the range of $\pm 28^\circ$. The transmittance of P-polarized light is approximately 87% for 0° field angle, varying between 87% and 60% for field angles in the range of $\pm 28^\circ$.



(a)



(b)

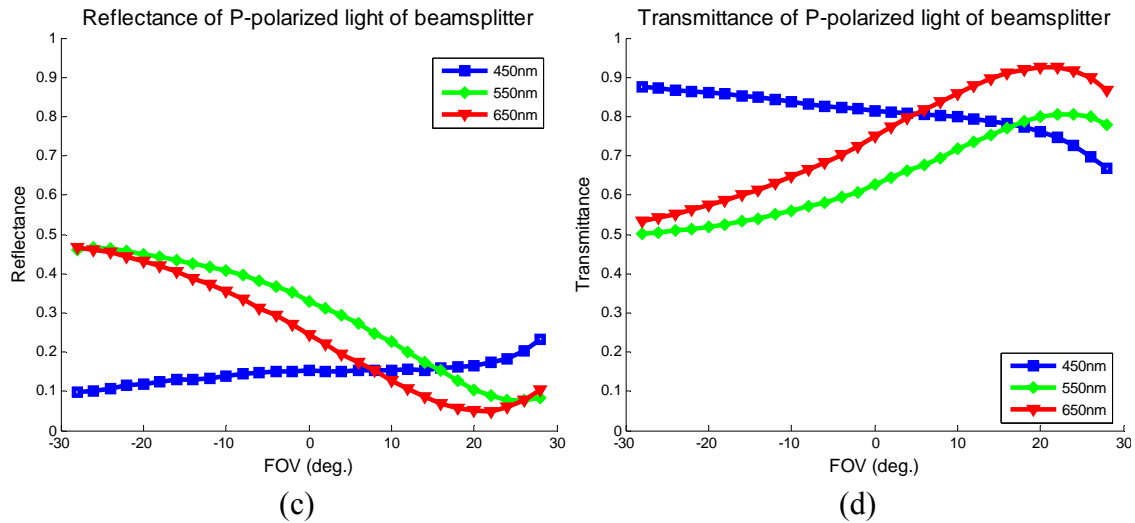


Figure 3.6 Characterizing a beamsplitter: (a) Reflectance and (b) Transmittance of S-polarized light; and (c) Reflectance and (d) Transmittance of P-polarized light.

In similar manners, we characterized polarization properties of a 50/50 non-polarizing beamsplitter, which was used not only for the measurement of a retroreflective screen but also for comparing the display performance between a p-HMPD and a conventional non-polarizing HMPD. Based on the measurements of transmission and reflection Mueller matrices, the transmittance and reflectance of the non-polarizing beamsplitter for S- or P-polarized incident light can be calculated through Equation 3.15 to Equation 3.18 for each field angle and wavelength. The transmittance and the reflectance for non-polarizing incident light are equal to the m_{00} elements of the corresponding Mueller matrices. Figure 3.6(a) and 3.6(b) plot the reflectance and transmittance of S-polarized light, respectively, while Figure 3.6(c) and 3.6(d) plot the reflectance and transmittance of P-polarized light respectively. The reflectance for S-polarized light is approximately 55% on average for the 0° field angle, varying between 10% and 85% for field angles in the range of $\pm 28^\circ$. The transmittance for S-polarized

light is approximately 45% on average for the 0° field angle, varying between 10% and 87% for field angles in the range of $\pm 28^\circ$. The reflectance for P-polarized light is approximately 25% on average for the 0° field angle, varying between 5% and 46% for field angles in the range of $\pm 28^\circ$. The transmittance for P-polarized light is approximately 45% for 0° field angle, varying between 50% and 95% for field angles in the range of $\pm 28^\circ$. From the graph, non-polarizing beamsplitter also shows the polarization preference. Compared with the PBS, the reflectance and transmittance of the non-polarizing beamsplitter demonstrate considerably large variations among the three wavelengths and much higher dependence on field angles.

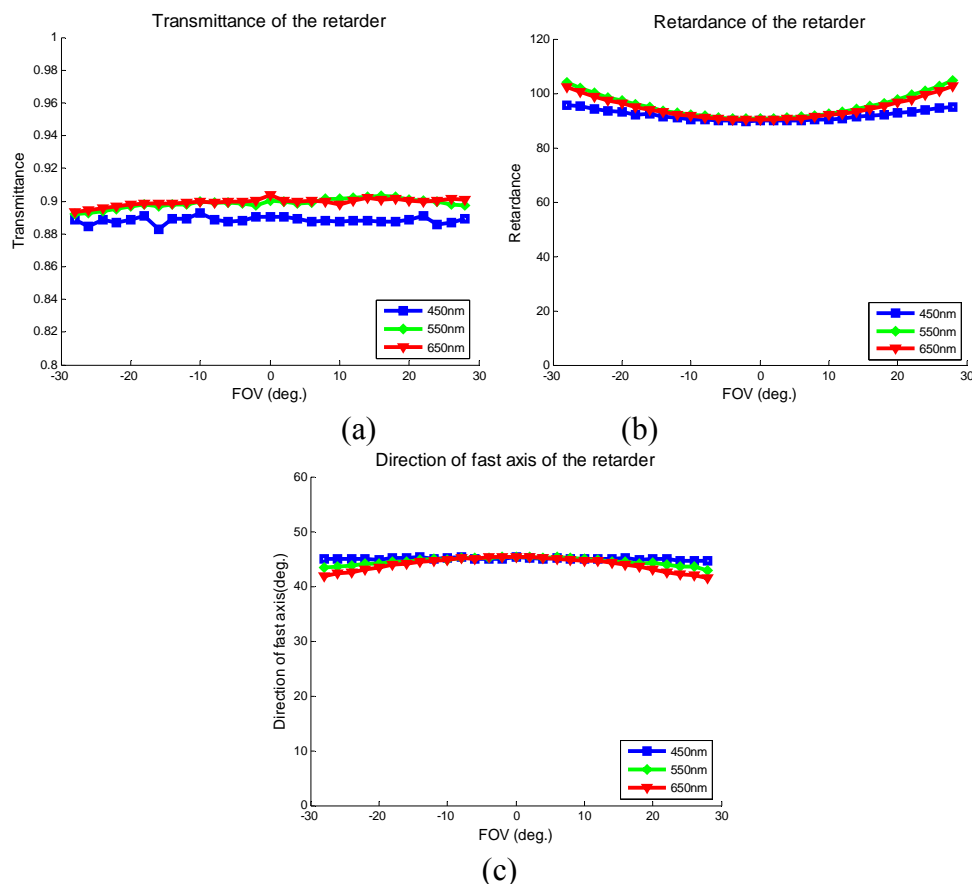


Figure 3.7 Characterizing a retarder: (a) Transmittance; (b) Retardance; and (c) Fast-axis direction

3.4.2 Retarder

The polymer quarter-wave retarder custom-made by Bolder Vision Optik was selected for a p-HMPD system due to its large FOV and broadband response to the visible wavelengths. Figures 3.7(a) through 3.7(c) plot the transmittance, the retardance magnitude, and the fast-axis direction of the retarder as a function of field angles at the three wavelengths. The transmittance of the retarder is approximately constant across the entire FOV with less than 1.5% of variation. The retardance magnitude remains approximately constant up to $\pm 16^\circ$ and increases gradually by 20nm (approximately 3.7% of the testing wavelength) at $\pm 28^\circ$. The direction of the fast axis also remains fairly constant at a 45° angle with the optical axis for the field angles less than $\pm 16^\circ$ and the angle decreases to about 42° at the field angle of $\pm 28^\circ$. The transmittance and retardance properties of the retarder demonstrate low dependence on the wavelengths. The variations of the retardance magnitude and fast axis direction with the incident angle could result in a slightly lower overall efficiency at a marginal visual field of the display than the center, creating vignetting-like artifacts.

3.4.3 Retroreflective screen

The retroreflective screen used in our p-HMPD system is made of hollow reflective micro corner cubes, the imaging properties of which will be discussed in Chapter 6. The retroreflection Mueller matrices of a retroreflective screen as a function of incidence angle and wavelength are obtained from the Equation 3.14. Figure 3.8 plots the normalized Mueller matrices at the wavelength of 550nm as a function of incident angles.

All the elements in each of the Mueller matrices are normalized by their first element m_{00} except the m_{00} itself (DeBoo *et al.* 2005). In this 4x4 graph array, each graph contains the plot of the normalized element value as a function of incident angles only for the wavelength of 550nm as the measurements demonstrate little dependence on wavelength. The m_{00} plot represents the retroreflectance of the screen for non-polarized light. As expected, it drops with the increase of incident angles. The normalized elements m_{11} , m_{22} and m_{33} have the largest absolute values which are averagely around 0.8, and the m_{22} and m_{33} have negative signs. The remaining elements of the Mueller matrix plots are generally small, which suggests that the retroreflective screen may has relatively low diattenuation effects. Fig 3.9 plots the diattenuation magnitude of a retroreflective screen. Retroreflective screen demonstrates little diattenuation across the FOV of 30° and its magnitude is smaller than 8% .

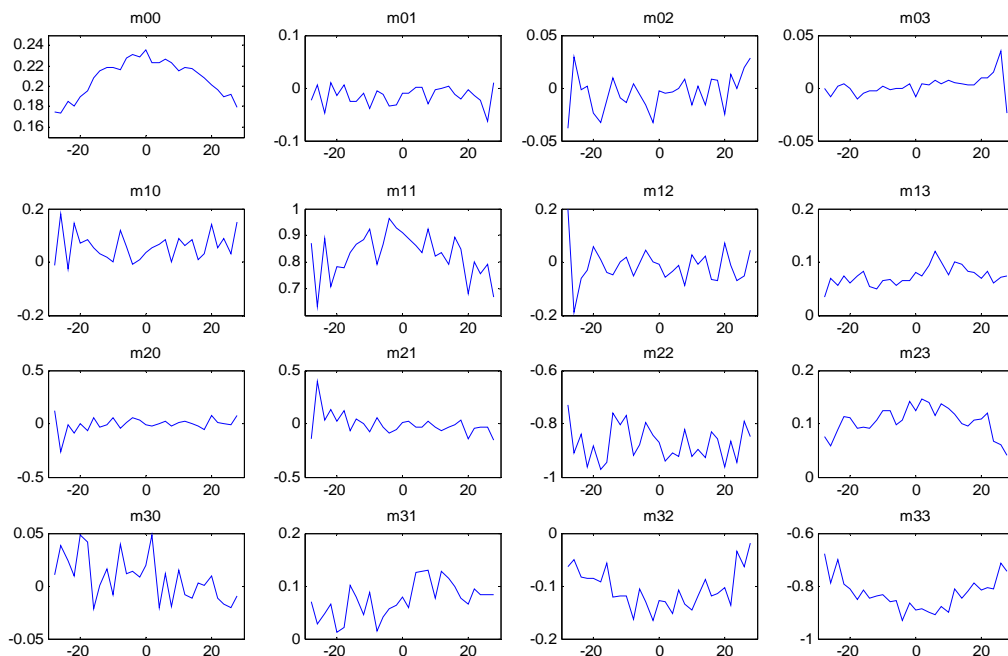


Figure 3.8 Normalized Mueller matrix plot for the retroreflection of a retroreflective screen at the wavelength of 550nm. The incident angle is from -28° to 28° .

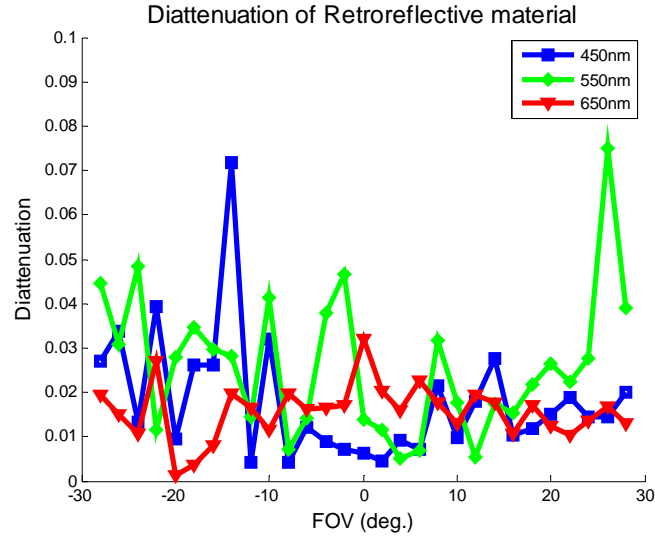


Figure 3.9 Diattenuation of a retroreflective screen

As shown in Figure 3.8, the retroreflection matrix is close to

$$M_{mirror} = \begin{bmatrix} 1 & 0 & 0 & 0 \\ 0 & 1 & 0 & 0 \\ 0 & 0 & -1 & 0 \\ 0 & 0 & 0 & -1 \end{bmatrix}, \quad (3.19)$$

which is the Mueller matrix for both mirror reflection and a horizontal half-wave linear retarder. The difference is that the mirror reflection does not introduce retardance into the incident light, and the coordinate of the light is changed instead. In the mirror reflection, assuming the z axis is vertical to the mirror surface, after the reflection z axis is changed to the opposite direction and one of the (x,y) local coordinates changes its sign to maintain the right-handed coordinate. Through the reflection, 45° polarized incident light becomes 135° polarized light while the direction of the electric field is still the same but in a different coordinate.

Since a mirror reflection matrix is included in the retroreflection matrix, to study pure retardance properties of a retroreflective screen, a Mueller matrix M''_{retro} without including reflection matrix can be obtained through

$$M''_{retro}(\theta, \lambda) = (M_{mirror})^{-1} M_{retro}(\theta, \lambda). \quad (3.20)$$

Through the decomposition of Mueller matrices (Lu & Chipman, 1996), the retardance of a retroreflective screen can be obtained as a function of FOV and wavelength. Figure 3.10 indicates that the retroreflective screen shows little retardance, the magnitude of which is smaller than 13 degrees.

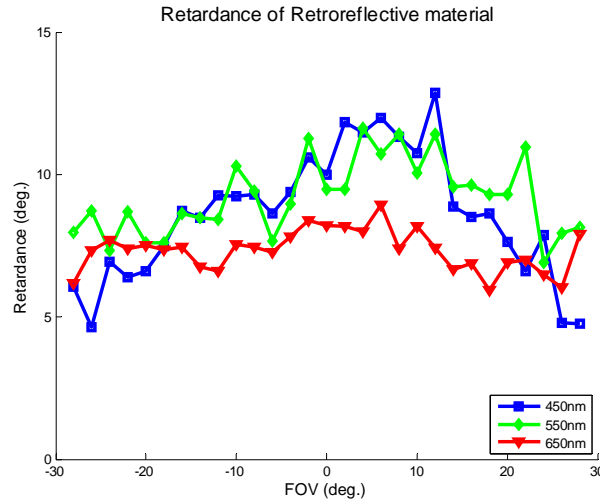


Figure 3.10 Retardance of a retroreflective screen

The depolarization magnitude of a retroreflective screen is quantified by the depolarization index

$$Dep = 1 - \frac{[\sum_{i,j} m_{ij}^2 - m_{00}^2]^{1/2}}{\sqrt{3}m_{00}} \quad (3.21)$$

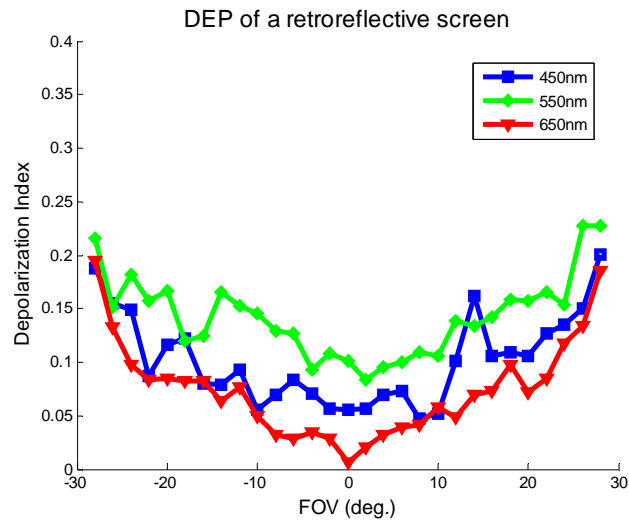


Figure 3.11 Depolarization index versus incident angles

Figure 3.11 plots the *Dep* of a retroreflective screen as a function of incident angle. The *Dep* is less than 15% for incidence angles within $\pm 20^\circ$ and is less than 23% for angles up to $\pm 28^\circ$. As a result, the retroreflected light remains dominantly the same type of polarization as its incident light, although the retroreflectance would be lower at large incident angles.

3.5 ANALYSIS OF OVERALL SYSTEM PERFORMANCE

Generally, the light emitted from the projection lens varies as a function of multiple factors, such as the light emission profile of the pixel, the throughput of the projection system, and the transmittance of the projection system, while these factors vary with microdisplay choices and lens system designs and should be taken into account during the design process to maximize the flux through the projection system. Since we mainly focus on the optical efficiency of a p-HMPD and HMPD, the light emitted from the

projection lens, which is considered as the input light in the following discussion, is assumed to be constant and linear polarized for both p-HMPD and non-polarizing HMPD and the luminous transfer efficiency mainly depends on the polarization characteristics of the elements after the projection lens in Figure 3.1.

3.5.1 Luminous transfer efficiency

The Mueller matrix of the overall p-HMPD system at a given FOV and wavelength is calculated through the multiplication of the corresponding Mueller matrices of each component. Following the optical path in the p-HMPD layout in Figure 3.1, the Mueller matrix of the p-HMPD is written as

$$M_{pHMPD}(\theta, \lambda) = M_{PBS-T}(\theta, \lambda)M_{retarder}(\theta, \lambda)M_{mirror}M_{retro}(\theta, \lambda)M_{retarder}(\theta, \lambda)M_{PBS-R}(\theta, \lambda) \quad (3.22)$$

where M_{PBS-T} and M_{PBS-R} are the transmission and reflection Mueller matrices of the PBS, respectively, and $M_{retarder}$ is the Mueller matrix of the quarter-wave retarder. In this equation, we assume the incident light from the projection system has a constant polarization state that is independent of FOV and wavelength for simplicity due to many engineering factors mentioned above. In the polarimeter, the z axis direction is defined by the light propagation direction. After retroreflection, the z axis direction becomes opposite while the x axis or y axis also changes its signs to maintain a right-handed coordinate. The coordinate change would affect the transmission Mueller matrices of the retarder and the PBS after the retroreflection. For example, the orientation of the fast axis of the retarder changes from 45° to 135° after retroreflection. To avoid such matrix change caused by the coordinate change, M_{mirror} is introduced into Equation 3.22 to

transform the new coordinate after retroreflection back to the coordinate before retroreflection.

To evaluate the performance improvement of a p-HMPD, we further calculate the Mueller matrices of a non-polarizing HMPD system which uses the same front-end projection system and microdisplays with a p-HMPD. The system uses a regular beamsplitter characterized in Section 3.4 and eliminates the quarter-wave retarder. As a result, the system Mueller matrix of an HMPD is written as

$$M_{HMPD}(\theta, \lambda) = M_{BS-T}(\theta, \lambda)M_{mirror}M_{retro}(\theta, \lambda)M_{BS-R}(\theta, \lambda) \quad (3.23)$$

Based on the Mueller matrices of the two systems, the overall luminance output through the system can be calculated by

$$\Phi(\theta, \lambda) = [1, 0, 0, 0] \cdot M_{system}(\theta, \lambda) \cdot S_{Incident} \quad (3.24)$$

where M_{system} is the system Mueller matrix, which can be written as M_{p-HMPD} for a p-HMPD and M_{HMPD} for a non-polarizing system, respectively. Φ represents the luminance efficiency of the system when the input Stokes vector has a unit luminance. $S_{Incident}$ represents the Stokes vector of the light from the projection system and it equals $[1, -1, 0, 0]^T$ for S-polarized light with a unit luminance and $[1, 1, 0, 0]^T$ for P-polarized light.

With the assumption of an S-polarized incident light, Figures 3.12(a) through 3.12(c) plot the luminance efficiency of a p-HMPD and a non-polarizing HMPD as a function of field angles at three different wavelengths. Figure 3.12(d) plots the ratio of the luminance efficiency of a p-HMPD to that of a non-polarizing HMPD as a function of field angle and wavelength. It indicates that on average the overall efficiency of a p-HMPD is about

two and half times of a non-polarizing HMPD throughout the entire FOV.

The luminance efficiency of a non-polarizing HMPD is further computed for a P-polarized input. The results clearly show that an S-polarized input yields higher luminance efficiency than a P-polarized input in a non-polarizing HMPD system. The luminance efficiency of a p-HMPD is averagely more than three times higher than that of a non-polarizing HMPD with a P-polarized input, which agrees well with the efficiency measurements directly obtained from two experimental prototypes in which P-polarized light was utilized in the non-polarizing HMPD setup (Hua & Gao, 2007).

3.5.2 Uniformity

As shown in Figure 3.12, the luminance efficiencies of both p-HMPD and non-polarizing HMPD systems decrease with the increase of FOV, owing to the angular dependence of the optical transformations for the key optical elements. The reducing efficiencies at large field angles directly result in lower luminance at the edge of the projected image than that of the image center. In order to quantify the image non-uniformity of the two systems, we calculate the average and the standard deviations (SD) of the luminance efficiencies as well as the normalized SD value across the FOV for the three wavelengths. The normalized SD value, which can be calculated through dividing the SD value by the corresponding average, is utilized to characterize the non-uniformity of the luminous efficiency across the FOV and to measure the image non-uniformity. The results are listed in Table 3.1. The normalized SD value of the p-HMPD system is lower than that of the non-polarizing system at the wavelength of

450nm, but is higher at the wavelength of 550nm and 650nm. It suggests that p-HMPD has higher image uniformity at the wavelength of 450nm but lower image uniformity at the wavelength of 550nm and 650nm.

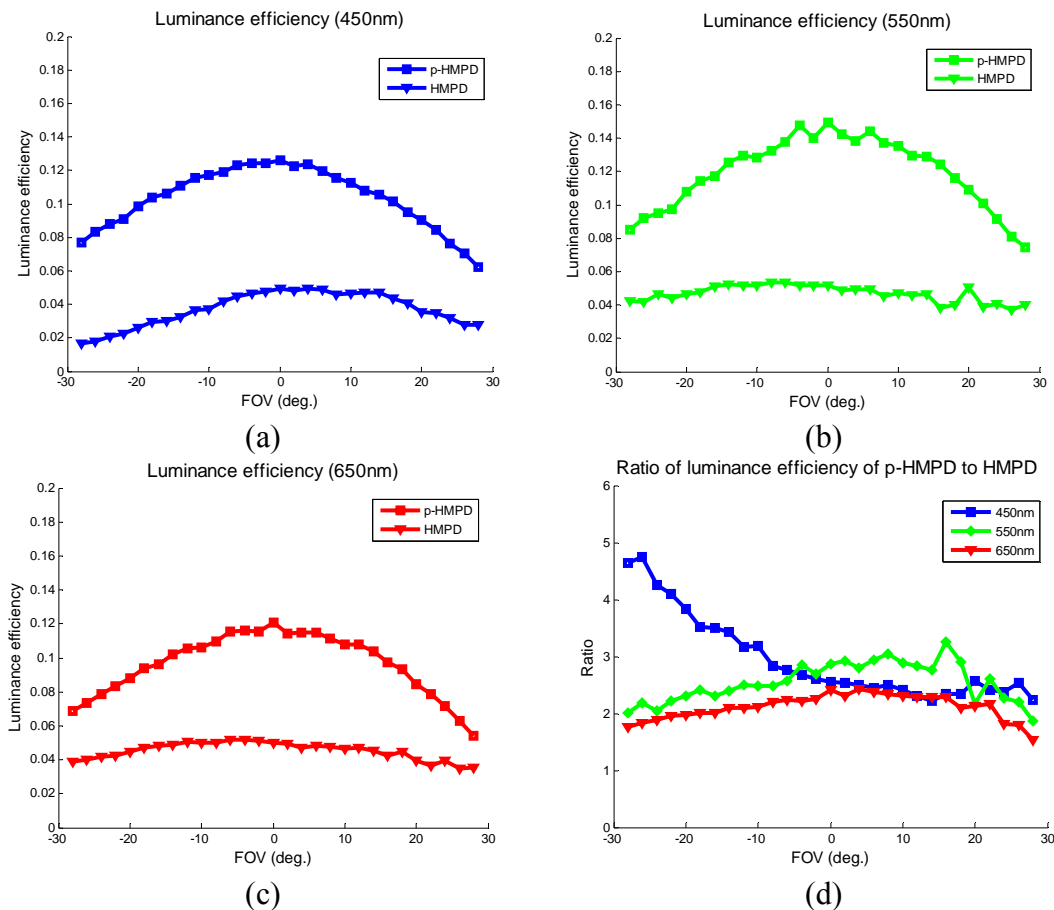


Figure 3.12 Luminance efficiency of a p-HMPD and a non-polarizing HMPD at the wavelength of (a) 450nm (b) 550nm and (c) 650nm. (d) The ratio of the luminance efficiency of a p-HMPD to an HMPD.

3.5.3 Contrast

The contrast of the projected image for both p-HMPD and HMPD systems is affected by the contrast of the microdisplay itself and the system transformation efficiency. In order to compare how the contrast of both systems is affected by their

luminous transfer efficiency, the microdisplay contrast is assumed to be 100:1. It is assumed that the output light of the display at white state is dominantly S-polarized and the output at dark state is unpolarized. Consequently, the stokes vector for the white state with a unit luminance is $[1,-1,0,0]^T$ and the stokes vector for the dark state is $[0.01,0,0,0]^T$, respectively. The output luminance values for both dark and white states were then calculated using Equation 3.24 for both p-HMPD and non-polarizing HMPD systems. The contrast value of a system is defined as the ratio of the output luminance at the white and dark states. The average contrast values across the entire FOV at three different wavelengths are listed in Table 3.1. It indicates that a p-HMPD system has higher image contrast than a non-polarizing system.

Table 3.1 Uniformity and image contrast: HMPD vs. p-HMPD

Wavelength	HMPD			p-HMPD		
	450nm	550nm	650nm	450nm	550nm	650nm
Average	0.037	0.047	0.045	0.103	0.119	0.096
SD	0.010	0.005	0.005	0.018	0.022	0.018
SD/Ave	0.27	0.106	0.11	0.17	0.18	0.18
Contrast	122.5	116.4	125.5	200.1	199.4	198.8

3.5.4 Colorimetric characteristics

The color representation of a display system, including non-polarizing HMPD and p-HMPD systems, is determined by both spectral properties of the microdisplay and the luminance transformation through the optical system. As shown in the Table 3.2 and in Figure 3.12, the overall efficiencies of both systems demonstrate considerable dependence on wavelengths, which could lead to chromaticity shift and reduced fidelity in color representation. To demonstrate how the colorimetric characteristics of the two

display designs are affected by different light propagation methods, we assume that the chromaticity coordinates of the red, green, and blue primaries as well as the white point for the microdisplays are the same as those of the standard sRGB display system (Stokes *et al.* 1996). Five fields, corresponding to $0, \pm 14^\circ$, and $\pm 28^\circ$, are used to represent the full FOV. Using the overall luminance efficiencies at the three different wavelengths at these five field angles, we calculated the chromaticity coordinates of the three primary colors and white point after propagating them through both display systems and the results are listed in Table 3.2. It indicates that the p-HMPD system not only shows less chromaticity shift than a non-polarizing HMPD system, but also better chromaticity uniformity since the chromaticity shifts demonstrate almost no dependence on the field angles in the p-HMPD system.

Table 3.2 Colorimetric characteristics: HMPD vs. p-HMPD

	FOV (deg.)	Red Primary (0.64, 0.33)	Green Primary (0.3, 0.6)	Blue Primary (0.15, 0.06)	White (0.3127, 0.3290)
HMPD	-28	(0.55, 0.39)	(0.28, 0.62)	(0.17, 0.07)	(0.2628, 0.3501)
	-14	(0.60, 0.36)	(0.29, 0.62)	(0.16, 0.07)	(0.2848, 0.3453)
	0	(0.64, 0.33)	(0.30, 0.60)	(0.15, 0.06)	(0.3113, 0.3348)
	14	(0.64, 0.33)	(0.30, 0.60)	(0.15, 0.06)	(0.3157, 0.3330)
	28	(0.61, 0.35)	(0.29, 0.62)	(0.16, 0.07)	(0.2941, 0.3513)
p-HMPD	-28	(0.64, 0.34)	(0.30, 0.62)	(0.15, 0.07)	(0.3177, 0.3598)
	-14	(0.63, 0.34)	(0.30, 0.62)	(0.15, 0.07)	(0.3159, 0.3591)
	0	(0.63, 0.34)	(0.30, 0.62)	(0.15, 0.07)	(0.3127, 0.3608)
	14	(0.63, 0.34)	(0.30, 0.62)	(0.15, 0.07)	(0.3105, 0.3619)
	28	(0.63, 0.34)	(0.30, 0.62)	(0.15, 0.08)	(0.3175, 0.3749)

3.6 SUMMARY

In chapter 3, the polarization elements were selected and analyzed. The polarization transformations for both a p-HMPD and a non-polarizing HMPD were characterized and the overall optical performance of two display systems was compared from the aspects of

luminance efficiency, image uniformity, image contrast, and color fidelity. The results indicate that the p-HMPD system has much higher luminance efficiency and higher image contrast than the non-polarizing HMPD system. The p-HMPD has higher image uniformity at the wavelength of 450nm, but lower image uniformity at the wavelength of 550nm and 650nm. Both systems show some level of color shifts on the three primary colors and white point due to the chromatic dependence of the luminous transfer efficiency. In comparison, the p-HMPD system not only shows less chromaticity shift but also better chromaticity uniformity than the non-polarizing system.

CHAPTER 4

DESIGN OF A P-HMPD SYSTEM USING FLCOS MICRODISPLAYS

Chapter 4 is partially based on a published article entitled “Design of a polarized head-mounted projection display using ferroelectric liquid-crystal-on-silicon microdisplays” (Zhang & Hua, 2008).

Chapter 4 presents a p-HMPD system using Ferroelectric Liquid Crystal on Silicon (FLCoS) microdisplays as the image sources. The design and evaluation of a compact light engine and a plastic projection lens, which are the two key parts of a p-HMPD system, are described in detail. Finally, we present a compact p-HMPD prototype using the custom-designed light engine and projection optics.

4.1 SELECTION OF MICRODISPLAYS

In older HMPD prototypes, a pair of 1.3” color AMLCDs were used as the image sources and these microdisplays have a resolution of $(640 \times 3) \times 480$ pixels and use 1.4” Alphalight RGB LED panels by Teledyne Inc. as the backlighting sources (Hua *et al.* 2000, 2003). When designing a new p-HMPD prototype, with the rapid development of display technology, it is critical to explore available microdisplay technologies that offer higher resolution, more compact packaging, and higher luminance output. Table 4.1 summarizes the main specifications of several candidate microdisplay technologies, including AMLCD, organic light emitting displays (OLEDs), liquid crystal on silicon

(LCOS) and FLCoS. It is worth noting that the data were collected from the website of the display manufacturers back to Feb. 2006 when we started to design a p-HMPD prototype. More details on recent technology progress are also added in the following discussion.

Table 4.1 Properties of microdisplays for HMDs*

	Active matrix LCD	OLED	LCOS (Type I)	LCOS (Type II)	FLCoS
Manufacturer	Kopin®	Emagin®	Brilliant®	Holoeye®	Forth dimension®
Size(diagonal) (inch)	0.97	0.61	0.75~0.86	0.364"	0.88
Resolution (pixel)	1280x1024	800x600	1600x1200	800x600	1280x1024
Contrast Ratio	100:1	100:1	2000:1	500:1	200:1
Pixel size (μm)	15 x 15	15 x 15	9.5 x 9.5	8.8 x 8.8	13.4 x 13.4
switching speed (ms)	<30	<1	11	1	0.04
Frequency (Hz)	60	Up to 85	Up to 120	60	60
Color method	RGB sub-pixels	RGB sub-pixels	Three R-G-B panels	Color sequential	Color sequential
Color depth (bit)	24	24	N/A	24	24
Illumination mode	Transmissive	Self-emissive	Reflective	Reflective	Reflective
Fill factor	<35%	~60%	~90%	~90%	~90%
Luminance (cd/m ²)	~100	>70	>1000 depends on the light engine	Up to 1000 depends on the light engine	Up to 1000 depends on the light engine
Optical efficiency	<10%	N/A	70%	60%	60-70%

*Data were collected in Feb. 2006

Compared with FLCoS and LCOS microdisplays, AMLCD offers a potentially more compact solution because its transmissive nature only needs a backlit panel rather than a complex illumination unit. However, it has relatively low contrast ratio and provides the lowest luminance range and largest pixel dimensions among all of the above technologies.

The self-emission nature of the OLED and its compact packaging offer potentially the most compact system design among these technologies. However, the resolution and contrast ratio of existing OLEDs are relatively low compared with FLCoS and LCOS microdisplays, and its life span would be shorter if the display luminance is too high (e.g. more than 100 cd/m^2). Another disadvantage is its relatively small panel size. For HMD designs, a display panel around one inch is preferred as it offers a good balance of compactness and the focal length range of the optics. When the display panel is too small, it requires a shorter focal length and larger magnification to achieve a reasonable FOV, which leads to a challenging design of a low F/# system. OLED technology has been developed rapidly in the recently several years. In 2009, Emagin released 0.77" SXGA OLED microdisplays and the luminance was improved to be higher than 150 cd/m^2 .

There are two types of LCOS microdisplays. The first type is the monochrome and high-resolution microdisplay developed in early 1990s. The liquid crystal used in LCOS microdisplays has low switching response at around 10ms. Such LCOS displays are widely used in three-panel architectures for rear projection television applications and digital projectors. The second type is the color-sequential microdisplay developed in late 1990s, and arranged in a single-panel. The switching time of the microdisplay is as fast as 1ms which makes it possible to generate 60HZ RGB color. Since an LCOS microdisplay operates in the reflective mode, an illumination unit is needed.

FLCoS offers high pixel resolution, high luminance output, high image contrast, and high optical efficiency. The ferroelectric liquid crystal has a fast response speed of 0.04ms. The ferroelectric liquid crystal could not be modulated continuously and only has

two states. As a result, both the gray scale levels and the color of FLCoS microdisplays are generated using a time sequential method. Similar to an LCOS microdisplay, it requires a carefully designed illumination unit to achieve high contrast and high luminance, which makes the overall display system less compact than a system using AMLCD or OLED microdisplays.

Digital Micromirror Device (DMD), developed by Texas Instrument, has been widely used in the digital projectors in recent several years. A DMD consists of up to millions of tiny microscopic mirrors, and each mirror represents one pixel in the image. The mirror can be tilted by 12 degrees to generate on and off states. Similar to FLCoS microdisplays, the gray scale of each color is controlled by the ratio of on-time to off-time. An illumination unit is required for a DMD system. Due to the 12 degree deflection angle between input and output light through DMD, the illumination unit is usually bulky. As a result, DMD is rarely used in a head mounted device.

Taking into account the pros and cons of the various technologies discussed above, we chose to use the SXGA-R2D FLCoS microdisplay kit by Forth Dimensional Displays Limited.

4.2 SYSTEM DESIGN OVERVIEW

The usage of FLCoS microdisplays makes the prototype design of a p-HMPD quite different from the older designs of HMPD optics (Ha *et al.* 2002; Hua *et al.* 2003). A key difference is the requirement for illumination units. The reflective FLCoS microdisplay requires a custom-designed front illumination system to illuminate the microdisplay. The

illumination unit for the microdisplay is called light engine which is a term commonly used in the projector industry. The FLCoS display is considered as the combination of a mirror and an electrically switchable quarter-wave retarder formed by the liquid crystal layer (Daniel, 2005). The retardance of the microdisplay is a function of the optical path length of rays through liquid crystal material. The FLCoS microdisplay works most efficiently when the illumination rays are normally incident upon the display surface. In normal incidence, all the rays experience the same optical path through the liquid crystal material, while skewed incidence leads to reduction of image contrast. To ensure a high contrast of the output image, it is recommended to limit the incident angle within the range of ± 16 degrees, which imposes a critical requirement on the design of both light engine and projection lens. One of the key requirements for the illumination engine is image-space telecentric so that for every pixel on the display surface the incident chief ray is normal to the display surface, the incident ray bundle is symmetric and the cone angle is smaller than 16 degrees.

Owing to the reflective nature of the microdisplay, the telecentric ray bundles incident upon the display surface will be mirror-reflected by the microdisplay. Thus the output ray bundles from every pixel of the microdisplay will be telecentric with a cone angle smaller than 16 degrees. To efficiently collect rays from the microdisplay and form a projected image with uniform illumination, it is required that the projection lens be image-space telecentric.

In summary, the key parts of a p-HMPD include an image-space telecentric light engine and an image-space telecentric projection lens. Both parts need to be compact and

light-weighted.

4.3 DESIGN OF AN ILLUMINATION UNIT

4.3.1 Light source and source modeling

The design of a head-mounted system sets several constraints on the light source selection and the light engine design. First, safety is a primary concern in any head-mounted devices. Therefore sources with low power consumption and low heat dissipation are highly desired. Second, compactness and lightweight are always critical for HMD systems. Finally, in order to generate an image with high brightness and uniformity across the whole FOV, the illumination on the microdisplay should be uniform and bright. With these considerations, a 0.5" Alphalight® color LED illuminator by Teledyne Inc. was selected for our p-HMPD prototype design.

The Alphalight illuminator is composed of a diffusive reflecting cavity, three LEDs with red, green, blue colors, diffusers and brightness enhancement film (Gleckman, 2000). As shown in Fig. 4.1 (b), three LEDs are enclosed in a diffusing housing and the light from LED sources undergoes several reflections within the cavity constructed from a diffusively reflecting material before eventually emerging from the aperture of the LED panel. A diffuser is placed at the aperture. As a result, the output light from three LEDs is uniformly distributed across the aperture and the aperture acts as a Lambertian source. To further concentrate the light into a small angle and increase the brightness at the small output angle, a brightness enhancement film is placed at the aperture. Figure 4.2 shows the intensity distribution as a function of the output angle.

The three LEDs in the illuminator are compatibly driven by the color sequential technique used in the FLCoS displays. The major specifications of the illuminator are summarized in Table 4.2.

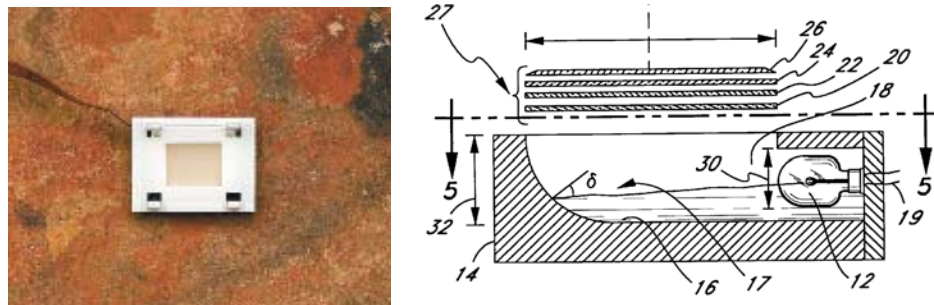


Figure 4.1 (a) Photos of a 0.5'' Alphalight LED illuminator (b) Structure of the LED illuminator (Courtesy of Teledyne).

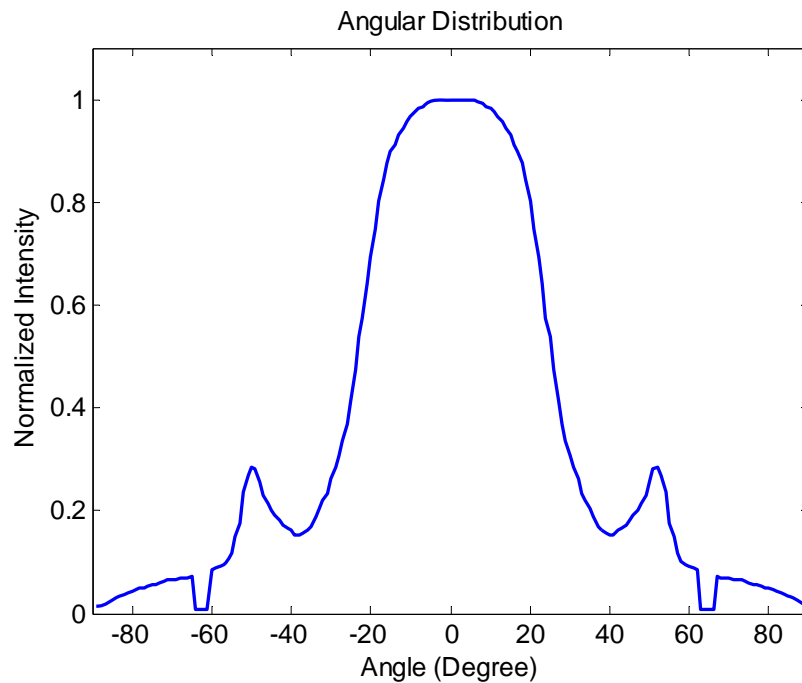


Figure 4.2 Angular distribution of the light as a function of angle

Table 4.2 Specifications of the microdisplay and LED illuminator

Parameters	Specifications
FLCoS microdisplay	
Diagonal size	22.3mm
Active area	17.43 x 13.95 mm
Resolution	1280x 1024 pixels
Pixel size	13.6 μ m
Color technique	Field sequential color
LED panel	
Body Dimensions	18.4 x 14.1mm
Active area	8.4 x 6.5mm
Weight	4 \pm .5 grams
Luminance	>34800 (cd/m ²) (full duty cycle)
Uniformity	<1.2:1
Color Coordinates	Red: x = .67~.43, y = .27~.33 Green: x=.14~.28, y = .64~.73 Blue: x = .11~.15, y = .04~.10
Power	340mW

4.3.2 Light engine designs

The design of illumination systems for reflective LCDs has been well explored in digital projector industry. The most two popular light engine designs include a lens array based design and an integrator rod based design (Robinson *et al.* 2005). The lens array based design uses a pair of fly's eye lens array system combining with condenser lenses to achieve uniform illumination with high efficiency on the microdisplays. The integrator rod based design uses an integrator rod to homogenize the light from LEDs and the output face of the rod is then relayed by several condenser lenses onto the microdisplay. However, both designs usually require a long optical path, i.e. 120mm at least, and are too bulky to be used for head-mounted applications. In the following sections, two compact designs of the light engine are presented and analyzed.

4.3.2.1 Design I: Double telecentric design

As discussed in Section 4.2, one of the key requirements for the illumination engine is image-space telecentric. LED illuminator provides a relatively uniform illuminance distribution across its aperture and the ratio of the maximum illuminance over the minimum is smaller than 1.2:1. Meanwhile the illuminator is highly concentrated around the normal incident angle and the rays within the cone angle of 23 degrees carry about 38.6% of the total energy. With these considerations, we present a compact design of a light engine using the concept of Abbe-illumination in which a light source is imaged directly on the microdisplay.

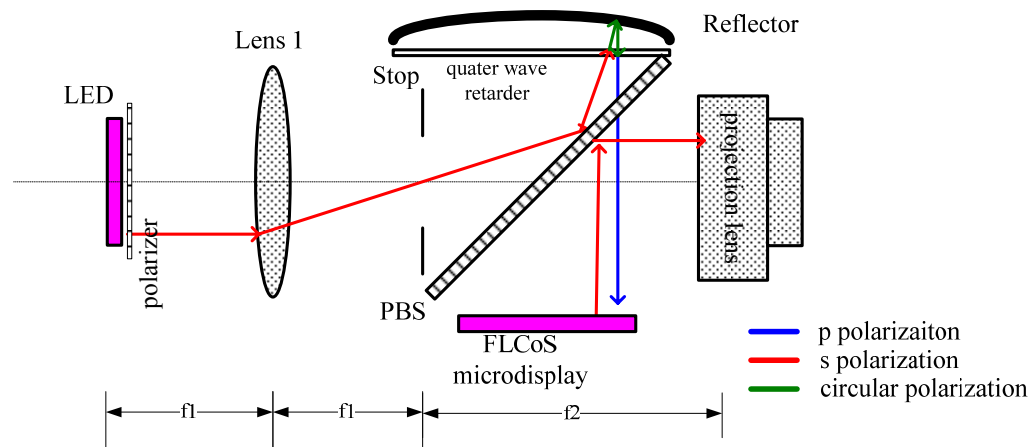


Figure 4.3 Design I: Double telecentric design of a light engine for an FLCOS microdisplay

Figure 4.3 illustrates the schematic design of the proposed design I of the light engine. This design, in addition to being an Abbe-illumination system, is a double telecentric system in which the chief ray (i.e. the ray passing through the center of the stop) is parallel to the axis of the system in both of the object and image spaces. The double telecentric is achieved by placing the stop at the common focal point of Lens I and

the reflector. Different from an ordinary double telecentric system composed of condenser lenses, in our system, an aspheric Fresnel lens is used for Lens I because of its feasibility of low $f/\#$ and light weight (Ruda *et al* 2005). The groove side of the Fresnel lens is set to face the LED to achieve higher light efficiency. A reflector, which is free of chromatic aberrations, is used as second optical element to fold the optical path to achieve a more compact solution.

Polarization elements are used in the design to increase light efficiency and achieve high contrast. A linear polarizer converts non-polarized light emitted by the LED panel into S-polarized source, which is reflected maximally by a PBS placed in front of the reflector. A quarter-wave retarder is placed between the PBS and the reflector and its fast axis is set to be at 45 degrees with the direction of S-polarized light. By passing through the retarder twice, the reflected S-polarized light is then converted into P-polarized light. The p-polarized light transmits through the PBS with a high efficiency and is incident on the microdisplay. The output light from the FLCoS microdisplay which is equivalent to a combination of a mirror and a quarter-wave retarder is S-polarized and will be reflected by the PBS and be collected by the projection lens.

Table 4.3 shows the first order data of the design. The LED panel is placed at the front focal point of Lens I and it forms an image on the FLCoS microdisplay which locates at the focal plane of reflector. The ratio of the reflector focal length (f_2) to the focal length (f_1) of Lens I is the same as the ratio of microdisplay size to that of the LED panel. The stop is used to limit the cone angle of ray bundle from each point on the LED, and it helps to make a uniform illumination on microdisplay. In our design, the stop size

is set to allow rays within the cone angle of ± 23 degrees to pass through system. Within this cone angle, roughly 38.6% of total energy will pass through the system. Considering the loss through a linear polarizer, theoretically 19.3% of total energy will be collected by the illumination optics to illuminate the microdisplay. Increasing the stop size and the cone angle can collect more energy, but compromise overall system compactness. In this double-telecentric design, the rays emitted normally from the LED panel surface, which have the highest luminance, are normally incident upon the microdisplay, yielding the most efficient reflection.

Table 4.3 First-order data of the light design

	Lens 1	Reflector
Focal length	15mm	35mm
Diameter	25mm	35mm
$f/\#$	0.6	1

	PBS	Retarder	Polarizer
Size(mm)	37 x 30	40 (Diameter)	8.4 x 6.5
Thickness(mm)	1.6	0.5	0.5

The optical magnification of the Abbe illumination system is given as

$$m = \frac{h'}{h} = \frac{f_2}{f_1} \quad (4.1)$$

where h and h' are the size of the LED panel and microdisplay, respectively. Considering the aspect ratio difference of the LED panel and microdisplays, the magnification in our design was set to be 2.3. The maximum ray angle incidence upon the microdisplay is calculated through the equation:

$$\mathcal{N} = uh = u'h' \quad (4.2)$$

where $u = \tan(\theta)$, $u' = \tan(\theta')$ and \mathcal{N} is a Lagrange Invariant. Here θ is marginal ray angle in the object space, and θ' is the marginal ray angle in the image space. As the stop size constrains the angle θ to be 23 degrees, through the equations 4.1 and 4.2, the angle θ' turns to be 10.5 degrees which is smaller than 16 degrees.

In order to better examine the light efficiency and illumination uniformity, the light engine design was modeled using LightTools® as shown in Figure 4.3. The emission profile of the LED panel was modeled using its angular intensity distribution data (Fig. 6.2), and the total power of the source was set to be 1 lumen. All the other components were modeled according to their optical properties and geometrical measurements of the real parts. A receiver was placed on the microdisplay to estimate the efficiency of the light engine and to evaluate the light distribution on the microdisplay. Figure 4.4 shows the output illuminance distribution on the microdisplay by tracing about 50 million rays through the system. The standard deviation of the illuminance distribution across the display area is about 4.5% and the maximum illuminance difference is about 23.8%. The total flux on the microdisplay is 0.11 lumens, which suggests that about 11% of the total energy emitted by the LED is collected by the microdisplay. The overall efficiency can be further improved with a compromise of a less compact design.

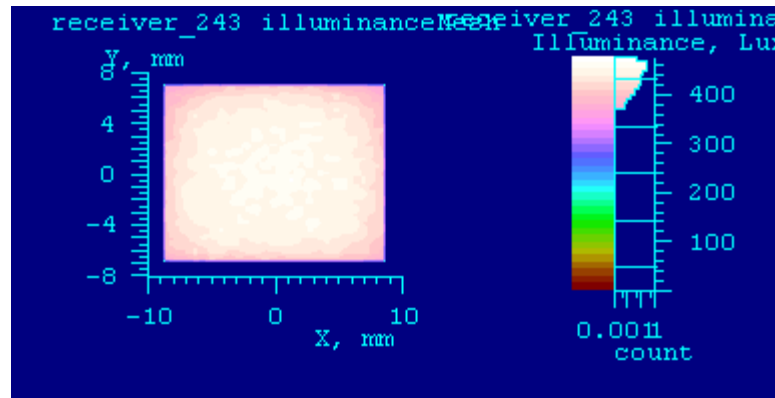


Figure 4.4. Illuminance distribution on the microdisplay for design I

4.3.2.2 Design II: Image space telecentric design

Since LED illuminator has a uniform illuminance distribution through its aperture, the luminance distribution of the LED source can be estimated by

$$L(\theta) \propto I(\theta) / \cos \theta \quad (4.3)$$

where $I(\theta)$ and $L(\theta)$ are the light intensity and the luminance as a function of emission angle θ , respectively.

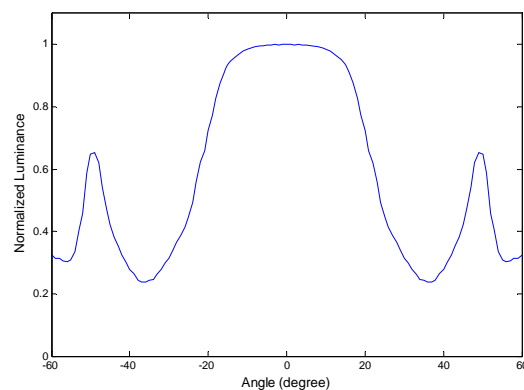


Figure 4.5 Luminance distribution of the LED illuminator as a function of emission angle

Figure 4.5 shows the luminance distribution of the LED illuminator as a function of emission angle. The luminance distribution is relatively uniform, and the luminance is highest in the normal direction of the panel and drops by about 17% at an 18° emitting

angle. Figure 4.6 shows the schematic design of the light engine which meets the requirements for image-space telecentricity, compactness, high efficiency, and uniformity. The LED illuminator is placed at the focal point of a concave reflector. In order to achieve a compact design, a PBS is used to fold the optical path in half and the microdisplay is placed conjugately at the focal point of the reflector. A polarizer is placed in front of the LED panel so that S-polarized light is reflected by the PBS toward the reflector. A quarter-wave retarder is placed between the reflector and PBS and its fast axis is set at a 45° angle with the S-polarized light. By passing through the retarder twice, the reflected light by the reflector becomes P-polarized and is transmitted through the PBS to illuminate the microdisplay with a high efficiency. An FLC_oS microdisplay functions as a quarter wave retarder and thus the P-polarized incident light becomes S-polarized through the microdisplay. This light is then reflected toward the projection lens by the PBS.

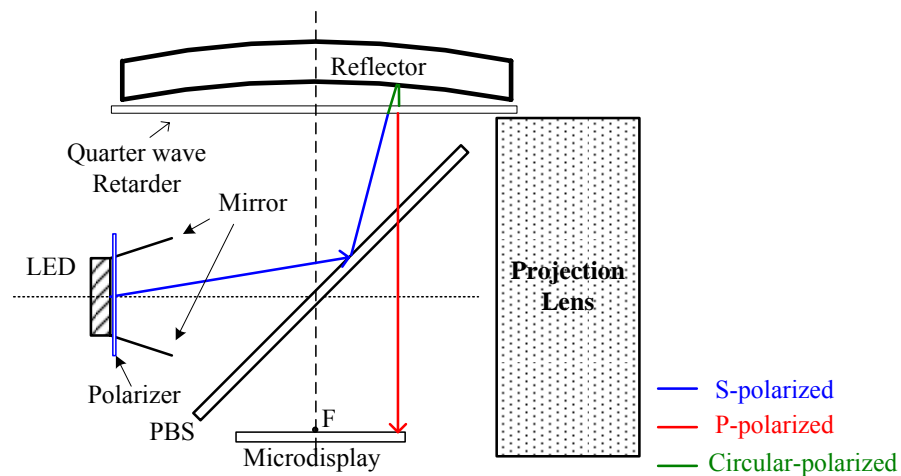


Figure 4.6 Schematic design of the light engine design II

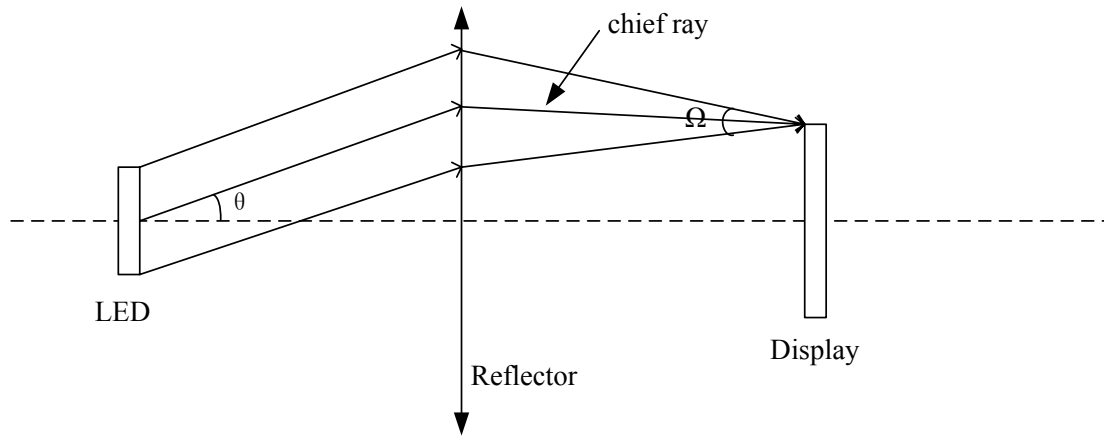


Figure 4.7 Simplified optical setup of the light engine design II

Figure 4.7 is the simplified optical setup of the light engine design II. The LED panel is actually set as the stop of the system to form an image-space telecentric system and the ray bundle received by the display is symmetric with the normal direction of the display surface. With both the source and the microdisplay at the focal point of the reflector, the spatial distribution on the microdisplay can be derived by

$$E_{display}(x, y) = L_{LED}(\theta) \times \Omega(x, y) = L_{LED} \left(\arctan \left(\frac{\sqrt{x^2 + y^2}}{f} \right) \right) \times \frac{S_{LED}}{f^2}, \quad (4.4)$$

where $E_{display}(x, y)$ is the illuminance at the position of (x, y) on the display, $\Omega(x, y)$ is the solid angle of the ray bundle incident at the position of (x, y) on the microdisplay, $L_{LED}(\theta)$ is the luminance distribution of the LED panel as a function of emitting angles, S_{LED} is the area of the LED panel and f is the focal length of the reflector. It is assumed that the center of the display is at the position of $(0, 0)$ and the normal of the display is aligned with the optical axis. As indicated by Equation 4.4, the solid angle of the ray bundle is a constant across the display and the illuminance is a function of angular

luminance of LED. The ratio of the illuminance at the center of the display to that at the edge is $L_{LED}(0^\circ) : L_{LED}\left(\arctan\left(\frac{D}{2f}\right)\right)$ where D is the diagonal size of the display.

To achieve a higher uniformity on the display, a reflector with a longer focal length is preferred. A longer focal length, however, will compromise compactness and optical efficiency due to a smaller solid angle. Considering these tradeoff factors, we selected a reflector with the focal length of 35mm and the diameter of 40mm. As a result, the light within the half cone angle of 18° emitted by the LED panel can be collected by the reflector to illuminate the display while the light at larger angles is wasted. The half cone angle of the ray bundle incident on the display is well constrained within 8.6° , while the ratio of the maximum luminance to the minimum luminance on the display is 1:0.83.

In order to reduce the anticipated non-uniformity and further improve the uniformity and the efficiency of the light engine, we designed a mirror-based tapered light pipe to recycle the light with an emission angle larger than 18° and homogenize the light distribution across the display panel. The light pipe is composed of four mirrors, each of which is tilted by an angle α , with the LED surface, forming a truncated pyramid shape. Through four mirrors, four LED images are formed. Fig 4.8(a) demonstrates how the mirror light pipe improves the optical efficiency. To collect the light with an emission angle larger than 18° , two constraints need to be met. First, the rays virtually emitted from mirror image of the LED need to pass through the mirror. Second, the output ray angle is constrained within the cone angle θ_0 (i.e. 18°) so that rays can be collected by the reflector. For example, for a given point T on the mirror image of the LED, the light

emitted within the region TSR could be recycled by the light pipe and collected by the reflector to illuminate the microdisplay. The boundary TS is set by the physical boundary of the mirror and the boundary TR is set by collection angle θ_0 (i.e. 18°) of the reflector. Figure 4.8(b) shows a prototype of the tapered light pipe with mirrors.

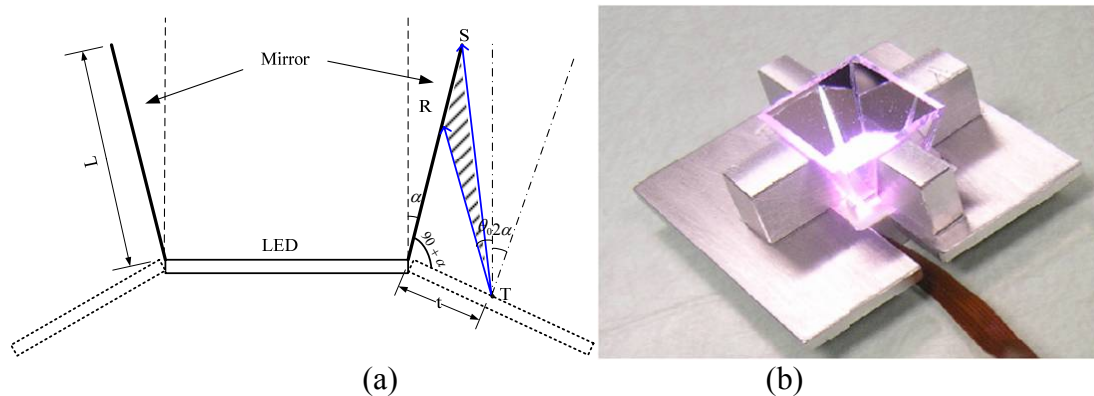


Figure 4.8 Tapered light pipe with mirrors: (a) Schematic design and (b) Prototype picture

Both the tilt angle α and the length L of the mirrors, as shown in figure 4.8(a), need to be optimized to maximize the uniformity and efficiency of the light engine. To obtain the optimal configurations for the above-mentioned parameters of the tapered light pipe and to examine the light efficiency and uniformity of the light engine, we modeled the light engine using LightTools®. The emission profile of the LED panel was modeled using its angular intensity distribution data. In the simulation, the total power of the source was set to be 1 lumen. A light receiver was placed on the microdisplay to estimate the efficiency of the light engine and to evaluate the light distribution on the microdisplay.

The non-uniformity, quantified by the average standard deviation of the illuminance distribution across the display area, and the optical efficiency, quantified by the ratio of

the received lumen on the microdisplay over the output lumen from the LED source, are evaluated as a function of the tilt angle α and the mirror length t . Figures 4.9 (a) and (b) show the non-uniformity and optical efficiency of the light engine as a function of the tilt angle. It is found that the light engine has the best uniformity and relatively high optical efficiency when the mirror tilt angle α is at 18° . Figure 4.10 (a) and (b) show the non-uniformity and optical efficiency of the light as a function of the mirror length. The light engine has the best uniformity and relatively high optical efficiency when t is 8mm. By balancing the performance and space constraint of the light engine, the mirror length t was selected to be 8mm.

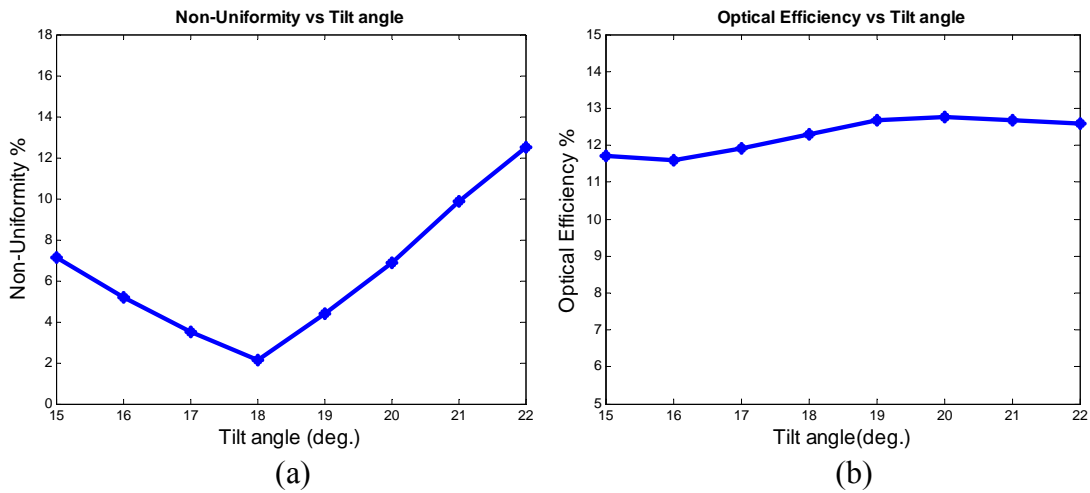


Figure 4.9 Effects of the mirror tilt angle on the (a) Non-uniformity and (b) Optical efficiency of the light engine

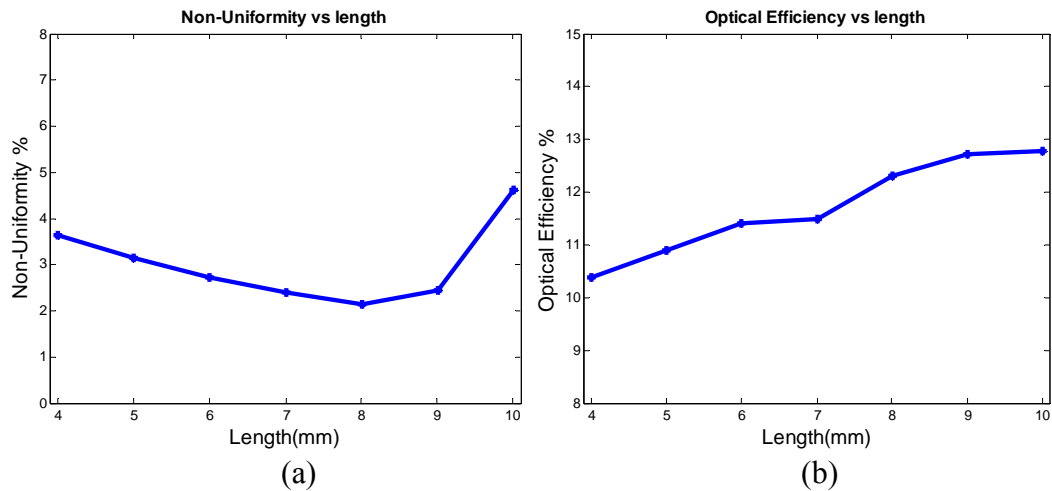


Figure 4.10 Effects of the mirror length on the (a) Non-uniformity and (b) Optical efficiency of the light engine

Figure 4.11(a) and (b) show the output illuminance distribution on the microdisplay without the light pipe and with the light pipe at the optimal angle and length, respectively. As indicated by the simulation results, the light efficiency of the light engine integrated with the tapered light pipe increased from 8.93% to 12.3%, and the non-uniformity was reduced from 5.61% to 2.15%.

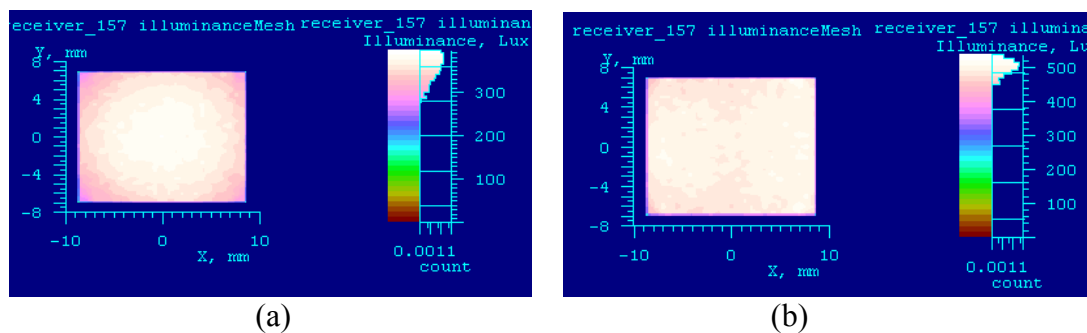


Figure 4.11. Simulated illuminance distribution on the display (a) Without light pipe and (b) With the light pipe

4.3.2.3 Further Analysis of Design II

By comparison of two designs of the light engine, the second design has more

compact structure and has almost half length of the first one. Meanwhile with the tapered light pipe, the second design also has better uniformity and optical efficiency than Design I. As a result, the second design is selected as the final design of the light engine.

Through the polarization management, the optical path is folded and the overall length of the light engine is reduced. However, one drawback of such design is the reduced contrast. As shown in figure 4.12, due to the polarization leakage of the PBS, a small amount of light from the LED passes through the PBS directly and is mixed with the S-polarized light from the microdisplay, which leads to the reduced image contrast. The light from the LED includes both P-polarized light and S-polarized light. Table 4.4 shows the percent of light from LED passing through the PBS directly assuming the light from LED source is completely unpolarized. The results show that the luminance of the light is 0.17% of LED luminance when the microdisplay is off. Table 4.5 lists all the factors that contribute to the light loss through the light engine and the luminance efficiency of the light engine is around 12.7% when the microdisplay is in white state. Based on the calculation, the image contrast is given by $12.7\%:0.17\%=75:1$. The contrast can be further improved to be around 150:1 after the reflection of the PBS which locates behind the projection lens by blocking the P-polarized light from the LED.

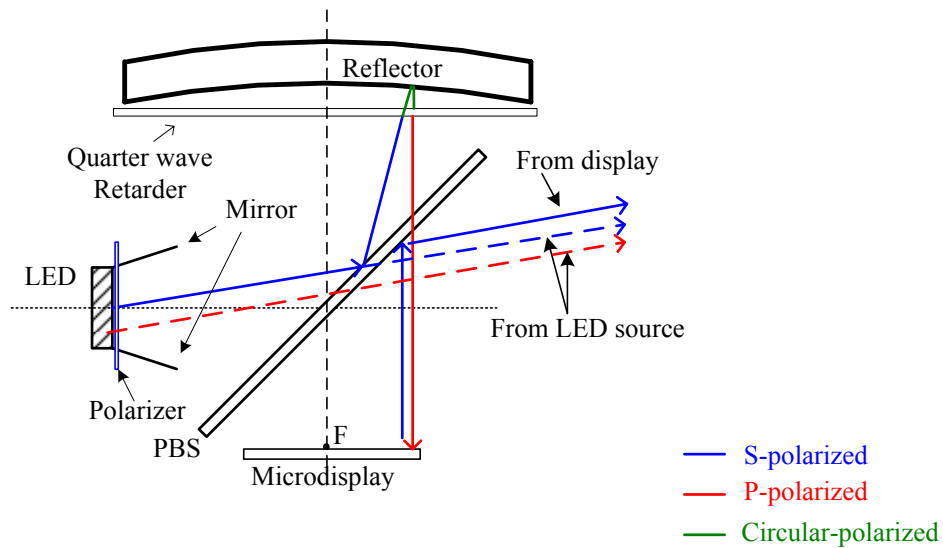


Figure 4.12 Reduced contrast due to polarization leakage in the light engine

Table 4.4 Percent of luminance from LED directly

Parameters	Specifications
S-polarized light	50%
Transmittance of PBS	85%
Polarizer @ LED	0.2%
P-polarized light	50%
Polarizer @ LED	0.2%
Transmittance of PBS	85%
Overall leakage	0.17%

Table 4.5 Percent of luminance through the microdisplay

Parameters	Specifications
S-polarized light	50%
Polarizer @ LED	85%
Reflection of PBS	90%
Transmittance of retarder	90%
Mirror reflection	90%
Transmittance of retarder	90%
Transmittance of PBS	85%
Efficiency of FLCoS display	60%
Reflection of PBS	90%
Overall	12.7%

4.4 DESIGN OF A PROJECTION LENS

Based on the design of a light engine, a lightweight and compact image-space telecentric projection lens was designed. In this section, the design process of the projection system is described.

4.4.1 Lens specification

The size of a projection lens does not scale as much as eyepiece-type optics with the increase of FOV, thus it is relatively easier to design wide FOV, optical see-through HMPD systems than conventional HMDs. There are still several factors that impose limits on the FOV of HMPD systems. First, the use of a planar PBS or a regular beamsplitter oriented at 45° with the optical axis sets the FOV upper limit to 90° . Second, a wide FOV requires a large-sized PBS and retarder, which consequently challenge the compactness and lightweight of the display system. The limit of allowable PBS and retarder dimensions is set by the interpupillary distance (IPD), which is in the range of 55 to 75 mm for over 95% of the population. Third, previous investigations on retroreflective materials show that the retroreflectance of currently available materials drops off significantly for light incident at angles beyond $\pm 35^\circ$ (Hua *et al.* 2003). A FOV beyond 70 degrees will inevitably cause vignetting-like effect and compromise image uniformity. Finally, the angular resolution of the display degrades with the increase of the FOV. Taking into account these factors, we aimed to design a projection system with a FOV of 55° , which corresponds to an effective focal length (EFL) of 21.6mm for the selected

FLCoS microdisplays.

In addition to the requirement of image-space telecentricity, the projection lens requires a large back focal length (BFL) to ensure enough space for a PBS which is placed between the microdisplay and projection lens (Figure 4.6). Based on the light engine design described in Section 4.3, the BFL is chosen to be at least 30.5mm. Since the BFL is longer than the effective focal length, this projection lens is also a reverse telephoto lens.

The so called entrance pupil of the projection lens is actually the exit pupil of the projection lens in a p-HMPD. In a lens design program, such as CodeV, the display plane is set to be the image plane and the exit pupil of the lens in a p-HMPD becomes the entrance pupil in the lens design program. The entrance pupil of the projection lens should be large enough so that most of the light from the display is collected. In other words, the throughput of the lens should match the throughput of the light engine. The Lagrange invariant of the light engine and the projection lens are calculated to determine the entrance pupil diameter (EPD) of the lens. For a projection lens with a FOV of 55°, the maximum chief ray angle is 27.5°. For the LED source, the maximum chief ray is 18° as shown in Section 4.3 and the diagonal size h_{LED} of the LED is 10.4mm without considering the light pipe and is 17.4mm if the light pipe is considered. Using the Lagrange invariant

$$\mathfrak{N} = h_{LED} \cdot \sin(18^\circ) = EPD \cdot \sin(27.5^\circ), \quad (4.5)$$

EPD is calculated to be 7.0mm for the case without considering the light pipe and 11.6mm for the case considering the light pipe area. Meanwhile, it is more challenging to

design a lens with a larger EPD. By balancing different factors, the lens aperture is selected to be 10mm, which leads to a projection system with an F/# of 2.16. The specifications of the projection system are summarized in Table 4.6.

In a p-HMPD, a user's eye is positioned at the conjugate position to the entrance pupil of the projection lens. In other words, the exit pupil of a p-HMPD is the image of the entrance pupil of the lens through the retroreflective screen. Due to the diffraction properties of a retroreflective screen which will be discussed in Chapter 6, the EPD of a p-HMPD is larger than the EPD of the lens if the ray bundle from the microdisplay fills the whole aperture of the lens. The EPD of the p-HMPD prototype will be measured directly in Section 4.6.

Table 4.6 Specification of the projection lens

Parameter	Specification
Projection lens	
Effective focal length	21.6 mm
Entrance pupil	10 mm
Eye relief	21 mm
Image mode	Image space telecentric
BFL	30.5 mm
FOV	55°
Wavelength range	486—656 nm
Distortion	<4% over FOV

4.4.2 Lens design and optimization

4.4.2.1 Starting point

After initial trials of optimization from several patent lenses, we selected a US patent lens by Norihiro Nanba (Nanba, 2001) as the starting point, as shown in Figure 4.13. This patent lens, designed for a digital projector, meets our requirements for reverse-telephoto and telecentricity. Unlike a typical double Gauss lens, the lens system

has an asymmetric structure relative to the stop because of the telecentric requirement in the image space. This five-element system offers a full FOV of 65° with an F/# of 2.5. Among the five glass elements, a doublet is used to correct chromatic aberration and the front surface of the last element is aspheric to help correct spherical aberration. The ratio of the BFL to the EFL of the lens is 1.13 and the ratio of the overall length (OAL) of the optics to the EFL is 3.15. The ratio of the exit pupil distance to the EFL is 13.6, which makes the system telecentric in the image space. After scaling the lens and several cycles of optimization with CODE V®, we obtained a starting lens system with 21.6mm EFL, 30mm BFL, 68 mm OAL, and 55° full FOV, as shown in Fig 4.14(a). As indicated in Fig. 4.14(b), the MTF of the lens is around 30% at the spatial frequency of 37cycles/mm which corresponds to the threshold spatial resolution of the FLCoS microdisplay and it is acceptable as a starting point for the design.

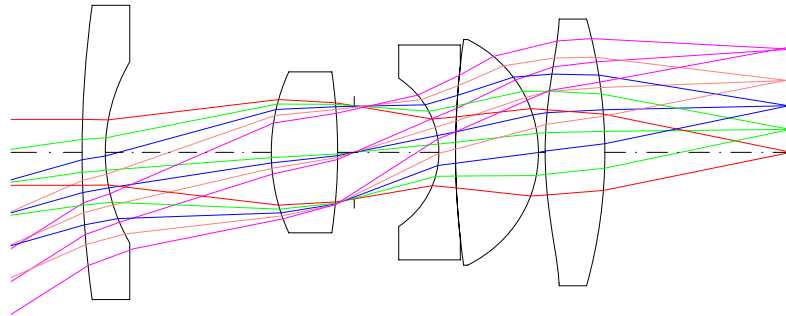
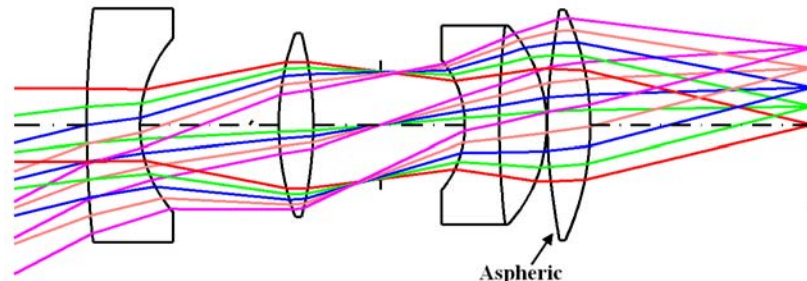
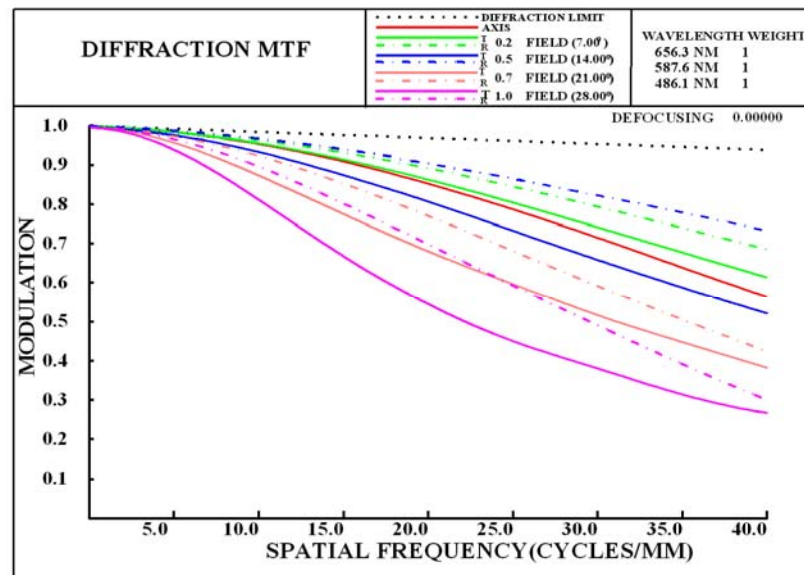


Figure 4.13 Layout of the starting patent lens



(a)



(b)

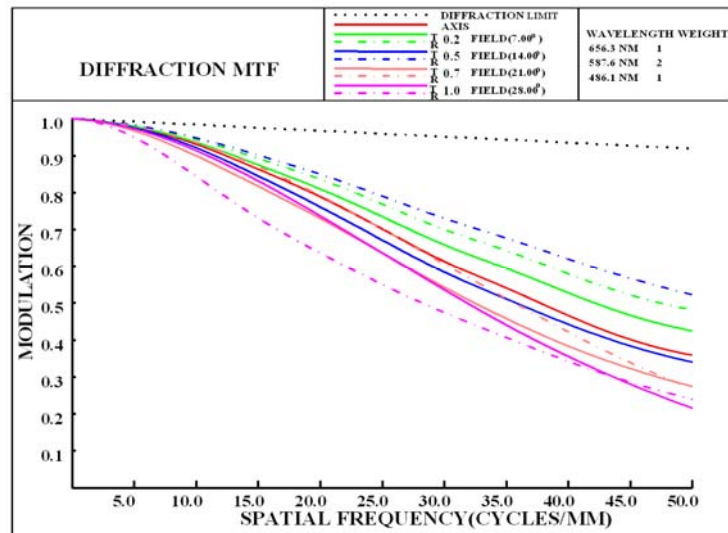
Figure 4.14. Starting lens: (a) Layout and (b) MTF performance

4.4.2.2 Optimization process

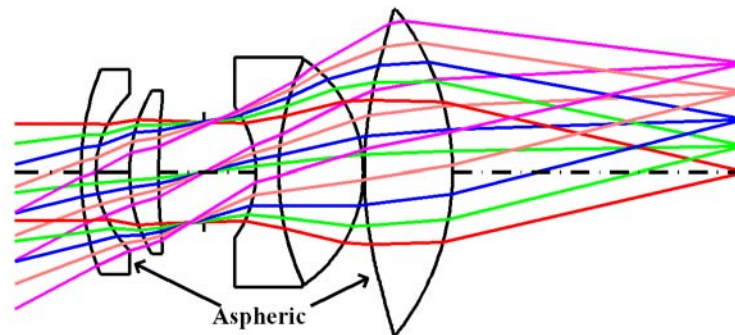
Due to the rotational symmetry of the system, the optimization is necessary only over half of the full FOV in the radial direction. Five visual fields, 0, 0.25, 0.5, 0.75, and 1 (i.e. on axis, 7, 14, 21, and 27.5 degrees, respectively) were selected in the optimization process to sample the whole FOV. The weights for these five fields were adjusted accordingly during the optimization process to balance the MTF performances across the entire FOV. Three representative wavelengths, 486nm, 589nm and 656nm, were set with

the weights of 1, 2 and 1, respectively. During the optimization, all the surface curvatures, the surface thickness, and the coefficients of aspheric surfaces were set to be variables. Several constraints were set to satisfy the specifications of the overall system and each individual lens, including the EFL, BFL, OAL, distortion requirements, and the center thickness of individual elements. The telecentric requirement was satisfied by setting the exit pupil distance to be at least 210mm from the image plane. This distance corresponds to a deviation of the chief ray by 3° from a perfectly telecentric system, which yields a good balance between the overall optical performance and the system compactness considering the difficulty in designing a perfectly telecentric lens with a short OAL.

One of the major problems of the lens in Figure 4.14(a) is its compactness: the OAL is too large for a head-mounted system. A more compact solution is needed. This initial system was gradually optimized by adjusting the parameter constraints and field weights through a local optimization approach. While the OAL was reduced down to about 40mm in the process of optimization, the overall performance was degraded as well. In order to further improve its performance, the back surface of the first lens was set to be aspheric, which helped to correct most of the spherical aberration. After gradual optimization, a system with satisfying performance was obtained. The lens layout and MTF are shown in Figure 4.15. This lens system is composed of five glass elements and weighs about 38.7 grams, which needs to be significantly reduced to obtain a lightweight p-HMPD system.



(a)



(b)

Figure 4.15 Intermediate compact design: (a) Layout and (b) MTF performance

Considering that the density of glass is typically three times of most plastic materials, we used plastic materials to replace the glass elements with the expectation that the weight of the lens would drop to around 10 grams. The drawback of using plastic materials over glasses is that only a very limited number of plastic materials are available for the diamond turning fabrication while a much wider range of glass options can be chosen for aberration balancing. The initial target was to replace the large aperture glass

elements on the right side of the stop with plastics as they contributed the most weight. Two plastics, polystyrene with a low Abbe number and Cyclic Olefin Copolymer (COC) with a relatively high Abbe number were selected to replace the glass materials of the doublet. COC was selected for the last element considering that it has the highest optical power among all the elements in the lens group and high Abbe number. After a few trials of optimization, it became evident that chromatic aberration dominates the resulting system.

To effectively correct the residual chromatic aberration, we decided to introduce a diffractive optical element (DOE) to the system. A DOE can be viewed as a material with large dispersion but opposite in sign to conventional materials (i.e. the Abbe number of a DOE is approximately -3.5 for the visible spectrum). The DOE replaced the functionality of a doublet for correcting chromatic aberration. The substrate shape of a diffractive surface can be spherical or aspheric. The commonly used orders of diffraction are 0, -1, or +1 and the +1 order of diffraction was adopted in this system. After a few trials, it was found that the most effective aberration correction was achieved with the DOE placed on the left surface of the last element. The DOE quadratic coefficient was constrained so that the DOE surface was not over-curved for fabrication concerns and other coefficients were set to be variable up to 12 orders in the optimization process. After finding a well-performed design through optimization, we replaced the first two glass elements on the left of the stop with Acrylic and Polystyrene, respectively, to further reduce the lens weight. Considering the higher fabrication cost of a doublet, we further split the doublet into two single elements, which offered extra freedom in the optimization and helped

improve the overall performance. Finally, through several rounds of optimization, a telecentric lens was obtained with an OAL of 34mm and a total weight of 8.2 grams. Figure 4.16 shows the layout of the final design of the projection lens.

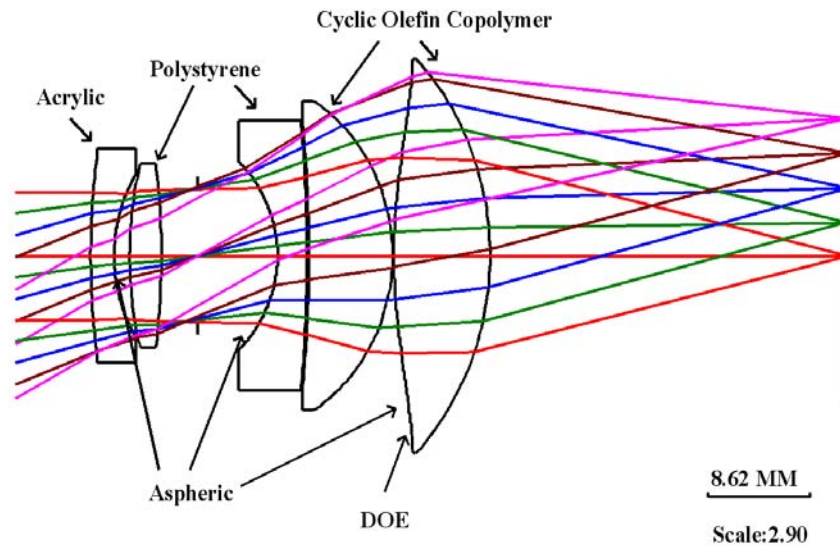


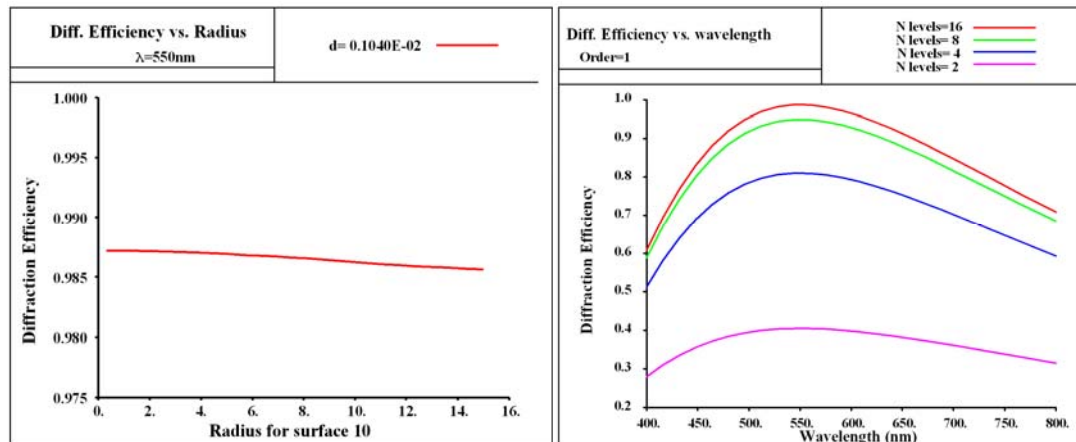
Figure 4.16 Layout of the final design of a projection lens

4.4.3 Performance analysis of the projection lens

4.4.3.1 DOE efficiency

The diffraction efficiency of a DOE drops as its physical features become finer near the edge. Figure 4.17 (a) shows the diffraction efficiency as a function of the radius of the diffractive surface at the designed wavelength of 550nm. The overall efficiency varies from 98.7% at the center to 98.5% at the edge. The diffraction efficiency is also wavelength dependent. Figure 4.17(b) plots the diffraction efficiency as a function of wavelength as well as the level of binary masks (i.e., 2, 4, 8, 16). A 16-level binary mask yields an accurate approximation for the Kinoform DOE produced through a diamond

turning fabrication method. The plot shows that the diffraction efficiency varies from 80% to 100% across the visible spectrum.



(a)

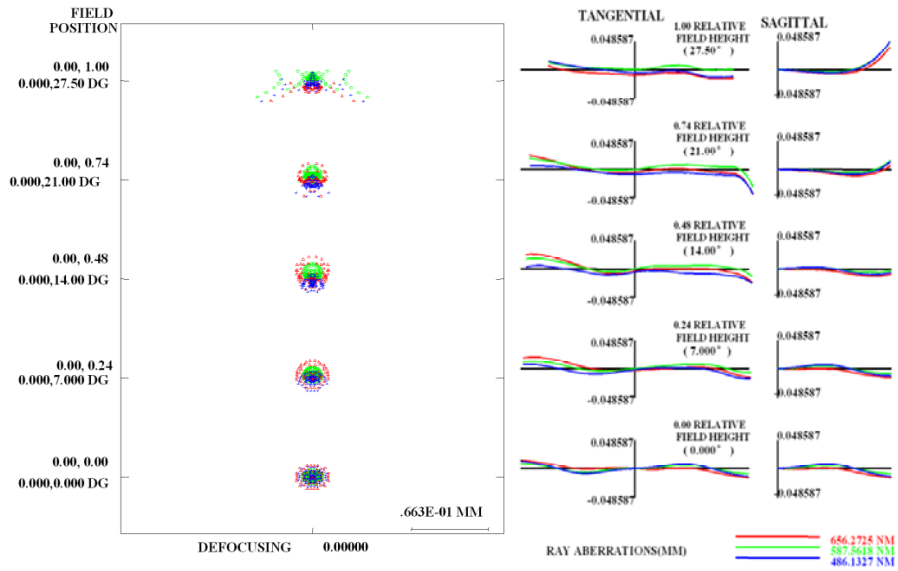
(b)

Figure 4.17 (a) Diffraction efficiency versus radius and (b) diffraction efficiency versus wavelength.

4.4.3.2 System performance in the microdisplay space

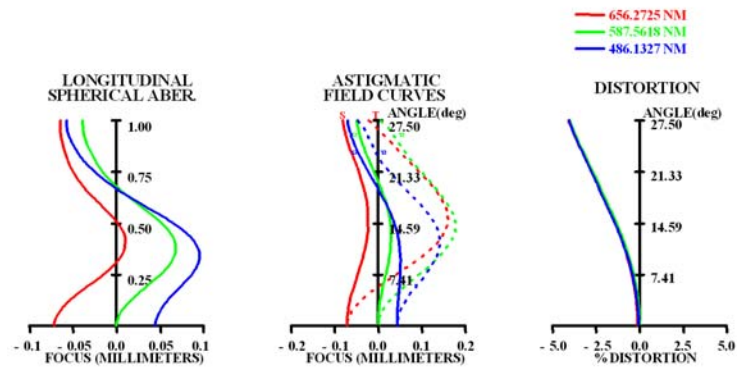
The optical performance of the optimized lens is assessed on the image plane at the five representative field angles for the three design wavelengths. The spot diagrams are shown in Figure 4.18(a). The average RMS spot diameter across the FOV is around $16\mu\text{m}$, which is slightly larger than the $13.6\mu\text{m}$ pixel size to avoid pixellated artifacts. Both the tangential and sagittal rayfans across the five fields are plotted in Figure 4.18(b), which demonstrates very low residual aberrations. Figure 4.18(c) shows the longitudinal spherical aberration, astigmatism, and distortion curves. The longitudinal spherical aberration and astigmatism are well balanced, and the distortion of the system is less than 4% across the FOV. The MTF of the lens is presented in the Figure 4.18(d). The FLCoS display has a threshold spatial frequency of 37cycles/mm given a $13.6\mu\text{m}$ pixel size. The

modulation is about 40% at 37cycles/mm across the whole FOV, which means the performance of the system is currently limited by the display resolution.

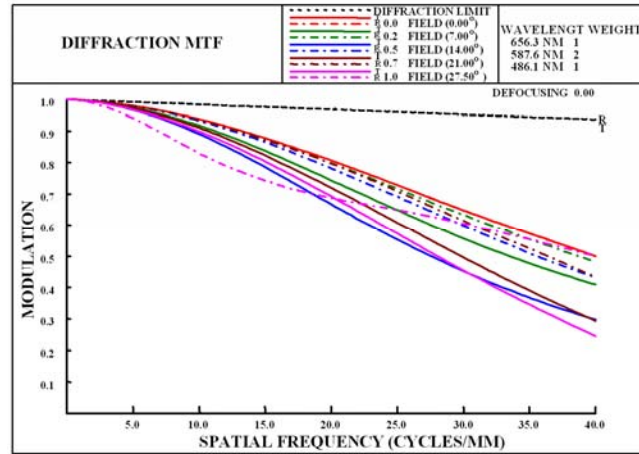


(a)

(b)



(c)



(d)

Figure 4.18 Lens performance of the optimized design: (a) spot diagram; (b) rayfan plot; (c) longitudinal spherical aberration, astigmatism and distortion; and (d) MTF performance.

4.4.3.3 Tolerance analysis

The diamond turning method was selected for the lens fabrication over the molding approach. Taking into account the cost and the fabrication capability of a typical single-point diamond turning process, the manufacturing errors were set as shown in Table 4.7. The image distance was set as the compensator and the MTF performance was used as the merit function in the tolerance process. Figure 4.19 shows the cumulative probability plot of the MTF at 37cycles/mm based on the manufacturing error in Table 4.7. The plot suggests that the MTF degradation at a given 97.7% cumulative probability is -2.95%, -1.64%, -2.34%, -7.89%, -8.69% at the five representative angles from 0° to 27.5°, respectively, which is acceptable for our system.

Table 4.7 Estimated errors in the fabrication

Tolerance type	Value
Thickness of the lens	10 μ m
Distance of the air gap	10 μ m
Delta of refraction index	0.001
Test plate fit	2 waves
Wedge of lens	2 μ m
Lens tilt	0.0002 radians
Decenter of lens	5 μ m

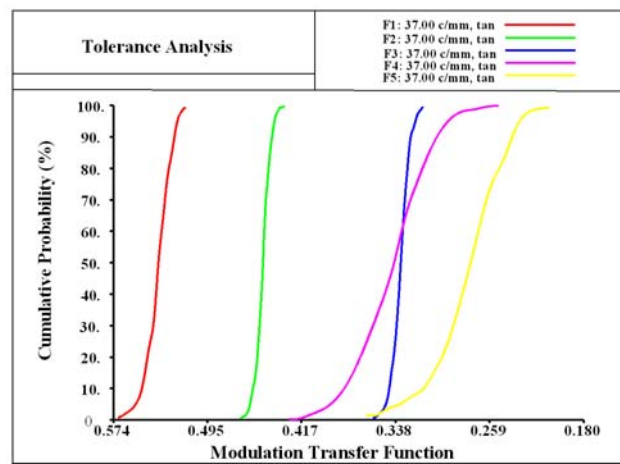


Figure 4.19 Cumulative probability plot for MTF tolerance.

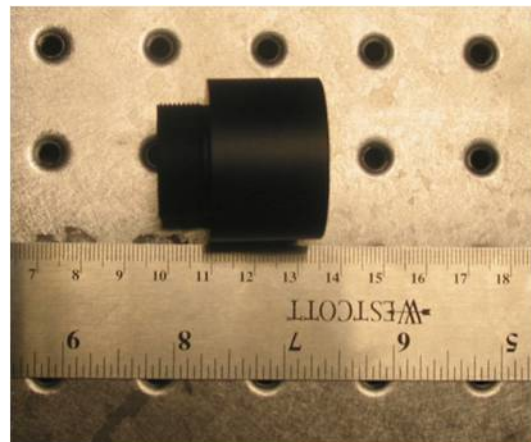


Figure 4.20 Prototype of the projection lens.

4.5 TESTING OF THE PROJECTION LENS

In this section, we measured the MTF performance of the projection lens and evaluate the polarization properties of the lens.

4.5.1 MTF testing of the lens

The lens was fabricated using diamond turning technique and assembled by Apollo Optical System. The lens prototype is shown in Figure 4.20. We measured the edge response functions of the lens at various field angles to evaluate the MTF of the lens prototype using software called Imatest. Figure 4.21 shows the measured MTF performance of the lens prototype for a set of tangential fields. The measured MTF of the lens is about 20% at 37cycles/mm across the whole FOV, which is acceptable for our application. Compared with the MTF performance predicted for the optimized lens, the MTF degradation of the prototype is mainly caused by the tolerance in the lens fabrication procedure and assembly procedure.

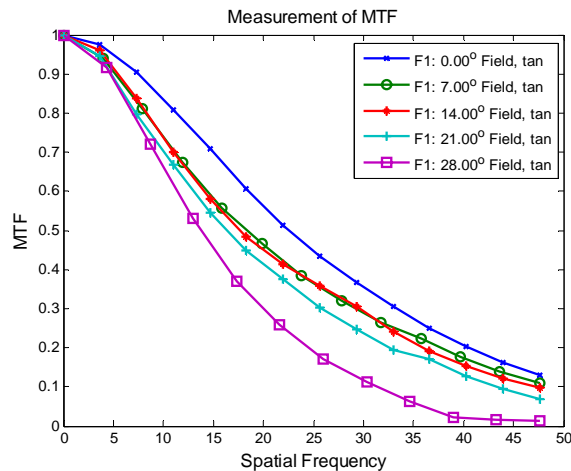


Figure 4.21 Measured MTF performance of the lens prototype for a set of tangential fields

4.5.2 Polarization measurement of the plastic lens

A plastics lens shows better performance than a glass lens in terms of lens weight and the feasibility of DOE fabrication, however, birefringence properties of a plastic element reduce the optical efficiency in a p-HMPD system. As shown in Figure 4.6 and Figure 3.1, the projection lens is located between two PBS's. The birefringence properties of the plastic elements may change the polarization states of the incident light, which leads to a lower optical efficiency. There are several explanations for the cause of birefringence properties of a plastic element, which can be categorized into: 1) orientational birefringence which is the intrinsic birefringence of the plastic material and (2) stress birefringence.

Polystyrene has much higher intrinsic birefringence than PMMA and CPC (Baumer, 2005). The intrinsic birefringence is orientational birefringence. One way to reduce the effect brought by the intrinsic birefringence of the projection lens is to align the fast axes of all plastic components with the polarization orientation of the incident light.

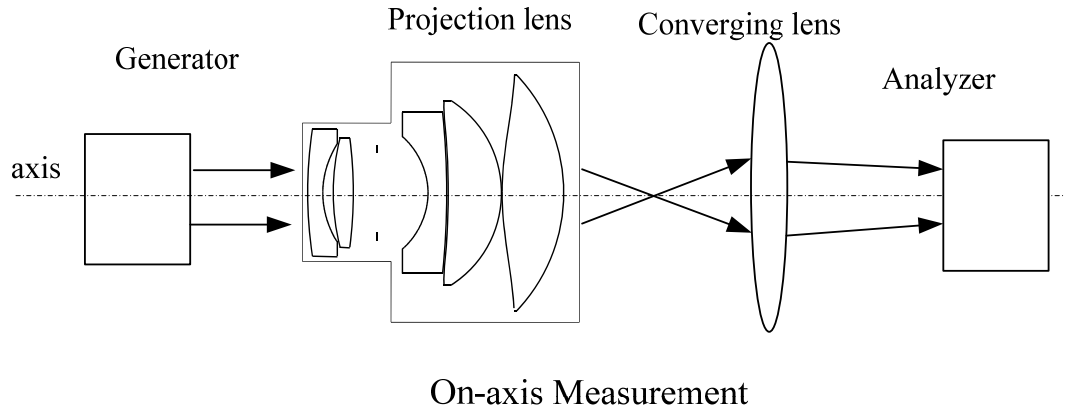
Stress birefringence is generally introduced in the molding process. The projection lens in the p-HMPD is fabricated using a diamond turning method, which generally will not introduce stress birefringence. However, in the assembly process, due to the tight tolerance, the pressure from lens rings on the plastic elements may cause stress birefringence.

Unfortunately I did not realize the potential problems caused by birefringence properties of the lens until I received the lens prototypes. At this stage, in order to reduce the light loss through a p-HMPD caused by the birefringence of the plastic lens, we further characterized polarization properties of the projections lens and explored methods

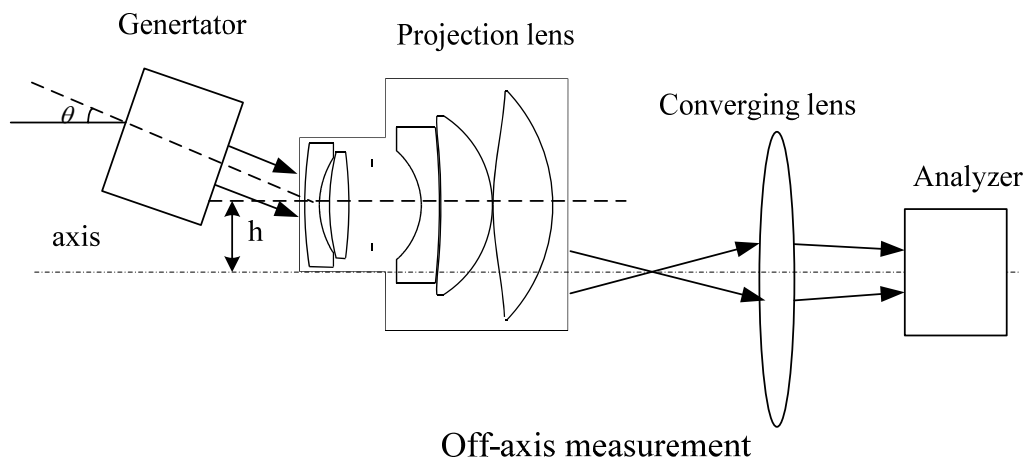
to improve the optical efficiency of a p-HMPD.

An Axometrics polarimeter was used for Mueller matrix measurements of the projection lens. An ideal way to do the measurement is to disassemble the lens set and measure the polarization performance of each component. However, due to the tight tolerance and high pressure on the plastics material from lens rings, disassembling the lens set may destroy the lens surface. Thus Mueller matrices of the projection lens were measured as a whole as a function of FOV.

Figures 4.22 (a) and (b) show the measurement setups for the on-axis field and off-axis fields, respectively. For the on-axis case, the beam from the generator was semi-collimated and the diameter of the beam was around 10mm so that the whole aperture of the projection lens could be filled. After passing through the projection lens, the beam was focused on the focal plane of the projection lens. A doublet lens with a focal length of 100mm and a diameter of 50mm was used as the converging lens to collect the output beam. In the test, the distance between the focal plane of the projection lens and the converging lens was larger than 100mm so that the output beam from the converging lens was slightly converged. Meanwhile, the distance between the Analyzer and the converging lens was long enough to make sure the beam size was smaller than the aperture of the analyzer. The converging lens was a coated glass lens and its normalized Mueller matrix measured by the polarimeter was close to a unity matrix. The depolarization index, the retardance magnitude and the diattenuation magnitude of the converging lens is smaller than 1%, 5° and 2% respectively. As a result, the polarization effect brought by the converging lens could be negligible.



(a)



(b)

Figure 4.22 Polarization measurement setup of the projection lens for (a) the on-axis field and (b) the off-axis field.

For the off-axis cases, four off-axis field angles, which are 7° , 14° , 21° and 27.5° , were measured. Since the polarization properties of the projection lens are not axially symmetrical, four measurements corresponding to four different rotational angles were performed at each off-axis field angle. As shown in Figure 4.22 (b), the generator was adjusted to an angle of θ , which is the measured field angle. Due to the nature of image space telecentricity of the projection lens, the projection lens was translated by a distance

of $h = f \cdot \tan(\theta)$ along the direction vertical to the axis while f is the focal length of the projection lens, so that the chief ray of the output beam was aligned with the optical axis. At each off-axis field angle, four measurements were performed by rotating the projection lens at four specified angles along its optical axis. The four specified angles were equally spaced within 360° . The same converging lens with a focal length of 100mm was used to converge the beam to the analyzer.

Two projection lenses were measured. Through the test, 17 Mueller Matrices were measured for each projection lens, including one measurement for the on-axis field and four measurements for each of four off-axis fields. Each Mueller matrix was normalized by its m_{00} component to compensate light loss in the measurement. Through the decomposition of the Mueller matrices at different field angles, the projection lens showed both retardance and depolarization properties. The goal of the polarization measurement was to mitigate the effects brought by the birefringence of the projection lens and to maximize the optical efficiency through a p-HMPD. Figure 4.23 shows a simplified drawing of the polarization propagation through the lens in a p-HMPD. The S-polarized light passes through the projection lens and then transmits through a horizontal polarizer which represents a PBS. Since the projection lens is allowed to rotate as a whole to a specified angle in the assembling process of a p-HMPD prototype, the optical efficiency of a p-HMPD can be optimized by selecting an optimal rotation angle α . The optical efficiency through the projection lens and the polarizer for horizontal polarized light can be calculated as a function of α using the equation

$$\begin{aligned}
P(\alpha) &= A(0^\circ) \cdot R(\alpha) \cdot MM_{lens}(0^\circ) \cdot R(-\alpha) \cdot S(0^\circ) & \alpha \in [0^\circ, 180^\circ] \\
&= \frac{1}{2} \begin{bmatrix} 1 \\ 1 \\ 0 \\ 0 \end{bmatrix}^T \cdot \begin{bmatrix} 1 & 0 & 0 & 0 \\ 0 & \cos(2\alpha) & -\sin(2\alpha) & 0 \\ 0 & \sin(2\alpha) & \cos(2\alpha) & 0 \\ 0 & 0 & 0 & 1 \end{bmatrix} \cdot MM_{lens} \cdot \begin{bmatrix} 1 & 0 & 0 & 0 \\ 0 & \cos(2\alpha) & \sin(2\alpha) & 0 \\ 0 & -\sin(2\alpha) & \cos(2\alpha) & 0 \\ 0 & 0 & 0 & 1 \end{bmatrix} \cdot \begin{bmatrix} 1 \\ 1 \\ 0 \\ 0 \end{bmatrix} \\
& & (4.6)
\end{aligned}$$

where $A(0^\circ)$ represents a horizontal polarized analyzer, MM_{lens} is the Mueller matrix of the projection lens, $R(\alpha)$ is the rotational matrix and $S(0^\circ)$ represents the horizontal polarized light. For each off-axis field angle, four data points were analyzed and the average optical efficiency of four data points was calculated to represent each off-axis field angle. Both projection lenses were measured and analyzed. Figures 4.24 (a) (b) and (c) show average optical efficiency of Lens I as a function of rotation angle α at five representative field angles for the wavelength of 450nm, 550nm and 650nm, respectively. The plots indicate that the maximum optical efficiency of Lens I can be reached for all three wavelengths when the rotational angle is at around 80° and the average optical efficiency across five field angles and wavelengths is as high as 85%. Thus, the light loss caused by the birefringence of Lens I can be significantly reduced by rotating the lens at 80° .

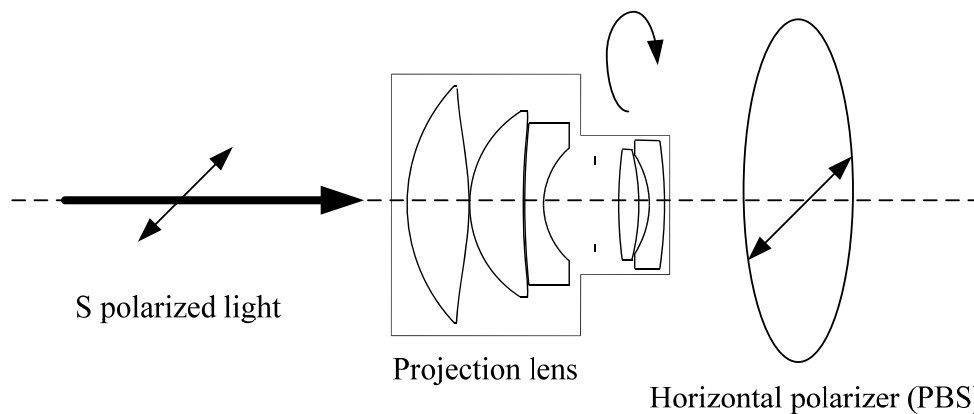


Figure 4.23 Simplified drawing of the propagation of the polarized light through the projection lens in a p-HMPD

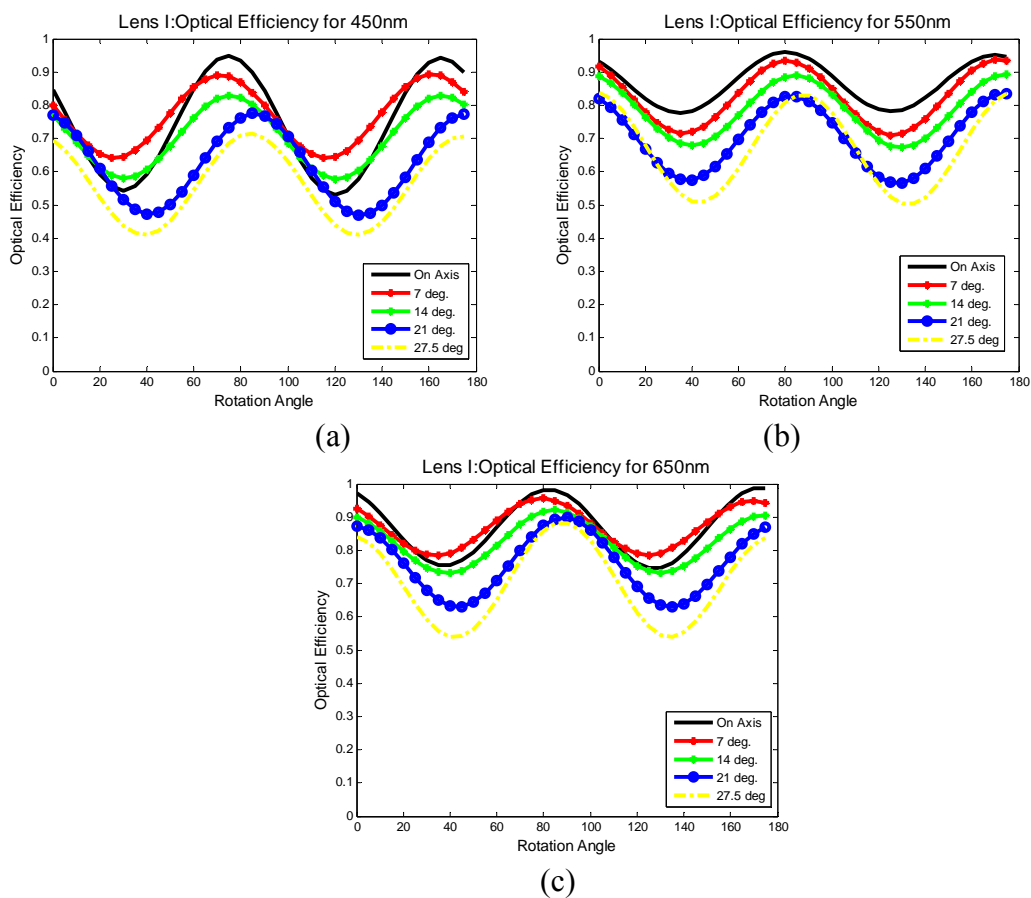


Figure 4.24 Average optical efficiency of Lens I as a function of rotation angle at five representative field angles for the wavelength of (a)450nm, (b)550nm and (c)650nm, respectively.

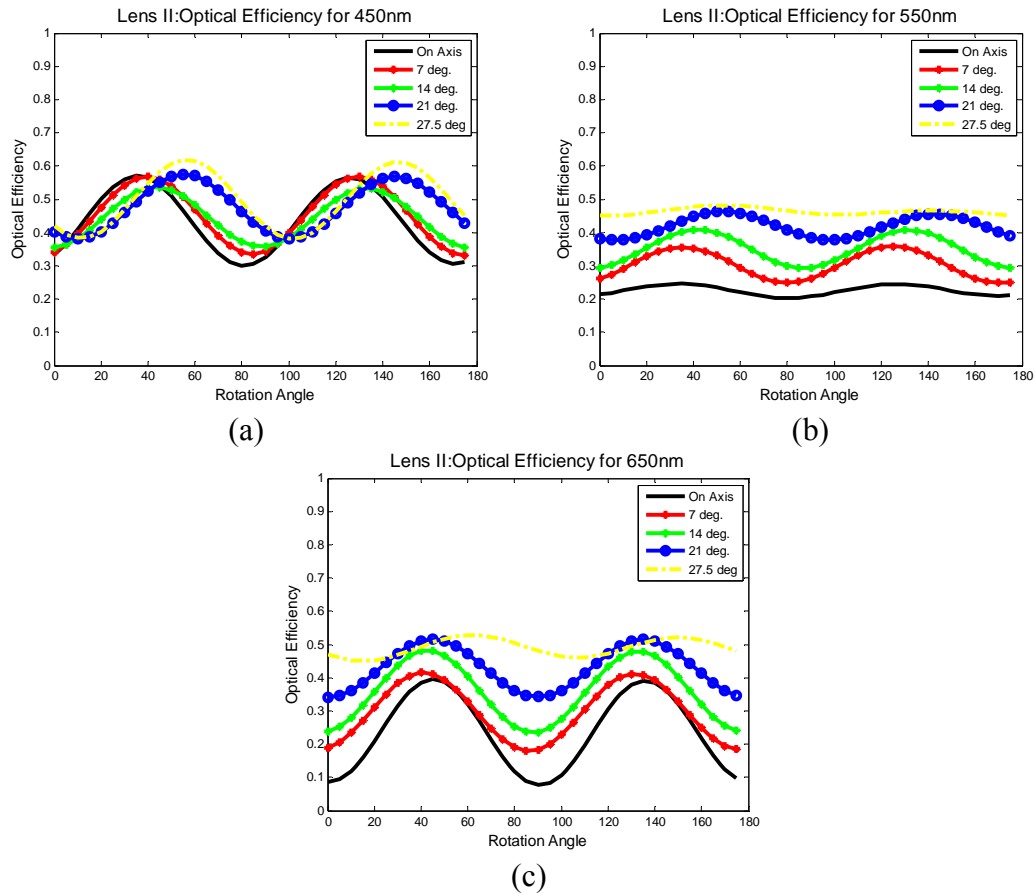


Figure 4.25 Average optical efficiency of Lens II as a function of rotation angle at five representative field angles for the wavelength of (a)450nm, (b)550nm and (c)650nm, respectively.

Figures 4.25 (a), (b) and (c) show the plots of the average optical efficiency of Lens II as a function of rotation angle at five representative field angles for the wavelength of 450nm, 550nm and 650nm, respectively. As shown in the plots, the optical efficiency does not improve a lot by just rotating the projection lens. To find other mitigation methods, we further studied the Mueller matrix of Lens II.

Taking the Mueller matrix at on-axis field with a wavelength of 550nm for example, The Mueller matrix of Lens II at on-axis field at 550nm is

$$MM_{550nm_OnAxis} = \begin{bmatrix} 1.0000 & \underline{-0.0064} & \underline{-0.0036} & \underline{-0.0066} \\ 0.0001 & \underline{-0.5779} & \underline{-0.6260} & \underline{0.1971} \\ 0.0019 & \underline{0.5762} & \underline{-0.5181} & \underline{0.1777} \\ -0.0105 & 0.0899 & 0.2201 & 0.7822 \end{bmatrix}. \quad (4.7)$$

The absolute value of components m_{11} , m_{22} , m_{12} and m_{21} are larger than 0.5, m_{11} and m_{12} have a negative sign while m_{21} and m_{22} have a positive sign. This structure makes it impossible to use the rotation matrices to improve the overall optical efficiency of a p-HMPD. To solve the problem, a polarization component needs to be added to manipulate the 2x2 matrix enclosed by the red line in Equation 4.7. Thus, a linear half-wave retarder was added between the projection lens and the horizontal polarizer to improve the optical efficiency of Lens II. Both the projection lens and the retarder have one degree of freedom to be rotated around the optical axis. The Mueller matrix of a horizontal retarder with its fast axis at angle θ is given by

$$HWR(\theta) = R(\theta) \cdot \begin{bmatrix} 1 & 0 & 0 & 0 \\ 0 & 1 & 0 & 0 \\ 0 & 0 & -1 & 0 \\ 0 & 0 & 0 & -1 \end{bmatrix} \cdot R(-\theta) \quad \theta \in [0^\circ, 180^\circ] \quad (4.8)$$

and the optical efficiency of the lens is given by

$$P(\alpha) = A(0^\circ) \cdot R(\alpha) \cdot (HWR(\theta) \cdot MM_{lens}) \cdot R(-\alpha) \cdot S(0^\circ) \quad \alpha \in [0^\circ, 180^\circ] \quad (4.9)$$

where $R(\theta)$ is the rotation matrix for a given rotation angle θ , and the other parameters have the same definition as Equation 4.6.

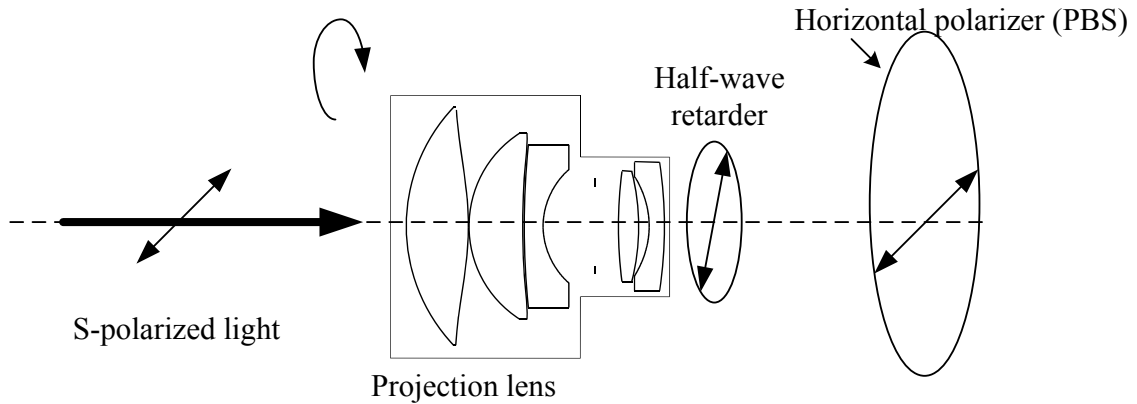


Figure 4.26 Simplified drawing of the propagation of the polarized light through the projection lens with an HWR.

By varying the angle θ and α , it was found that the optimal performance of Lens II could be obtained when $\theta=55^\circ$. Figure 4.27 shows the optical efficiency of Lens II as a function of rotational angle α at the wavelength of 450nm, 550nm and 650nm after an HWR with its fast axis at an angle of 55° was added. The optical efficiency of Lens II has been significantly improved after a retarder is added. The maximum optical efficiency of Lens II can be reached for all three wavelengths when the rotational angle α is at around 60° and the average optical efficiency the different field angles and wavelengths is about 75%. We further examined the Mueller matrix of Lens II at on-axis field at the wavelength of 550nm after mitigation. The Mueller matrix is given by

$$M_{550nm_OnAxis_miti} = \begin{bmatrix} 1.0000 & -0.0071 & 0.0019 & -0.0066 \\ 0.0000 & 0.8517 & -0.0336 & -0.1809 \\ 0.0019 & -0.0332 & -0.7738 & 0.1942 \\ 0.0105 & -0.2192 & -0.0921 & -0.7822 \end{bmatrix} \quad (4.10)$$

where the 2x2 matrix enclosed by the red line is close to a diagonal matrix.

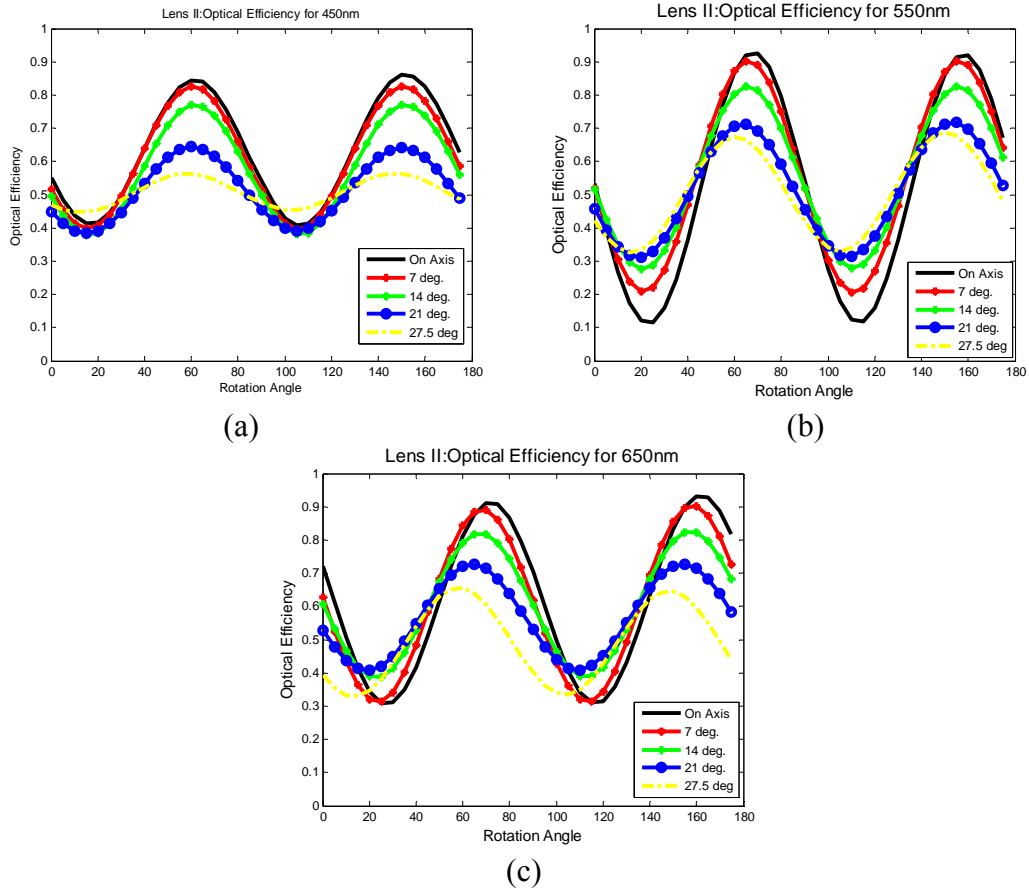


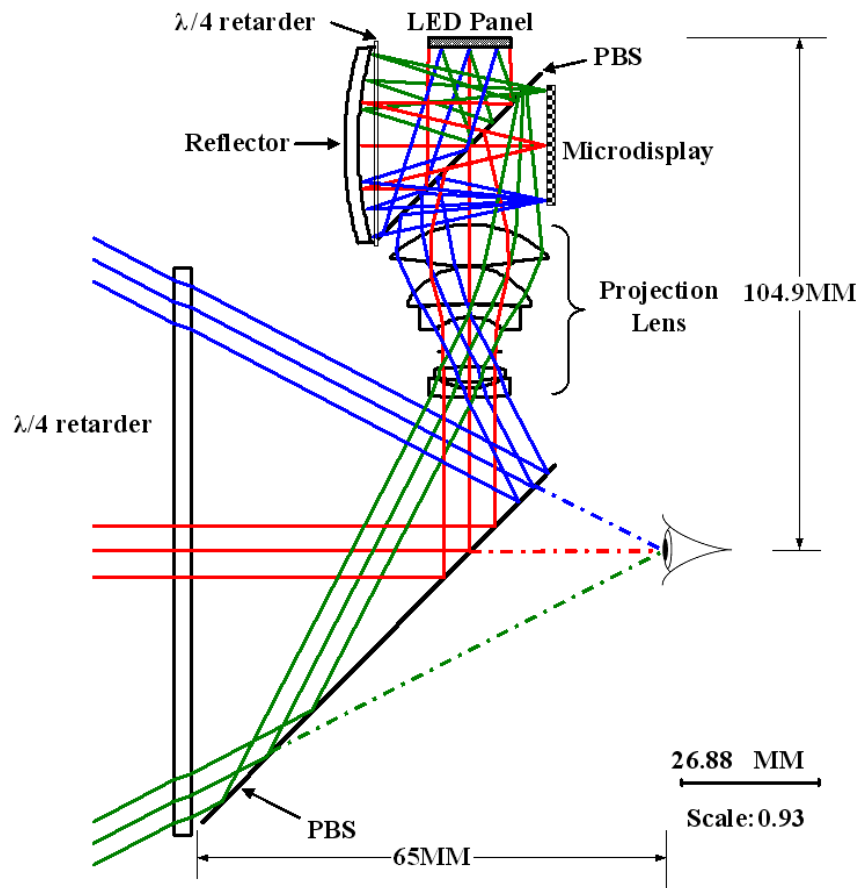
Figure 4.27 Optical efficiency of Lens II as a function of rotational angle α at the wavelength of (a)450nm, (b)550nm and (c)650nm after an HWR with its fast axis at 55° was added

4.6 A P-HMPD PROTOTYPE AND ITS PERFORMANCE

Based on the design of the light engine and the projection lens, a p-HMPD prototype was further developed. Considering both ergonomic and aesthetic factors, we mounted the optics vertically to ensure that the width of the helmet was around the average width of an adult head. Figure 4.28 (a) shows the overall optical layout of the system. In the vertical direction, the optics is mounted according to the shape factor of the head and the associated electronics is mounted on the top of the helmet. A major drawback of the

vertical mount is that the ghost view directly reflected from the ground by the PBS is overlaid with the projected image, which leads to reduced image contrast. This problem, however, can be solved by blocking the optical path from the ground.

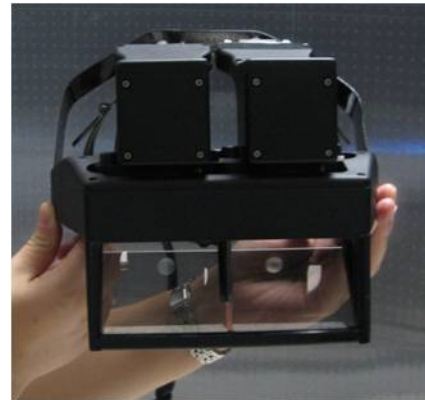
To make the system more compact and lighter, the mount of the light engine and projection lens was fabricated separately and then integrated with the shell as a whole. By adjusting the mount of the light engine and projection lens, the IPD of the p-HMPD can be changed. The lens position relative to the microdisplay is adjustable to obtain a projected image with adjustable magnification. The helmet shells were fabricated using rapid prototyping techniques, in which physical models were fabricated layer by layer directly from 3D CAD models. The helmet shells were assembled and attached to an off-the-shelf headband that offers head-size adjustment. The front and side views of the prototype are shown in Figure 4.28 (b) and (c), respectively.



(a)



(b)



(c)

Figure 4.28 Design of a compact p-HMHD prototype: (a) Overall optical layout of the system; (b)-(c) side and front views of the p-HMHD prototype.

We further measured the exit pupil diameter of the p-HMPD prototype. A diffuser was placed at the pupil plane of the p-HMPD and Figures 4.29 (a) and (b) show the photos of the pupil. Figure 4.29(a) was taken at a dark environment with longer exposure time while Figure 4.29(b) was taken at a brighter environment with shorter exposure time. The black circle labeled in the picture has a diameter of 12mm. By comparison of two figures, the diameter of the pupil can be estimated to be around 10~12mm although the luminance drops at the edge of the circle.

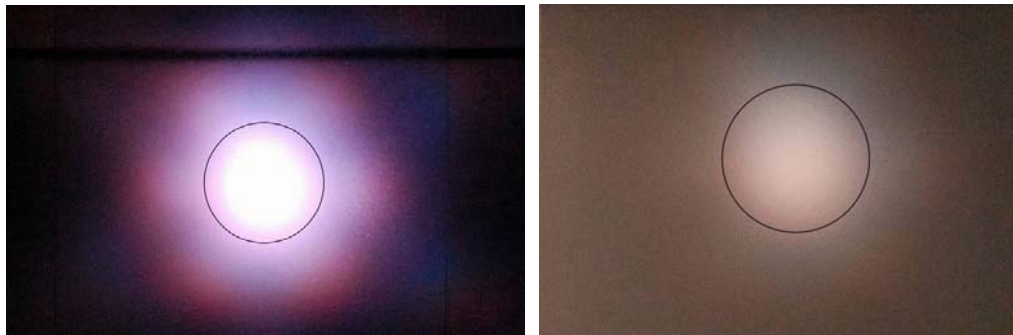


Figure 4.29 Photos of the pupil through a p-HMPD prototype type: (a) is taken in a darker environment with longer exposure time and (b) was taken at a brighter environment with shorter exposure time.

We further estimate the luminance level of the p-HMPD prototype. Based on the measurement results done by Forth Dimension (www.forthdd.com), the maximum on-axis luminance level of the LED panel, driven by an FLCoS microdisplay, is 7650fL. Since the light transmittance of the illumination unit is 12.7%, the maximum luminance from the FLCoS microdisplay is estimated to be 971.6fL. Based on the measurement of the projection lens through a polarimeter, the light loss due to the absorption of the plastic material is about 20% and the light loss due to birefringence effects is about 20%. Thus the transmittance through a projection lens is estimated to be 64%. Based on the

polarization measurement results in chapter 3, the optical efficiency of a p-HMPD for the parts located behind the projection lens is around 12%. Thus, the final image luminance is estimated to be as high as 75fL or 256cd/m², which is 63 times brighter than the older prototypes. Under this luminance level, the p-HMPD prototype can be used in a well-lit indoor environment.

4.7 SUMMARY

In Chapter 4, we have designed a p-HMPD system using FLCoS microdisplays. The design of the key elements of the system, including a light engine and a projection lens, were presented. The performances of both designs are analyzed in details. Compared with older prototypes using transmissive LCDs, both luminance and image resolution of the new system have been improved significantly.

CHAPTER 5

CALIBRATION OF A P-HMPD

Based on a p-HMPD prototype, a series of calibrations were performed to obtain correct color presentation, desired focusing setting and accurate depth rendering necessary for achieving accurate registration between virtual objects and their counterparts in the real world. In this chapter, these calibration methods are reviewed.

5.1 COLOR CALIBRATION

5.1.1 Mathematical model

The color characteristics of a p-HMPD system are determined by the spectral properties of the LED illuminator, the optical properties of the microdisplays, and the luminous transfer properties through the p-HMPD system. As mentioned in Chapter 3.5, the luminance transfer efficiencies of a p-HMPD have considerable dependence on wavelengths, which could lead to chromaticity shift and reduced fidelity in color representation. In order to evaluate the chromatic characteristics of the system and to obtain accurate color representation, we developed color calibration programs and performed color calibration on our system using the method summarized by Sharma (Sharma, 2002). The calibration was performed on both the left and right eye displays, which helps to eliminate potential color inconsistencies between two displays and ease the difficulty of image fusion caused by color discrepancies.

The FLCOS microdisplay is driven by the signals controlled by the R, G, B triplet for each pixel, corresponding to the red, green and blue channels for that pixel. Typically the red, green and blue channels function independently and the coupling between neighboring pixel elements can be ignored. Assuming the display is spatially homogeneous, the colorimetric performance of the p-HMPD system can be specified by a CIE XYZ tristimulus vector $\mathbf{t}(R, G, B) = [t_1, t_2, t_3]^T$, where t_1 , t_2 , and t_3 are the CIE X, Y, and Z tristimulus values, respectively. With the channel-independence assumption, the tristimulus values of the p-HMPD can be written as

$$\mathbf{t}(R, G, B) = \mathbf{t}_r(R) + \mathbf{t}_g(G) + \mathbf{t}_b(B) + \mathbf{t}_0 \quad (5.1)$$

where $\mathbf{t}_r(R)$ represents the XYZ tristimulus vector produced by the spectral emission from the red channel in response to the input value R and, in the similar way, $\mathbf{t}_g(G)$ and $\mathbf{t}_b(B)$ represent the XYZ tristimulus vectors by the light emitted from the green and blue channels, respectively, and \mathbf{t}_0 accounts for the light emitted from a dark pixel with $R=G=B=0$.

With a further assumption that the spectrum of the light from a channel has the same basic shape and only undergoes a scaling in amplitude as the driving signal of that channel is varied, the tristimulus vectors for the light from the red, green, and blue channels, respectively, can be written as

$$\begin{aligned} \mathbf{t}_r(R) &= v_r(R)\mathbf{t}_{mr} \\ \mathbf{t}_g(G) &= v_g(G)\mathbf{t}_{mg} \\ \mathbf{t}_b(B) &= v_b(B)\mathbf{t}_{mb} \end{aligned} \quad (5.2)$$

where $v_r(R)$, $v_g(G)$, and $v_b(B)$ denote the amplitude scaling factors, also referred to as the

tone-response curves (TRCs), for the three channels, respectively, \mathbf{t}_{mr} , \mathbf{t}_{mg} , and \mathbf{t}_{mb} represent the tristimulus values at the maximum driving signal for the red, green, and blue channels, respectively. Equations 5.1 and 5.2 can be combined and rewritten as

$$\begin{aligned}\mathbf{t}(R,G,B) &= \mathbf{t}_r(R) + \mathbf{t}_g(G) + \mathbf{t}_b(B) + \mathbf{t}_0 \\ &= [\mathbf{t}_{mr}, \mathbf{t}_{mg}, \mathbf{t}_{mb}] \cdot [v_r(R), v_g(G), v_b(B)]^T + \mathbf{t}_0 \\ &= \mathbf{T}_m \cdot [v_r(R), v_g(G), v_b(B)]^T + \mathbf{t}_0\end{aligned}\quad (5.3)$$

where $\mathbf{T}_m = [\mathbf{t}_{mr}, \mathbf{t}_{mg}, \mathbf{t}_{mb}]$ characterizes the intrinsic chromaticity of each channel of the display device and defines the color gamut in the XYZ color diagram.

Color calibration of a display typically takes two steps. The first step is a colorimetric characterization step to obtain the TRCs and the intrinsic chromaticity matrix. The second step is to obtain the inverse of the device characterization model in Equation 5.3 and to obtain the RGB grayscale values corresponding to any desired tristimulus values. Based on the assumptions that (1) the TRCs are invertible functions and (2) the matrix \mathbf{T}_m is nonsingular, the inverse model to obtain the RGB driving values corresponding to a desired XYZ tristimulus vector \mathbf{t} is written as:

$$[R, G, B] = [v_r^{-1}(R'), v_g^{-1}(G'), v_b^{-1}(B')] \quad (5.4)$$

where

$$[R', G', B'] = [v_r(R), v_g(G), v_b(B)] = \mathbf{T}_m^{-1} \cdot (\mathbf{t} - \mathbf{t}_0) \quad (5.5)$$

5.1.2 Colorimetric characterization

In order to characterize the colorimetric performance of a p-HMPD prototype, a series of spatially uniform color patches were displayed through the p-HMPD. The

p-HMPD helmet was mounted on an optical bench and the fiber detector of a spectrometer by Ocean Optics was placed at the exit pupil of the p-HMPD system to measure the spectral radiance for each of the color patches. The spectrometer has a sampling resolution of 0.35nm in the range of 380nm to 980nm. The XYZ tristimulus values of the displayed color patch can then be computed using the CIE 2° color-matching functions (CIE, 1986). All the measurements were made in a dark environment to minimize stray light. Since chromaticity shifts of a p-HMPD system demonstrate relatively low dependence on the field angles, all the measurements were measured only for the central FOV within about 2° confined by the FOV of the spectrometer detector.

In the FLCoS microdisplays, the LED illuminator is driven by a color sequential technique and the maximum brightness of the LEDs for each color channel can be controlled through a software interface that controls the driver board of the microdisplay through an RS232 port. The command levels controlling the brightness of the three LEDs are not independent from each other. Instead, decreasing the brightness of one LED can result in an increase of the brightness of the other two LEDs, which can consequently change the color spectrum of the source. Therefore, the color calibration of the p-HMPD system is slightly different from the typical two-step procedure mentioned in Sec. 5.1.1. Before the colorimetric characterization step is performed, the LED illuminator needs to be calibrated to obtain a desired white point for the display. In this process, we displayed a white pattern with R=G=B=255 on the microdisplay and measured the spectral radiant distribution output through the p-HMPD system. We then computed the corresponding

CIE XYZ tristimulus values and chromaticity coordinates. Through the software interface of the microdisplays, we gradually adjusted the command levels of the three LEDs and repeated the tristimulus value measurement until the chromaticity coordinates of the white point is calibrated to be around (0.333, 0.333). This step was repeated for both the left and right eye displays.

Following the source calibration, colorimetric characterization step was performed to obtain the intrinsic color gamut and the TRCs of the display. The characterization color patches consisted of ramps with 33 levels for each of the R, G, B channels. For example, the characterization patches for the red channel consists of patches with $G=B=0$ and R values uniformly sampling the range from 0 to $R_{\max}=255$. The black spectrum measured at $R=G=B=0$ suggests that a small fraction of the LED source light is reflected by the pixels even in the OFF state. To remove this residual effect, the individual RGB channel spectral measurements for the R, G, and B ramps are offset-corrected by subtracting the black spectrum.

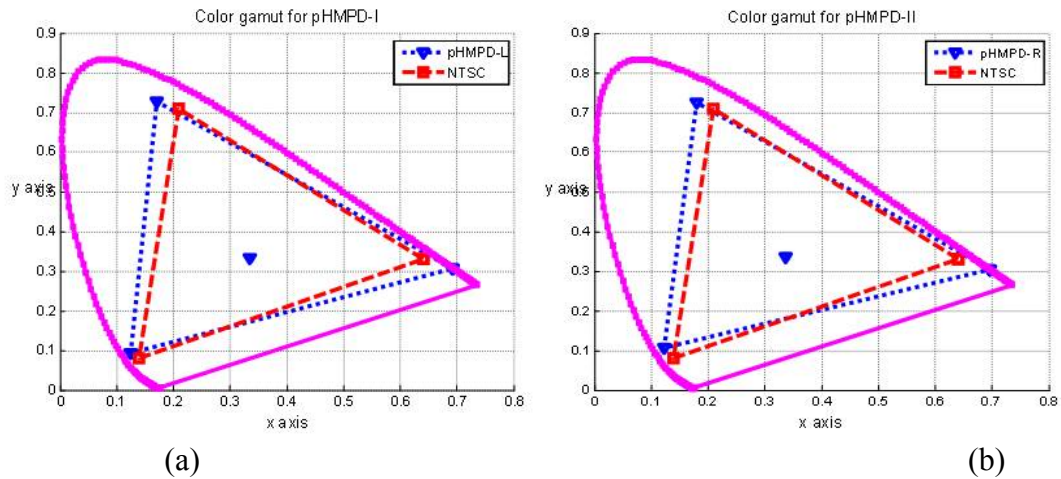


Figure 5.1 Color gamuts for (a) the left-eye display and (b) the right-eye display.

The intrinsic color gamut of the display is obtained by the spectral measurements at the maximum driving signal for each of the color channels (i.e. R=255, or G=255, or B=255). The intrinsic chromaticity matrices for both the left- and right-eye displays are:

$$\mathbf{T}_{m-L} = \begin{bmatrix} 18342.31 & 3334.72 & 3684.13 \\ 8123.76 & 14203.12 & 2806.45 \\ 28.86 & 1968.55 & 23326.36 \end{bmatrix} \quad (5.6)$$

$$\mathbf{T}_{m-R} = \begin{bmatrix} 19158.4 & 3694.24 & 3902.15 \\ 8356.59 & 14982.68 & 3428.40 \\ 24.54 & 1960.14 & 24587.55 \end{bmatrix}$$

In Figure 5.1(a) and (b), the triangles formed by the blue dash line show the achievable color gamut of the left- and right-eye displays, respectively, in the CIE x-y chromaticity space. For the left-eye display, the chromaticity coordinates for the red, green, blue and white are (0.692, 0.307), (0.171 0.728), (0.124 0.094) and (0.335 0.333), respectively, while the coordinates for the right-eye display are (0.696 0.303), (0.179 0.726), (0.122 0.107) and (0.337 0.335), respectively. The color gamut of the two displays is fairly close. Compared to the triangle formed by the red dash line which represents the color gamut of the NTSC standard, the p-HMPD has a slightly larger color gamut.

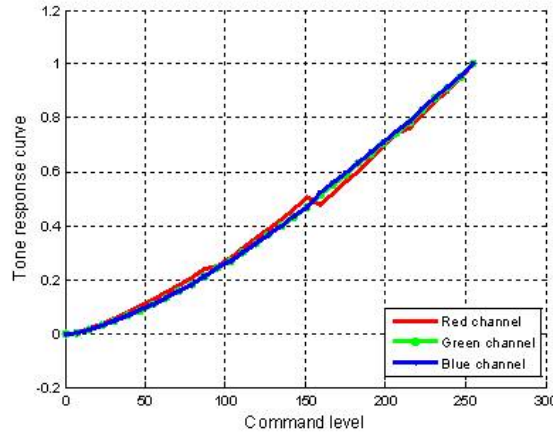


Figure 5.2 Tone response curves for R, G, B channels

The TRCs of the red, green, and blue channels can also be computed from the spectral measurements for the individual channel ramps. Since both the left and right displays are driven in a similar manner, in the following discussion, we only present the results for the left-eye display since both displays have the similar performance. The TRCs for R, G, B channels of the left-eye display are shown in Figure 5.2. Overall, the TRCs for the three color channels have similar shapes. The TRC for the red channel demonstrates an abnormal drop around the command level of 155, which is caused by the defect of the driving sequence file. The TRCs for each channel can be fit by a power-law function

$$v(CL) = \left(\frac{CL}{255}\right)^\gamma \quad (5.7)$$

where CL represents the command level of the channel and γ is commonly referred as the gamma value of the display.

Through the best-fit algorithm, the gamma values for the red, green, blue channels are calculated to be 1.431, 1.403, and 1.420, respectively. The mathematical model for

the TRCs of R, G, B channels can be written as:

$$\begin{aligned} v_r(R) &= \left(\frac{R}{255}\right)^{1.431} \\ v_g(G) &= \left(\frac{G}{255}\right)^{1.403} \\ v_b(B) &= \left(\frac{B}{255}\right)^{1.420} \end{aligned} \quad (5.8)$$

5.1.3 Model evaluation

With the assumptions of channel independence and channel-chromaticity constancy, the per-channel spectral characterizations obtained in the previous subsections can be used to predict the spectral radiance as well as the corresponding CIE x-y chromaticity coordinates for the display with any combinations of RGB triplet. Furthermore, the inverse model of the p-HMPD system can also be obtained using the Equation 5.4 and 5.5, which can be used to obtain the RGB driving values corresponding to a desired XYZ tristimulus vector \mathbf{t} . Given the power-law form for the TRCs, the Equation 5.4 can be written as

$$[R, G, B] = [(R')^{\frac{1}{\gamma_r}} \times 255, (G')^{\frac{1}{\gamma_g}} \times 255, (B')^{\frac{1}{\gamma_b}} \times 255] \quad (5.9)$$

where $[R', G', B']$ was obtained with Eq. (5.5) using the \mathbf{T}_m matrix.

Table 5.1 Color calibration errors for left-eye display over 3x3x3 test patches

	RMS Error	Mean Error	Max Error
ΔE_{ab}^* units	4.70	3.26	11.18
ΔE_{94}^* units	1.87	1.39	3.67

To evaluate the calibration error, we tested with 27 independent color patches that are 3x3x3 ramps uniformly sampling the RGB color cube. The actual spectrum of each

test pattern was measured, while the predictions of these patches were also made using TRCs combined with the spectra measured at the maximum driving signals of each channel. The measured spectra and predicted spectra of these test patterns were converted into CIELAB values through which the color errors can be calculated in terms of ΔE^*_{ab} (CIE, 1986) and ΔE^*_{94} units (CIE, 1995). The root mean square (RMS), the average and the maximum color error are listed in Table 5.1. This level of error is acceptable for the p-HMPD application.

5.2 CALIBRATION OF THE FOCUSING PLANE

In order to minimize viewing discomfort and to ease stereo fusion caused by the accommodation-convergence depth discrepancy, the focusing plane of the p-HMDP is adjustable to meet the requirement of different applications. For example, for the workbench applications, the focusing distance is set to be 1m, while for the walk-through applications, the focusing distance is preferably set to be 2m.

For a digital projector, the image is projected on a diffusing screen and the best image quality is obtained when the image plane overlaps with the diffusing screen. In a p-HMPD system, although the best image resolution is expected when the projected image plane coincides with the retroreflective screen, the image resolution changes much less significantly with the position of a retroreflective screen comparing with a digital projector. Thus, the screen position can be hardly used as a reference plane to calibrate the focusing plane.

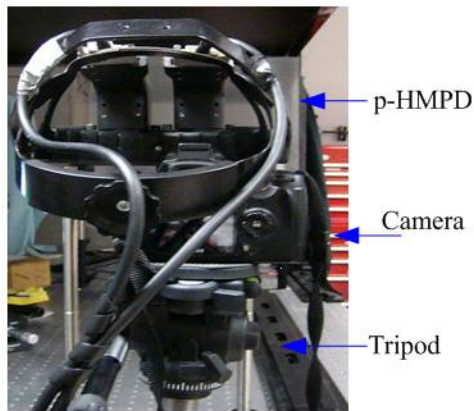
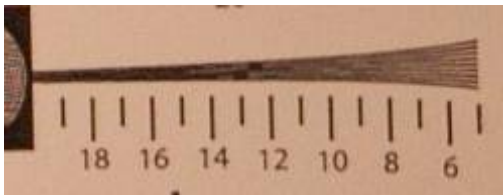


Figure 5.3 Nikon D40 on a Tripod was used to capture the image through a p-HMPD

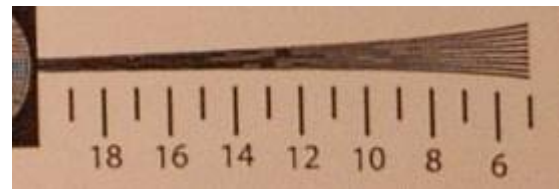
In the calibration, as shown in Figure 5.3, a Nikon D40 digital camera was used to measure the focusing distance. In the measurement, the p-HMPD helmet was mounted on the optical bench by two optical posts. The camera was fixed on a tripod and was adjusted to match its pupil with that of the p-HMPD. First, an image of the p-HMPD is captured through the camera. The capture mode of the camera was set to be automatic so that the camera automatically focused on the image plane of the p-HMPD to capture the image. The next step is to calculate the focusing distance of the camera. With the camera still at the same position, the p-HMPD helmet was moved away. Instead, an ISO 12233 chart was placed in front of the camera. The focusing mode of the camera was then switched to the manual mode and multiple pictures were taken while the chart was moved from a far distance to a closer distance relative to the camera. The picture with the best image quality can be selected and the corresponding position was taken as the focusing plane. Since the depth of focus of the camera is about 1cm, the movement step size of the chart is 2cm. In our case, multiple pictures were taken when the chart was moved from 120cm to 80cm in a step size of 2cm. Figure 5.4 shows the pictures of a part of ISO

12233 chart when the chart was 102 cm, 100cm, 98cm and 96cm away from the camera, respectively. By examining the cut-off frequency of each image, the pictures at the 100cm and 98cm have the highest cut-off frequency. As a result, the focusing distance for this case is estimated to be 99cm.

To set the focal plane of the p-HMPD at a desired distance, a reverse process can be followed. First, the ISO 12233 chart was placed at the target position which coincides with the desired focusing plane. By taking a picture of the chart, the camera in the automatic mode would focus on the chart. Second, a p-HMPD was placed in front of the camera to match its pupil with the pupil of the camera. A square wave pattern in the threshold frequency of the microdisplay was displayed through the p-HMPD. The focusing distance of the p-HMPD optics was adjusted in a small step size consecutively and the images through the p-HMPD at each focusing distance were captured by the camera in the manual mode. The focusing plane corresponding to the best image resolution is the target plane. Since it is less accurate to decide the focusing plane by comparing the image blur of square wave patterns, this method only provides a good way to roughly adjust the focusing plane to a desired position. We still need to measure the adjusted focusing distance using the method described above to obtain a more accurate value of the focusing distance.



(a)



(b)

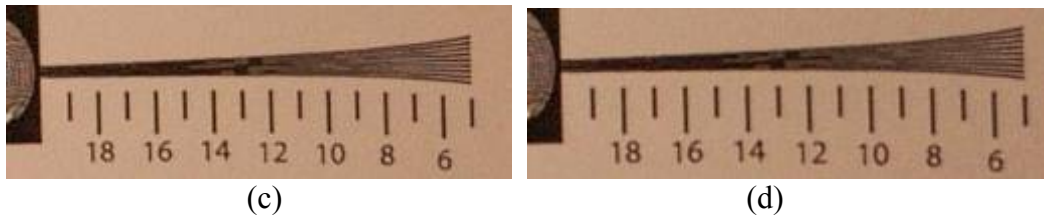


Figure 5.4. Pictures of a part of ISO 12233 chart when the chart was (a) 102cm, (b)100cm, (c) 98cm and (d) 96cm away from the camera

5.3 GEOMETRICAL CALIBRATION

In AR applications, 3D virtual images are superimposed with the real world and users are allowed to explore both the virtual world and the real world simultaneously. In order to achieve accurate registration between virtual objects and their counterparts in the real world, a geometrical calibration was performed on the p-HMPD using an off-line calibration method proposed by Gao *et al.* (Gao *et al.* 2003). In this section, the calibration method and procedure are briefly overviewed.

As introduced in Chapter 2, a SCAPE system was developed in 3DVIS lab. To register a virtual object with its counterpart in the real world and in real time, a 6DOF (degree of freedom) HiBall 3000 optical tracking system from the 3rdTech Inc (www.3rdtech.com) was utilized to detect the head motion of each user. The HiBall 3000 tracking system was composed of two key elements: a HiBall Optical Sensor and HiBall Ceiling Arrays. The HiBall Optical Sensor, composed of 6 lenses and photodiodes, was mounted on the p-HMPD helmet. The HiBall ceiling arrays, composed of IR LED arrays, were mounted on the ceiling of the SCAPE. By capturing the image of the IR LED arrays through the HiBall sensor, the HiBall position and orientation could be defined. Figure

5.5 (a) shows a view of the helmet with a HiBall 3000 sensor attached. Figure 5.5(b) shows the SCAPE environment where the HiBall 3000 tracker is installed on the ceiling.

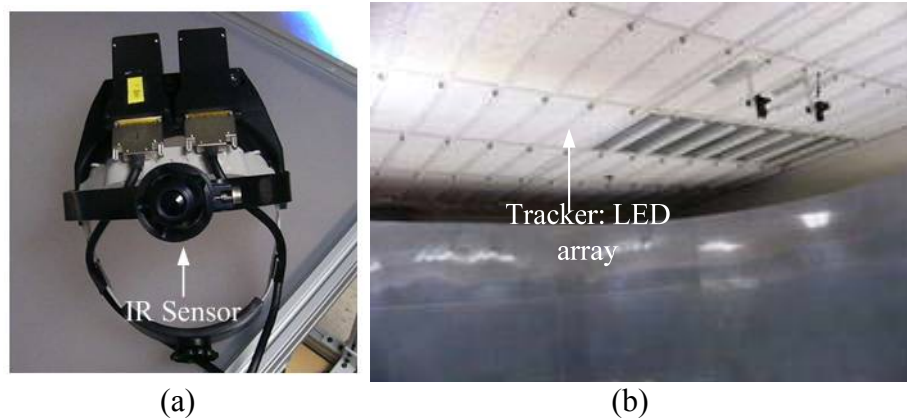


Figure 5.5 (a) HiBall IR sensor and (b) HiBall tracker

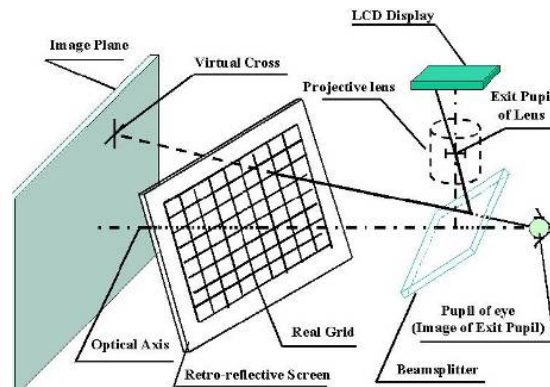


Figure 5.6 Simplified view of the image formation in a p-HMPD (Hua, *et al.* 2007)

The goal of the calibration is to find the projected point on the microdisplay for a 3D image point in real time. Similar to a typical HMPD system, image forming through a p-HMPD is a two-step process as shown in Figure 5.6: the projected image is projected through the projection lens and the eye views the image through the pupil of the p-HMPD (Hua, *et al.* 2007). As shown in Figure 5.7, the image forming process is modeled using an object plane, an image plane and a projection center which coincides with the pupil

general form is given by

$$\mathbf{T}_{i \leftarrow j} = \begin{bmatrix} \mathbf{R} & \vec{\mathbf{v}} \\ 0 & 1 \end{bmatrix} \quad (5.10)$$

where \mathbf{R} is a 3 x 3 rotation matrix and $\vec{\mathbf{v}}$ is a 3x1 the translation vector between two coordinates. To obtain the transformation matrix of the EVP in the sensor coordinate, a calibrated camera was used. The pupil of the camera matched the exit pupil of the p-HMPD. Thus, the EVP coordinate had the same origin with the camera coordinate but might have different orientations. The matrix \mathbf{R}_E was defined as the rotation matrix from the camera coordinate to the EVP coordinate. To obtain the matrix \mathbf{R}_E , a 10 x 8 black-white checkerboard pattern was displayed through the p-HMPD and the size of each unit pattern was 128x128 pixels. Figure 5.8(a) shows the image of the checker board captured by the calibration camera. Through the checker board image from the p-HMPD, all the parameters of the EVP coordinate, including rotation matrix \mathbf{R}_E , the focal length f of the projection lens and the central offset (u, v) can be calculated using the calibration toolbox (www.vision.caltech.edu/bouguetj/calib_doc/). Based on the rotation matrix \mathbf{R}_E , the transformation matrix between EVP and the camera coordinate is given by

$$\mathbf{T}_{camera \leftarrow EVP} = \begin{bmatrix} \mathbf{R}_E & 0 \\ 0 & 1 \end{bmatrix} \quad (5.11)$$

Meanwhile, the transformation matrix from the camera coordinate to the tracker coordinate was calculated. A physical checker board was placed in front of the camera. A stylus, which was mounted on another HiBall sensor, was used to record the coordinates of the four corners of the checkerboard in the tracker coordinate. Through the recorded coordinates, a transformation matrix from the checkerboard to the tracker coordinate

$\mathbf{T}_{World \leftarrow Board}$ was obtained. A picture of the checkerboard was captured by the camera as shown in Figure 5.8(b). By using the calibration toolbox, the transformation matrix between the camera coordinate and the checkerboard coordinate, $\mathbf{T}_{Board \leftarrow Camera}$, can be obtained. By simply recording the orientation and the position of the HiBall sensor mounted on the p-HMPD, the transformation matrix from the real world to the sensor, $\mathbf{T}_{Sensor \leftarrow World}$, can be obtained. Finally, the transformation from the EVP to the sensor coordinate is given by

$$\mathbf{T}_{Sensor \leftarrow EVP} = \mathbf{T}_{Sensor \leftarrow World} \mathbf{T}_{World \leftarrow Board} \mathbf{T}_{Board \leftarrow Camera} \mathbf{T}_{Camera \leftarrow EVP} \quad (5.12)$$

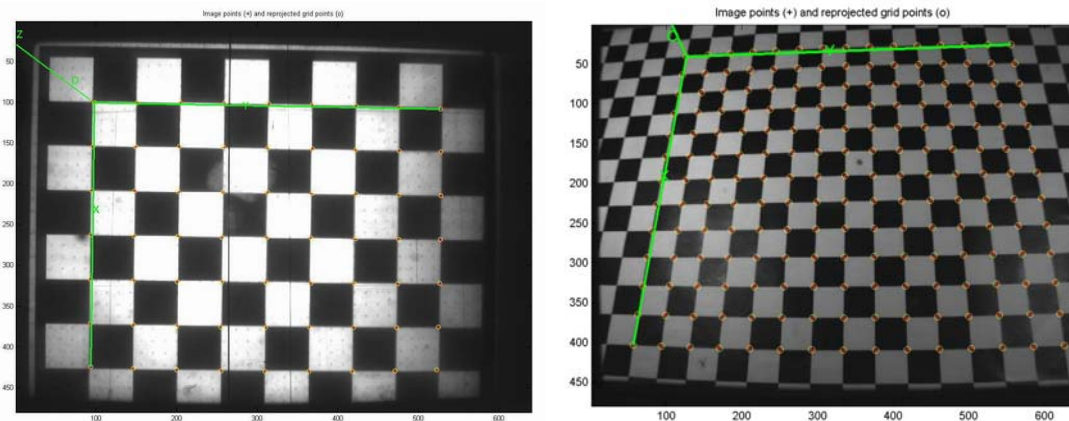


Figure 5.8 (a) Image of the checkerboard from the p-HMPD (b) Image of a Real checkerboard captured by a video camera.

Based on the review above, the calibration procedure can be summarized in the following steps:

- 1). Calibrate two video cameras using the Matlab Toolbox program and obtain the intrinsic parameters of the camera, such as focal length and distortion parameters.
- 2). Mount the p-HMPD prototype on an optical bench. Mount the two video cameras on

the optical rail and adjust the cameras to match the pupils of two cameras with the left eye pupil and the right eye pupil of the p-HMPD. The experiment setup is shown in Figure 5.9.

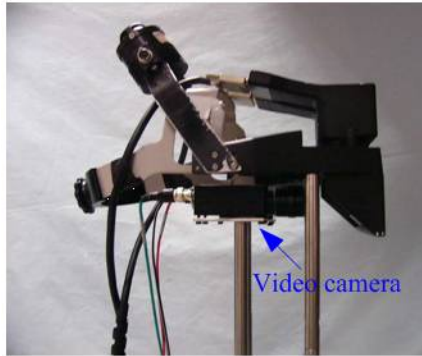


Figure 5.9 Experiment setup to capture pictures through p-HMPD

3) Display a checkerboard image on the microdisplays of the p-HMPD. Place a retroreflective screen in front of the p-HMPD helmet. Capture the images from the microdisplays using video cameras. Through the checkerboard images, \mathbf{R}_E , focal length of the projection lens and the offset (u, v) for both eyes can be obtained.

4) Place a physical checkerboard in front of the helmet and make sure the board fills the FOV of the video cameras and take a picture of the checker board. The matrix $\mathbf{T}_{Board \leftarrow Camera}$ can be obtained.

5) Use a stylus mounted with a sensor to record the coordinates of four corner of the checkerboard. The matrix $\mathbf{T}_{World \leftarrow Board}$ can be obtained using the Calibration Toolbox.

6) Record the orientation and the position of the sensor on the p-HMPD helmet to obtain $\mathbf{T}_{World \leftarrow Sensor}$.

Following the six steps above, the transformation matrix between the sensor and the

EVP for both eyes, the focal length and the display offset (u, v) for both eyes can be obtained. For a moving p-HMPD user, the coordinate and the orientation of the p-HMPD sensor in the real world are updated in real time through the tracking system. Thus, the transformation from the EVP to the real world is updated in real time, through which the projected image point on the microdisplays can be calculated for any target virtual point within the FOV.

5.4 SUMMARY

In chapter 5, the calibration methods for color calibration, focusing plane calibration and geometrical calibration are reviewed.

CHAPTER 6

IMAGING PROPERTIES OF A RETROREFLECTIVE SCREEN

Chapter 6 is partially based on a published article entitled “Imaging quality of a retroreflective screen in head mounted projection displays” (Zhang & Hua, 2009).

A retroreflective screen is one of the key elements in an HMPD system and its imaging properties play critical roles in the overall imaging performance of an HMPD system. In this chapter, the imaging properties of a retroreflective screen are analytically studied based on a geometrical model and a diffractive model. Using a numerical analysis method, we further evaluate the image resolution of a retroreflective screen in an HMPD system. It is worth noting that the results of this study are not unique to an HMPD system but applicable to all HMPD-like systems and perhaps other imaging systems involving a retroreflective screen.

6.1 INTRODUCTION

Different from diffusing and specular surfaces, a retroreflective screen redirects incident light along its opposite incident directions as shown in Figure 6.1(c).

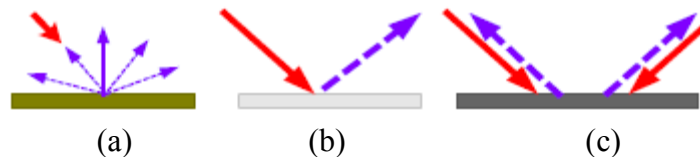


Figure 6.1 three types of reflection (a) Diffusing surface, (b) Specular surface (c) Retroreflective surface (Hua *et al.* 2002)

A micro corner cube reflector (CCR) array is one of commercially available

retroreflective screens. A micro corner cube reflector, composed of three reflective faces, can have either a solid structure or a hollow structure. The three reflective faces of a micro CCR are perpendicular to each other. The light entering a micro CCR is retroreflected through either three consecutive total internal reflections, typically in a solid structure, or three reflections, typically in a hollow one. Figure 6.2 demonstrates the microscopic structure of a retroreflective screen based on the CCR array technology. The screen is composed of hollow micro CCRs and aluminum coating is applied to each surface of a CCR element. The length of each side of the triangular aperture is about $200\mu\text{m}$.

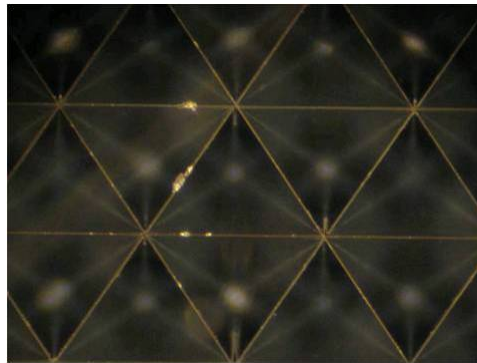


Figure 6.2 Photo of a micro CCR based retroreflective screen

6.2 RELATED WORK

Corner cube reflectors have a wide range of applications for non-image-forming systems. Examples include, but are not limited to, long path interferometry (Haschberger & Tank, 1993), laser ranging (Minato & Sugimoto, 1998), communication (Pister *et al.* 1995), laser resonators (Zhou *et al.* 1982), safety devices and traffic signs (www.3m.com). Driven by these applications, many aspects of the optical properties of a CCR, such as the polarization properties (Liu & Azzam, 1997; O'Brien *et al.* 1999; Segre & Zanza, 2003),

the retroreflectivity (Eckhardt, 1971), and the maximum effective retroreflective area (Kim & Lee, 2007), have been studied extensively.

Arrays of miniature CCRs have also been explored in imaging systems. Barrett and Jacobs analyzed the imaging properties of a retroreflective array using wave propagation theory and discussed its possible application as a phase conjugator (Barrett & Jacobs, 1979). Palmer suggested the use of a retroreflector array in an imaging system with a large aperture to correct aberrations of the system (Palmer, 1985). Chipman *et al.* investigated the wavefront correction characteristics of corner cube arrays experimentally and demonstrated that a collimating lens could improve the image quality of a retroreflective screen (Chipman *et al.* 1988).

Recently a CCR array has been utilized as a retroreflective screen in head mounted projection displays (HMPD). Although many efforts have been attempted in designing compact HMPD prototypes with high-quality lightweight projection optics (Hua, 2003; Hua & Gao, 2007; Zhang & Hua, 2008), most of them primarily focused on optimizing and evaluating the optical designs of the projection optics without considering the imaging artifacts caused by a retroreflective screen. A few pilot investigations examined the imaging artifacts of a retroreflective screen. The study of the retroreflective screen for HMPD systems was initially explored by Poizat and Rolland (Poizat & Rolland, 1998). Hua *et al.* quantitatively described the effects of imperfect retroreflection on the perceived image and the exit pupil by assuming a nonzero deviation angle and a nonzero cone angle of the retroreflected light for an ideal incident ray (Hua *et al.* 2000). Subsequently, Hua *et al.* measured the retroreflectivity of various retroreflective screens

as a function of incident angles and examined the divergence profile of the retroreflected beam at a 4° incident angle (Hua *et al.* 2002).

However, few efforts were made to evaluate the overall image resolution of HMPD systems with the presence of a retroreflective screen. Furthermore, analysis on how the imaging artifacts of a retroreflective screen affect the tolerance range of a user's distance to the screen under various application scenarios haven't yet been explored before.

6.3 BASIC PROPERTIES OF A SINGLE CCR

Our discussion starts with the study of a single CCR. More specifically, the geometrical imaging properties, the effective area and the diffraction pattern of a single CCR are studied.

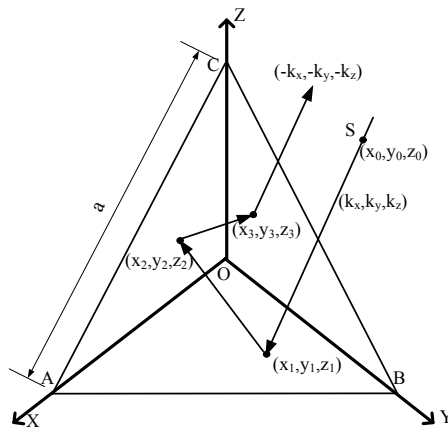


Figure 6.3 Ray tracing in a corner cube reflector

6.3.1 Geometrical imaging properties of a single CCR

Figure 6.3 illustrates a single CCR, which is an assembly of three reflective surfaces that are mutually orthogonal to each other. The vertex, O, of the CCR is defined as the origin of the coordinate system while the perpendicular dihedral edges OA, OB, and OC

are defined as the X, Y, and Z axis, respectively. The mirror surfaces (i.e. BOC, AOC, and AOB), perpendicular to the X, Y, and Z axes, lie in the YOZ, XOZ, and XOY planes, respectively. The triangle ABC forms the aperture of the corner cube and the side length of the equilateral triangular aperture is denoted as a . A hollow corner cube is assumed for simplicity. An incident ray in a direction of $\vec{k}(k_x, k_y, k_z)$ is emitted from a point source S located at (x_0, y_0, z_0) . After three consecutive reflections off the reflective surfaces AOB, AOC, BOC, the returned ray propagating in a direction of $-\vec{k}(-k_x, -k_y, -k_z)$ is laterally shifted from the incident light. The distance between the two parallel rays depends on the cube size and the direction of the incident light.

There are six possible reflective sequence orders in which a beam of light can pass through a corner cube, with the optical path depending on the direction and position of the incident ray. The six path sequences and their corresponding constraints on the incident ray direction are listed in Table 6.1. Using a ray tracing method for each path sequence, the coordinates of the intersection point of the retroreflected ray with the aperture plane of the cube are calculated and the results for all six paths are described by the same function listed in Table 6.1. Further analysis shows that the rays following different paths will converge at the point $(-x_0, -y_0, -z_0)$, forming the image of the point source S (x_0, y_0, z_0) through the CCR. This result suggests that the image formed by a CCR is point-symmetrical to the object with respect to the CCR vertex, meaning the image is rotated by 180° from the orientation of the object.

Table 6.1 Ray tracing results for six possible optical paths

Paths	Constraint	Retroreflected ray on the aperture plane
BOC->AOC->AOB	$\frac{x_0}{k_x} > \frac{y_0}{k_y} > \frac{z_0}{k_z}$	Coordinate: $(-x_0 + \frac{x_0 + y_0 + z_0 + 1}{k_x + k_y + k_z} k_x,$ $-y_0 + \frac{x_0 + y_0 + z_0 + 1}{k_x + k_y + k_z} k_y,$ $-z_0 + \frac{x_0 + y_0 + z_0 + 1}{k_x + k_y + k_z} k_z)$ Direction: $(-k_x, -k_y, -k_z)$
BOC->AOB->AOC	$\frac{x_0}{k_x} > \frac{z_0}{k_z} > \frac{y_0}{k_y}$	
AOC->BOC->AOB	$\frac{y_0}{k_y} > \frac{x_0}{k_x} > \frac{z_0}{k_z}$	
AOC->AOB->BOC	$\frac{y_0}{k_y} > \frac{z_0}{k_z} > \frac{x_0}{k_x}$	
AOB->BOC->AOC	$\frac{z_0}{k_z} > \frac{x_0}{k_x} > \frac{y_0}{k_y}$	
AOB->AOC->BOC	$\frac{z_0}{k_z} > \frac{y_0}{k_y} > \frac{x_0}{k_x}$	

6.3.2 Effective area of a CCR

As noted above, only the rays that experience three consecutive reflections can be retroreflected. As a result, only a fraction of rays incident upon a CCR aperture can be effectively retroreflected and defines the effective aperture of a corner cube. The shape and size of the effective aperture of a CCR depend not only on the size of the CCR, a , but also on the angle of the incident rays.

A ray tracing method is used to characterize the effective aperture of a CCR. The following part summarizes the analytical results of the effective aperture of a CCR, while the detailed derivation can be found in Appendix A.

As shown in Figure 6.3, the side length of the equilateral triangular aperture of the CCR is denoted as a and the function of the aperture plane is given by

$$\frac{x}{a} + \frac{y}{a} + \frac{z}{a} = \frac{1}{\sqrt{2}} \quad (6.1)$$

where the coordinate has the same definition as Section 6.3.1.

Based on the ray tracing results, for a ray in the direction of $\vec{k}(k_x, k_y, k_z)$, in order to be retroreflected by a CCR, the following condition should be met

$$\begin{aligned} x_i &< \frac{\sqrt{2}a \cdot k_x}{k_x + k_y + k_z} \\ y_i &< \frac{\sqrt{2}a \cdot k_y}{k_x + k_y + k_z} \\ z_i &< \frac{\sqrt{2}a \cdot k_z}{k_x + k_y + k_z} \end{aligned} \quad (6.2)$$

where the point (x_i, y_i, z_i) is the intersection point of the ray with the aperture plane of the CCR. Since the point (x_i, y_i, z_i) locates within the physical boundary of the CCR aperture ABC, the following constraints should be met

$$\begin{aligned} x_i &> 0 \\ y_i &> 0 \\ z_i &> 0 \end{aligned} \quad (6.3)$$

Given that the point (x_i, y_i, z_i) is on the aperture plane, its coordinates are further constrained by

$$\frac{x_i}{a} + \frac{y_i}{a} + \frac{z_i}{a} = \frac{1}{\sqrt{2}}. \quad (6.4)$$

Equations (6.2) through (6.4) give a complete definition on the effective aperture.

Take a normal incident ray bundle with $k_x = k_y = k_z$ as an example. The effective area is

formed by the aperture boundary and the constraints of $x < \frac{2a}{3\sqrt{2}}, y < \frac{2a}{3\sqrt{2}}$ and

$z < \frac{2a}{3\sqrt{2}}$. As shown in Figure 6.4, the effective aperture is the dotted area with a

hexagonal shape and its side length is $\frac{a}{3}$. The effective area is 66.7% of the whole

aperture of ABC. In the following sections, we use a circular aperture with a diameter of $0.606a$, which has the same area as the hexagonal aperture, to equivalently characterize the size of the effective area.

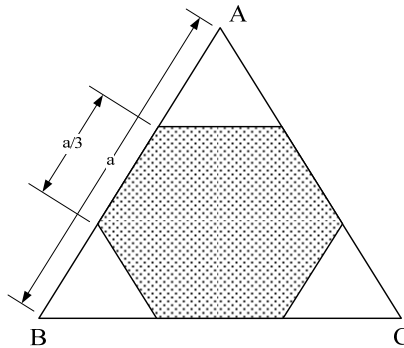


Figure 6.4 Effective aperture of a CCR for a normal incident angle

The area of the effective aperture of a CCR varies as a function of a ray's incident angle. The calculation results are plotted as a function of (θ, φ) , which is defined in figure 6.5(a). An $X'Y'Z'$ coordinate is defined, in which Z' axis passes through the vertex of the CCR and is perpendicular to the aperture plane while Y' axis goes through the point A and is perpendicular to the line BC. The polar angle θ is defined as the angle between the incident ray and Z' axis while the azimuthal angle φ is the angle between the projected vector of the incident ray on the $X'Y'$ plane and X' axis.

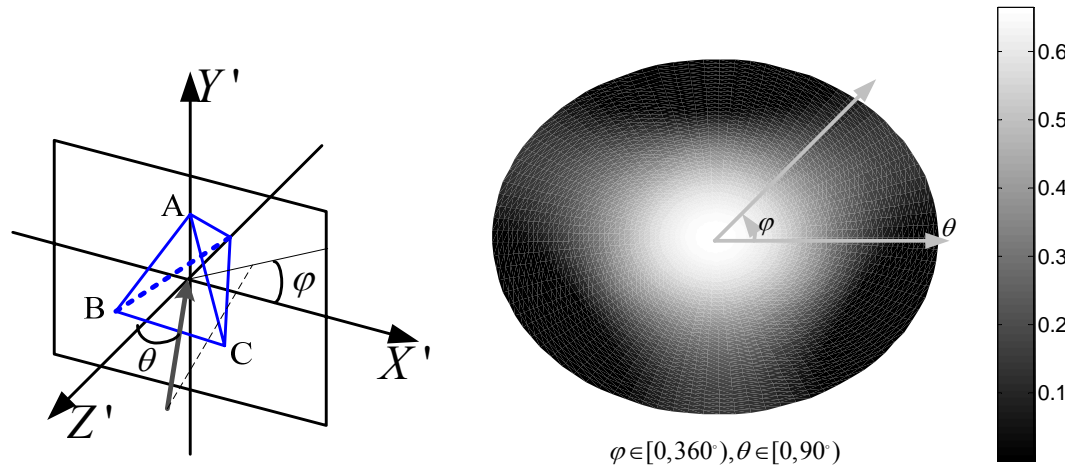


Figure 6.5 (a) (θ, φ) is defined in the $X'Y'Z'$ coordinate (b) The ratio of the area of the effective aperture to the area of the physical aperture as a function of θ and φ .

As shown in figure 6.5(b), the area ratio of the effective aperture to the physical aperture is plotted as a function of θ and φ . The maximum effective aperture is obtained when the light is normally incident on the retroreflective aperture. The area of effective aperture is symmetrical with φ when θ is less than 45° . The detailed derivation is in Appendix A.

6.3.3 Diffraction pattern of a CCR

From the geometrical imaging point of view, a single CCR forms a virtual image point symmetrical to the object point with respect to the CCR vertex. The retroreflected ray bundle is virtually emitted from the image point. Since the aperture size of a CCR in a retroreflective screen is small (i.e. at the magnitude of $100 \mu\text{m}$), diffraction effect could have a significant impact on the image pattern observed in the retroreflective path (i.e. on the same side of the aperture as the object). In this section, the diffractive pattern of the retroreflected light through a CCR is studied. For the purpose of the study of a retroreflective screen in following sections, the observation plane is set to be at the same

distance from the CCR as the source.

As illustrated in Figure 6.6, the object point is defined as the origin of XYZ coordinate and Z axis is vertical to the aperture plane of the CCR. The distance from the object point to the CCR aperture is denoted as d . Thus, for a CCR with its vertex point O at (x_0, y_0, d) , the geometric image I_0 of the point source S is located at $(2x_0, 2y_0, 2d)$. In the calculation of the wave propagation, two approximations are made. First, since the corner cube size a is significantly smaller than distance d , the thickness of a CCR is negligible comparing with d in the calculation. Second, the effective aperture of a CCR for the incident ray bundle from point source S is defined by the direction of the chief ray of the incident ray bundle, which is the ray passing through the vertex of the CCR, since the half cone angle of ray bundle δ ($\sim \frac{a}{2d} \ll 1$) is small enough.

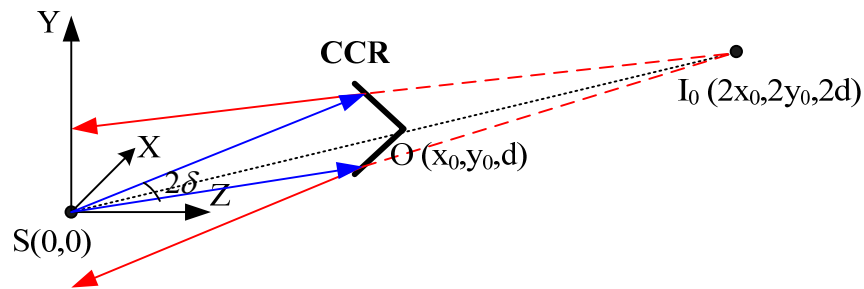


Figure 6.6 Diffractive retroreflected light through a CCR

As shown in Table 6.1, there are six different sequences of reflecting paths through which an incident beam can pass through a CCR. The retroreflected light through different paths ends up with different polarization states which are determined by the optical properties of the reflective surfaces (Liu & Azzam, 1997). The diffraction pattern can be calculated by combining the beams with different polarization states that emerge

from the six sectors of a CCR aperture. Chang *et al* showed that the far-field diffraction pattern of a CCR with aluminum-coated reflective surfaces is approximately the Fourier transform of the exit aperture of the cube, due to the fact that the polarization effect of each path is so small that it doesn't significantly affect the energy distribution of the diffraction pattern (Chang *et al.* 1970). In this work, we limit the study to aluminum-coated CCR arrays which are commonly used in HMPD systems and the beams emerging from the six sectors of a CCR aperture are treated as a single beam through the effective aperture of a CCR.

As shown in Figure 6.6, the wavefront leaving the effective aperture of the CCR, virtually emitted from point I_0 , is given by

$$U_{RR}(x, y) = \mathbf{exp} \left(\frac{i\pi [(x - 2x_0)^2 + (y - 2y_0)^2]}{d\lambda} \right) t(x - x_0, y - y_0) \quad (6.5)$$

where $t(x - x_0, y - y_0)$ is the effective exit aperture of the CCR with its vertex point at (x_0, y_0) . The retroreflected wavefront continues to propagate and the wavefront function on the observation plane is given by

$$U_d(x, y) = \mathbf{exp} \left(\frac{i(x^2 + y^2)\pi}{d\lambda} \right) \mathfrak{F} \left\{ U_{RR}(x', y') \mathbf{exp} \left(\frac{i(x'^2 + y'^2)\pi}{d\lambda} \right) \right\}_{\xi = \frac{x}{\lambda d}, \eta = \frac{y}{\lambda d}} \quad (6.6)$$

The irradiance distribution of the image pattern observed can be obtained by

$$I(x, y) = |U_d(x, y)|^2 \quad (6.7)$$

Based on the Equations 6.5~6.7, the retroreflected pattern can be calculated. A geometrical model and a far-field diffraction model can be used corresponding to the

conditions of $d < \frac{2}{\lambda} \left(\frac{a_{eff}}{2}\right)^2$ and $d \gg \frac{2\pi}{\lambda} \left(\frac{a_{eff}}{2}\right)^2$, respectively.

When d is small and meets the condition of $d < \frac{2}{\lambda} \left(\frac{a_{eff}}{2}\right)^2$, corresponding to Fresnel number $N_f > 1$, the geometrical boundary can be used to characterize the spot size of the retroreflected ray pattern. As shown in Figure 6.6, since the image point locates at the symmetrical position of the object point over the vertex of the CCR, the geometrical size of the blur on the observation plane, which is also the object plane, is twice as large as the effective aperture of the CCR based on the geometrical relations. The geometrical diameter is given by

$$D_{geo} = 2a_{eff} \quad (6.8)$$

where a_{eff} is the size of the effect aperture which is a function of incident angle of the chief ray. If the chief ray of the ray bundle is normal incident on the CCR aperture, the image spot is in a hexagonal shape with a side length of $\frac{2a}{3}$ and the equivalent diameter of the blur is $1.212a$.

On the other hand, when $d \gg \frac{2\pi}{\lambda} \left(\frac{a_{eff}}{2}\right)^2$, corresponding to the Fraunhofer approximation condition, the far-field diffraction pattern of a CCR is approximately the Fourier transform of the exit aperture of the cube. The effective exit aperture of a corner cube is not the physical aperture of the CCR but varies with the angle of incident light, which suggests that the diffraction distribution of the light varies as a function of incident angle. For simplicity we here limit the diffraction pattern analysis to the on-axis field

angle. The diffraction pattern of other incident angles can be analyzed in a similar fashion by determining the effective aperture functions as shown in section 6.3.2. A fast Fourier transform method was used to calculate the Fourier transform of the effective exit pupil. Figure 6.7 shows the amplitude distribution of the diffraction pattern of a CCR with a hexagonal effective aperture for the normal incident angle, in which all the parameters, such as the cube size, the wavelength, and the image distance, were assumed to be unit parameters. The diameter of the central bright area representing the zero-order diffraction pattern is 4.08, while the energy encircled within this area is 83.5% of the total energy. By scaling the diffraction pattern with the wavelength λ , the aperture size a , and the absolute distance d from an image source to the aperture plane, the diameter of the zero-order diffraction pattern is give by

$$D_{diff} = \frac{4.08\lambda d}{a} = \frac{2.47\lambda d}{0.606a}. \quad (6.9)$$

where $0.606a$ is the equivalent diameter of the effective area. The result is consistent with the diameter of an airy disk.

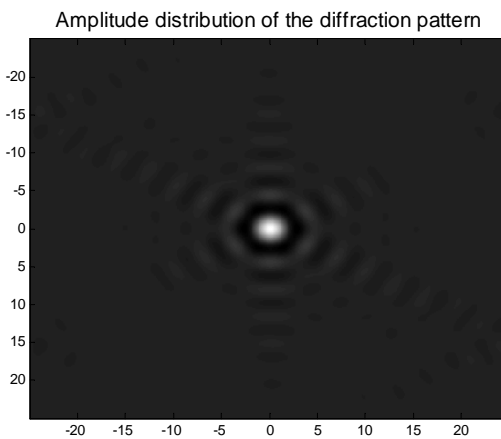


Figure 6.7 Diffraction pattern of a CCR for normal incident light

Taking the CCR in the retroreflective screen used in our HMPD systems for example, it has an effective aperture of 121 μm for normal incident light. For the wavelength of 550nm, Fraunhofer approximation can be used when

$$d \gg \frac{2\pi}{\lambda} \left(\frac{a}{2}\right)^2 = \frac{2\pi}{550 \times 10^{-9} \text{m}} (60.5 \times 10^{-6} \text{m})^2 = 4.1 \text{cm}$$

and the spot diameter is $0.011d$, while the geometrical approximation may be used when $d < \frac{2}{\lambda} \left(\frac{a_{\text{eff}}}{2}\right)^2 = 1.3 \text{cm}$ and the spot diameter is 242 μm .

6.4 IMAGING PROPERTIES OF A CCR ARRAY BASED RETROREFLECTIVE SCREEN

Based on the basic properties of a single CCR discussed in the previous section, the imaging properties of a retroreflective screen composed of a 2D array of CCRs are analyzed in this section. We assume that the 2D array is composed of identical CCRs, each of which possesses an equilateral triangular aperture with side length of a .

The analysis of the imaging effects of a retroreflective screen may be categorized into two cases depending on the distance, d , between the source object and the retroreflective screen as well as the half cone angle, δ , of the ray bundle from a source point.

Case 1: the object plane is close enough to the aperture plane of the retroreflective screen so that the incident ray bundle from a source point S covers no more than one corner cube, that is $|d| \leq d_0 = \frac{a}{2 \tan(\delta)}$. This is a trivial case where the diffraction effect

is negligible and geometrical effects dominate. Figure 6.8 illustrates an example of this case, where the object plane coincides with the aperture plane of the corner cube array. Only the light from the object points which locate within the effective aperture of a CCR can be effectively retroreflected while the object points locate outside of the effective aperture will not be retroreflected. Each unit segment of the object within the effective aperture of a CCR, which is labeled by consecutive integers (e.g. 1, 2, 3 etc.), is imaged by a corresponding CCR in the array. The image of a unit segment is formed at the symmetrical position of the object over the vertex of the corresponding CCR. The array of the unit images follows the same arrangement as the unit object array, with each unit image rotated by 180° from the orientation of the corresponding unit object. These rotated unit images are labeled by consecutive integers with primes (e.g. 1', 2', 3' etc.). Although the overall image will appear similar to the object, the image detail has a slight variation from the object due to the local 180° rotation effect. As a result, the image artifact is as large as $2a_{eff}$ in the retroreflected image. In this case, the resolution of the retroreflected image is limited by the effective aperture size of the corner cube.

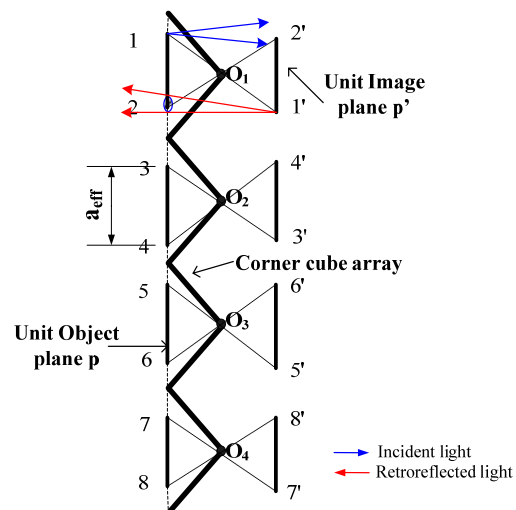


Figure 6.8 Imaging effect of a CCR array when the object plane coincides with the aperture plane of the CCR array ($|d|=0$)

Case 2: the object plane is far enough from the aperture plane of the retroreflective screen so that the incident ray bundle from a source point S covers more than one corner cubes. This is the most common case and the distance d meets the condition of

$$|d| > d_0 = \frac{a}{2 \tan(\delta)}. \quad (6.10)$$

The following sub-sections will focus on discussing the effects corresponding to the case 2.

6.4.1 Geometrical imaging effect

Without loss of generality, we select an arbitrary 2D plane passing through the object point and the collinear vertices of a CCR array for the discussion in this Section. The intersection line of the selected plane with the aperture plane of the CCR array defines a line aperture. Figure 6.9 shows the cross-section of the CCR array with a 2D plane. The ray bundle from the object point S impinges on multiple CCRs (e.g. O_0 , O_1 and O_2). Based on the raytracing concepts of Section 6.2, multiple virtual image points (e.g. I_0 , I_1 , and I_2) are formed through these corner cubes and are located at the symmetrical positions of the object point with respect to the vertices of the corresponding CCRs. The ray passing through the vertex of each CCR, which is defined as the chief ray for the corresponding CCR, would be retroreflected back to the object point. The retroreflected ray bundles from each CCR, which are centered around the corresponding chief rays and virtually emitted from different image points (i.e. I_0 , I_1 , I_2), will converge

toward the object point S, and a minimally blurred spot centered on the object point S will be formed on the object plane. Thus, for an extended object, the image plane of the object through a retroreflective screen coincides with the object plane and the image spot for each object point centers on the object point itself.

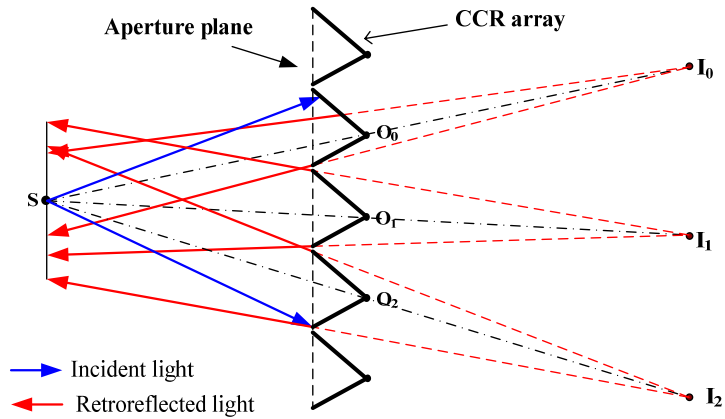


Figure 6.9 Illustration of geometrical imaging effect through a CCR array in a 2D plane

To characterize the spot size of the blurred image formed by a retroreflective screen, we select an arbitrary CCR and evaluate the footprint size of its retroreflected ray bundle on the object plane. As discussed in Section 6.3.3, the geometrical spot size of the retroreflected light on the object plane is $2a_{eff}$, where a_{eff} is the effective aperture size of the CCR.

The spot size of the blurred image formed by a CCR array can then be obtained by combining the footprints of the retroreflected ray bundles from all individual CCRs within the coverage of the incident ray bundle, give by

$$D_{geo-blur} = \max \{2a_{eff}(O_{0,1,\dots,n})\} < 2a \quad (6.11)$$

where $a_{eff}(O_{0,1,\dots,n})$ denotes the effective aperture size of each individual CCR (e.g. O_0 ,

O_1, \dots, O_n) covered by the incident ray bundle. The spot size is hereby characterized by the largest effective apertures among the covered CCRs. Because the effective aperture of a CCR is no larger than the aperture of a CCR, a , the image spot of a retroreflective screen is smaller than $2a$.

When the cone angle of the incident ray bundle from an object point is small, the variation of the size and shape of the effective aperture in this case is small enough to be neglected and the incident angles of the ray bundle can thus be approximated by its chief ray direction. For instance, in a typically HMPD system, the cone angle of the incident ray bundle on a retroreflective screen is smaller than 1° , determined by the exit pupil size (typically around 10 mm) and the relatively long image projection distance (typically at least 0.5 m). The chief ray direction of a given object is defined by its polar angle θ and azimuthal angle φ , the Equation 6.11 can be rewritten as

$$D_{geo-blur} = 2a_{eff}(\theta, \varphi) \quad (6.12)$$

where $a_{eff}(\theta, \varphi)$ is the effective aperture of a CCR for a parallel ray bundle in the direction of (θ, φ) . Therefore, for an object with a small cone angle, the geometrical image spot from the retroreflective screen is twice as large as the effective aperture of the CCR, which is a function of the chief ray angle. Taking the example when the incident ray bundle is normal to the aperture plane, the image spot is in a hexagonal shape with the side length of $\frac{2a}{3}$ and the equivalent diameter of the blur is $1.212a$.

To validate the above theoretical analysis, we simulated the imaging process of a CCR array using LightTools®. As shown in Fig. 6.10(a), a retroreflective screen was

modeled, consisting of identical CCRs with a side length of $a=141\ \mu\text{m}$ for the triangular aperture. A point source was placed at a distance of 20 mm away from the screen. The emission profile of the source is defined by three parameters: the half cone angle of the ray bundle δ and the chief ray angle (θ, φ). A receiver was placed at the conjugate position of the source over a beamsplitter to evaluate the image formed by the retroreflective screen. Both the half cone angle δ and chief ray polar angle θ were varied while φ was fixed as 0° . A subset of the simulation results is shown in Table 6.2. The rows correspond to the results for the half cone angle δ of 0.5° and 10° , respectively. The results for the half cone angle δ of 0.5° simulate typical ray configurations in an HMPD-like system. The columns correspond to the results for three different chief ray polar angle θ : 0° , 15° , and 30° , respectively. The white reference circle in each pattern has a diameter of $2a$ and all the patterns are limited within the white reference circle. When $\theta=0^\circ$ and $\delta=0.5^\circ$, which represent the on-axis field and a ray bundle with a small cone angle, the simulated image demonstrates a hexagonal pattern twice as large as the hexagonal effective aperture of the CCR. As expected, the resultant image spot for off-axis fields (e.g. $\theta=15^\circ$ and 30°) is the combination of the effective apertures of two types of the CCRs: pointing-down CCRs and pointing-up CCRs. A microscopic image of a CCR array is shown in Fig. 6.10(b) to demonstrate the two types of orientations. The effective apertures of these two types of CCRs are the same for normal incident light but different for off-axis fields. The spot patterns for $\delta=10^\circ$ are similar to those with $\delta=0.5^\circ$, but their boundaries are blurred, which is due to the fact that the effective aperture has more significant variation across the ray bundle when the ray bundle is large.

Table 6.2 Simulation results: the geometrical imaging effect of a retroreflective screen

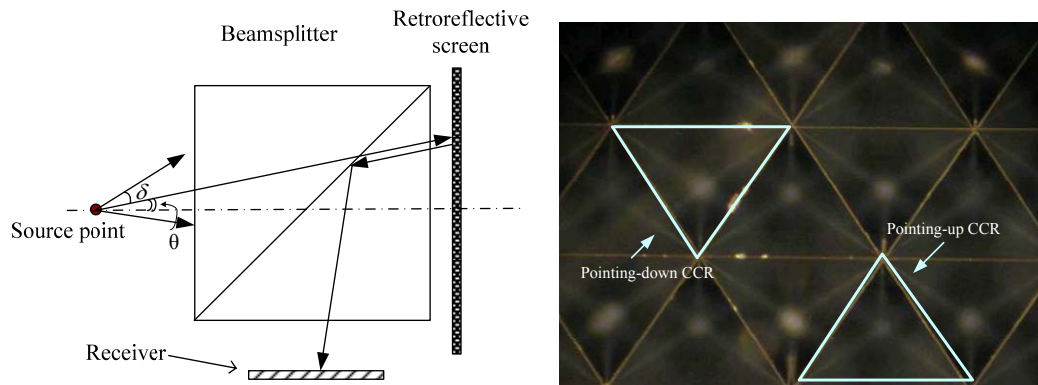
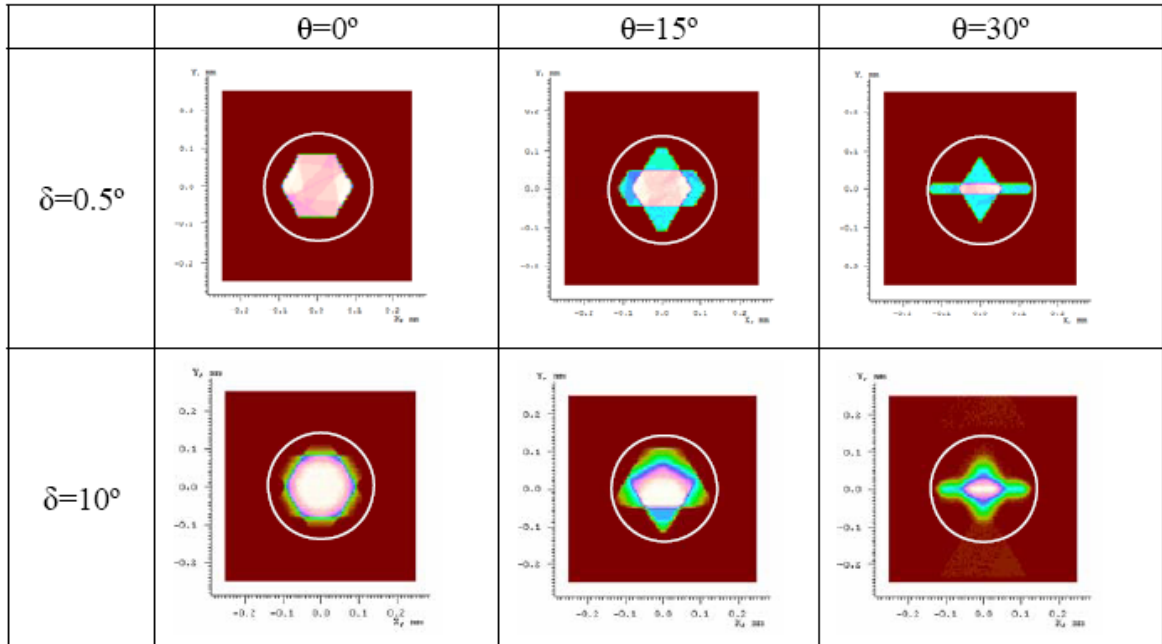


Figure 6.10 (a) Simulation setup in LightTools® (b) a microscopic image of a CCR array

6.4.2 Diffractive pattern of a retroreflective screen

As shown in Figure 6.9, from the geometrical imaging perspective, light incident on individual CCRs from an object point S converges on the object plane and forms a minimally blurred image spot centered on the object point. As discussed in Sec. 6.3.3, the

diffraction effects of small CCRs could have significant effects on the resultant image pattern. In this section, we extend the discussion from a geometrical model to a diffractive model using the wave propagation method. Using the same approach in Section 6.3.3, the wavefront function $U(x, y)_{o_i, \lambda}$ on the image plane from a given single CCR at a given wavelength could be calculated. The irradiance distribution of the image pattern at the wavelength of λ by a CCR array can be obtained through

$$I(x, y)_\lambda = \left| \sum_{o_i \in A_i} U(x, y)_{o_i, \lambda} \right|^2. \quad (6.13)$$

A_i represents the region on the retroreflective screen covered by the ray bundle from object point S. For the incident light with visible spectrum, the irradiance distribution is given by

$$I(x, y) = \int_{\lambda_b}^{\lambda_r} I(x, y)_\lambda S(\lambda) d\lambda \quad (6.14)$$

where $S(\lambda)$ is the spectral distribution of incident light and $[\lambda_b, \lambda_r]$ represents the spectrum range of the visible light.

When $d \gg \frac{2\pi}{\lambda} \left(\frac{a_{eff}}{2}\right)^2$, corresponding to the Fraunhofer approximation condition,

the image spot size centered on the object point S can be obtained by combining the far-field diffraction wavefront of individual CCRs within the coverage of the incident ray bundle. The amplitude distribution of the far-field diffractive pattern of a retroreflective on the object plane was simulated using Matlab as shown in Figure 6.11 (a). In the simulation, monochromatic source with the wavelength of 550nm was used while the distance d was set to be 1m and the half cone angle δ is 0.5° . For the comparison, the

amplitude distribution of the diffraction pattern of a single CCR is plotted in Figure 6.11 (b). As shown in Figure 6.11(a) and (b), the diffractive pattern through a retroreflective screen is composed of multiple gratings with their amplitudes modulated by the diffractive pattern of a single CCR (Barrett & Jacob, 1979). The gratings are generated through the interference of the ray bundles from individual CCRs. The interference only changes the local amplitude distribution while the overall amplitude distribution is determined by the diffractive pattern of each single CCR. In other words, for an extended object with visible spectrum, the imaging degradation through the retroreflective screen is barely affected by the interference effect. Thus, to avoid the complex and tedious computations based on Equation 6.14, the blur size through a retroreflective screen could be evaluated based on the sum of the irradiance from each individual CCR. For an object with its ray bundle in the visible spectrum and in a small cone angle, the retroreflected ray bundles from each individual CCR overlap on the observation plane. The spot size of a retroreflective screen can be determined by the diffractive pattern of a single CCR, and for the far field diffraction, the spot is given by $D_{diff} = \frac{4.08\lambda d}{a}$.

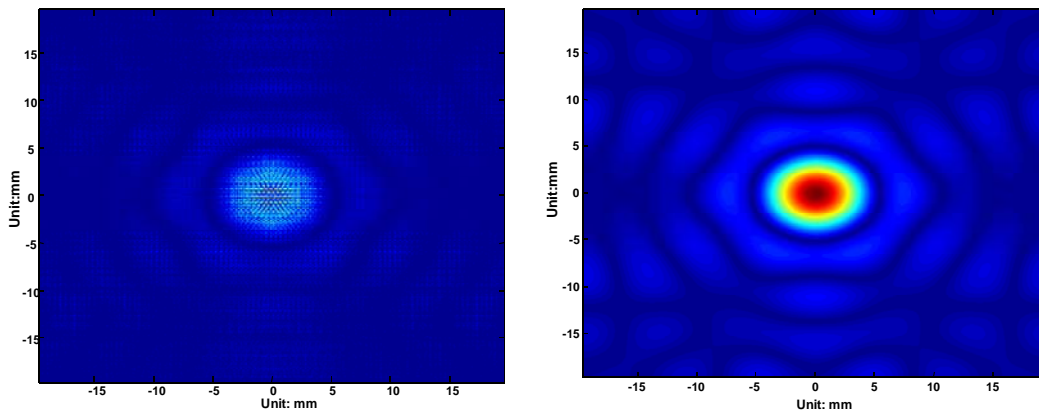


Figure 6.11 Amplitude distribution on the object plane (a) through the a retroreflective screen (b) through a single CCR

6.5 IMAGE RESOLUTION OF A RETROREFLECTIVE SCREEN IN AN HMPD SYSTEM

In Section 6.4, we evaluated the spot size of a retroreflective screen on the image plane where the minimum blur is formed without taking into account the viewing configuration of an HMPD system. In this section, we examine the effective spatial resolution of a retroreflective screen observed by a user wearing an HMPD system and analyze the tolerance range of an HMPD user's movement under different display settings based on the analysis of the imaging artifacts of a retroreflective screen.

6.5.1 Image resolution analysis method

Since the focus of this section is to analyze the degradation of image resolution caused by imaging artifacts of a retroreflective screen discussed in Section 6.4, the front-end projection system in an HMPD is assumed to be perfect, yielding infinitely high spatial resolution. With this assumption, Figure 6.12 illustrates a simplified view of an HMPD system, where the projection lens forms a projected image point S after the reflection by a beam splitter or PBS. The distance from the exit pupil of the projection lens, which also corresponds to the entrance pupil of a viewer's eye, to the image point S is denoted as z_i . The projected light from S strikes on the retroreflective screen and is then retroreflected back toward the eye pupil. The retroreflective screen is placed at a distance of d from the image plane of the projection optics. Within a tolerance range, the distance from the exit pupil to the retroreflective screen has the flexibility of being closer or farther than the focusing distance z_i , allowing for user mobility in a 3D environment.

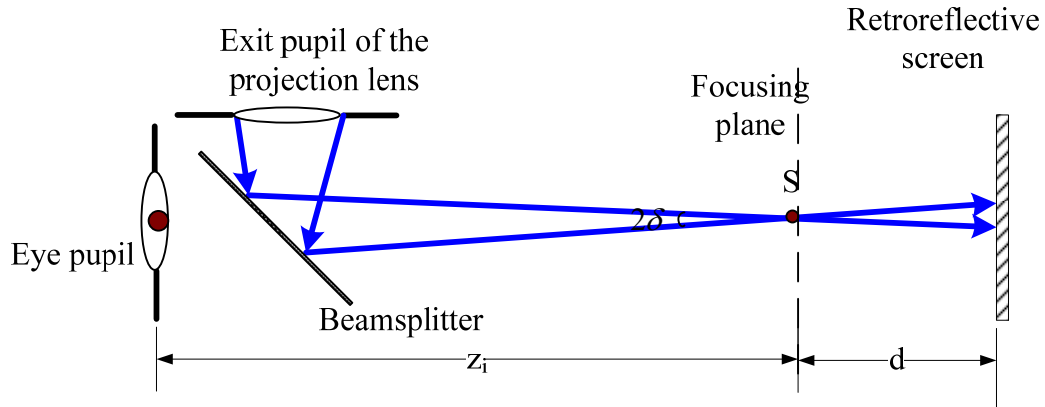


Fig. 6.12 Simplified view of an HMPD/p-HMPD setup

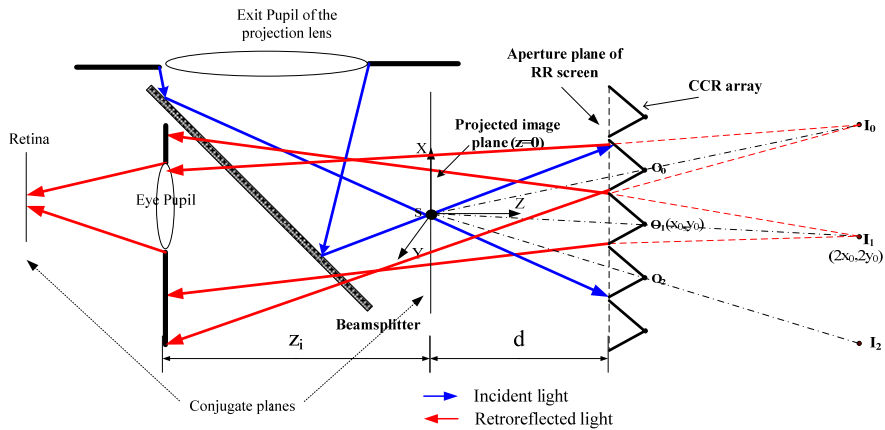


Fig 6.13 Imaging by a corner cube array when $|d| > d_0$

Similar to Section 6.4, the study of the retroreflective screen in an HMPD can be divided into two cases depending on the distance d .

Case 1: the projected image plane, which is also the object plane for the retroreflective screen, is close enough to the aperture plane of the retroreflective screen so that the incident ray bundle from a source point S covers no more than one corner cube, that is $|d| \leq d_0 = \frac{a}{2 \tan(\delta)}$. Similar to the discussion in Sec 6.4, the image artifact caused

by the 180° degree rotation effect is as large as $2a_{eff}$ in the retroreflected image.

Case 2: the projected image plane is far enough from the aperture plane of the retroreflective screen so that the incident ray bundle from a source point S covers more than one corner cubes, which meet the condition of $|d| > d_0 = \frac{a}{2 \tan(\delta)}$. Due to the sampling effects of the eye pupil, the effective resolution of a retroreflective screen in an HMPD, which will be analyzed in this section, is expected to be better than the results in Section 6.4.2.

Fig 6.13 illustrates the light propagation in an HMPD system. The drawing of the system is not in scale. The light from the projection lens is reflected by a beamsplitter and is focused on the projected image plane. The object point S is defined as the origin of the reference coordinates XYZ, while the object plane coincides with the XY plane and the Z-axis is parallel to the optical axis. The ray bundle from the point S impinges on multiple CCRs (e.g. O_0 , O_1 and O_2). Based on the raytracing concepts in Section 6.4, multiple virtual image points (e.g. I_0 , I_1 , and I_2) are formed through these corner cubes and are located at the symmetrical positions of the object point with respect to the vertices of the corresponding CCRs. As discussed in Section 6.4, a minimally blurred image spot centered on the object point S is formed if a physical observation screen is placed at the corresponding position. In an HMPD system, however, only a small fraction of the retroreflected rays may enter the eye pupil and form a retinal image. This pupil sampling effect, as illustrated in Fig. 6.13, is significant. As a result, the effective spatial resolution observed by a viewer is expected to be better than the blurred spot obtained in

Section 6.4.

To evaluate the effective spatial resolution observed by a viewer, let us consider the ray bundle retroreflected by the CCR $O_1(x_0, y_0)$ as an example. Similar to the single CCR discussion in Section 6.3.3, the retroreflective wavefront leaving the effective aperture of the CCR, virtually emitted by point I_1 , is given by

$$U_{RR}(x, y)_{(x_0, y_0)} = \mathbf{exp} \left\{ \frac{i\pi \left[(x - 2x_0)^2 + (y - 2y_0)^2 \right]}{d\lambda} \right\} t(x - x_0, y - y_0) \quad (6.15)$$

where $t(x - x_0, y - y_0)$ is the effective aperture function of the CCR with its vertex at (x_0, y_0) and d is the distance between S and CCR aperture plane in Z direction. The retroreflected wavefront continues to propagate and is incident on the pupil plane of the eye. Before passing through the pupil, the wavefront is given by

$$U_{p-}(x, y)_{x_0, y_0} = \mathbf{exp} \left(\frac{i(x^2 + y^2)\pi}{(d + z_i)\lambda} \right) \mathfrak{F} \left\{ U_{RR}(x', y')_{x_0, y_0} \mathbf{exp} \left(\frac{i(x'^2 + y'^2)\pi}{(d + z_i)\lambda} \right) \right\}_{\xi = \frac{x}{\lambda(d + z_i)}, \eta = \frac{y}{\lambda(d + z_i)}} \quad (6.16)$$

where $d + z_i$ is the distance from the retroreflective screen to the eye. After the light passes through the pupil, the wavefront function is given by

$$U_{p+}(x, y)_{(x_0, y_0)} = U_{p-}(x, y)_{(x_0, y_0)} p(x, y) \quad (6.17)$$

where $p(x, y)$ is the pupil function. Considering Stiles-Crawford effect which states that the efficiency of peripheral rays through pupil is lower than the central ray, an apodizing filter can be applied to the pupil function:

$$p(x, y) = \mathbf{exp} \left[-0.105 \cdot (x^2 + y^2) \right] \mathit{cyl} \left(\frac{\sqrt{x^2 + y^2}}{r_p} \right) \quad (6.18)$$

where r_p is the radius of the eye pupil and is set to be 2mm in the calculation. $\mathit{cyl}(r)$ is a

cylinder function and is defined as the

$$cyl(r) = \begin{cases} 0 & r > 1 \\ 1 & r \leq 1 \end{cases}. \quad (6.19)$$

By neglecting the eye aberrations and assuming it being a diffraction limited system, the wavefront function after the eye system is give by

$$U_{eye}(x, y)_{x_0, y_0} = U_{p+}(x, y)_{x_0, y_0} \exp\left[-\frac{i(x^2 + y^2)\pi}{f_e \lambda}\right] \quad (6.20)$$

while f_e is the effective focal length of the eye. The ray bundle is focused on the retina by the eye and the image distribution on the retina is given by

$$\left| U_{retina}(x, y)_{x_0, y_0} \right| = \left| \mathfrak{F} \left\{ U_{p+}(x', y')_{x_0, y_0} \exp\left[\frac{i(x'^2 + y'^2)\pi}{\lambda} \left(-\frac{1}{f_e} + \frac{1}{z'_i} \right) \right] \right\} \right|_{\xi = \frac{x}{\lambda z'_i}, \eta = \frac{y}{\lambda z'_i}} \quad (6.21)$$

while z'_i is the distance between eye lens to retina and can be obtained through the lens equation

$$-\frac{1}{f_e} + \frac{1}{z'_i} = -\frac{1}{z_i}. \quad (6.22)$$

As a result, the light distribution on the retina can be written as

$$\left| U_{retina}(x, y)_{(x_0, y_0)} \right| = \left| \mathfrak{F} \left\{ U_{p+}(x', y')_{x_0, y_0} \exp\left(\frac{i(x'^2 + y'^2)\pi}{\lambda z_i} \right) \right\} \right|_{\xi = \frac{x}{\lambda z'_i}, \eta = \frac{y}{\lambda z'_i}} \quad (6.23)$$

The wavefront on the retina is the sum of the wavefront from multiple CCRs and the irradiance distribution at the wavelength of λ on the retina plane is given by

$$I(x, y)_\lambda = \left| \sum_{(x_i, y_i) \in A_i} U_{retina}(x, y)_{(x_i, y_i), \lambda} \right|^2 \quad (6.24)$$

where A_i represents a complete set of the vertices coordinate $\{(x_1, y_1), (x_2, y_2), \dots, (x_n, y_n)\}$ of the CCRs covered by the ray bundle from S. For the incident light with visible spectrum,

the final irradiance is given by

$$I(x, y) = \int_{\lambda_b}^{\lambda_r} I(x, y)_\lambda S(\lambda) d\lambda \quad (6.25)$$

where $S(\lambda)$ has the same definition with Equation 6.14.

The diameter D of the area of A_i in Equation 6.24 could be obtained through the equation

$$\frac{D}{d} = \frac{RBD}{z_i} \quad (6.26)$$

where RBD is the ray bundle diameter at the pupil plane of the projection lens. In the design, RBD should be equal or smaller than the physical pupil size of the projection lens.

The final irradiance distribution of the image spot can be obtained using Equation 6.25. However, tremendous computations are required to simulate the final irradiance distribution. Similar to the discussion in section 6.4.2, the interference effect between the ray bundles from multiple CCRs may change the local distribution of the final image on the retina, but it barely affects the image spot size through a retroreflective screen for an extended object with its spectrum in visible range. To evaluate the spot size of a retroreflective screen in an HMPD, the sum of the irradiance pattern from each individual CCRs is obtained and the Root Mean Square (RMS) diameter of the pattern is calculated to characterize the effective resolution of a retroreflective screen in an HMPD.

6.5.2 Image resolution calculation

In this section, the effective resolution of a retroreflective screen in an

HMPD/p-HMPD is calculated based on the theoretical analysis in Sec 6.5.1.

For an HMPD system, the distance z_i is typically set to match the requirements of an application in order to minimize viewing discomfort and to ease stereo fusion caused by the accommodation-convergence depth discrepancy plaguing most existing stereoscopic displays (Sugihara *et al.* 1999). The various application scenarios may be categorized into three-types: arm-length, middle-range, and far-field. The arm-length applications refer to the scenarios where the 3D scene to be displayed is at about an arm-length distance from the viewer (e.g. workbench-type applications and surgical visualization). The display optics is typically focused at a distance of around 1m in these applications. The far-field applications refer to the scenarios where the 3D scene is considerably far from the viewer (e.g. flight simulation or battlefield visualization). The display optics is typically focused at a distance of 4m or larger for these scenarios. The middle-range applications refer to the scenarios where the 3D scene is primarily somewhere between the arm-length and far-field distance (e.g. immersive walk-through applications and vehicle simulation). In this case, the display optics is typically focused at a distance of about 2m. In the following analysis, the angular resolution for all three focusing setups is evaluated.

The angular resolution of a retroreflective screen in a p-HMPD is affected by multiple factors, such as the distance, d , between projected image plane and the retroreflective screen, the projected image distance z_i , the ray bundle diameter (RBD) from the exit pupil of the projection lens and the corner cube size a . The simulation is only performed for the on-axis field angle, in which the ray bundle from S is

approximately normal to the retroreflective screen. The analysis for the off-axis fields can be performed in the similar way.

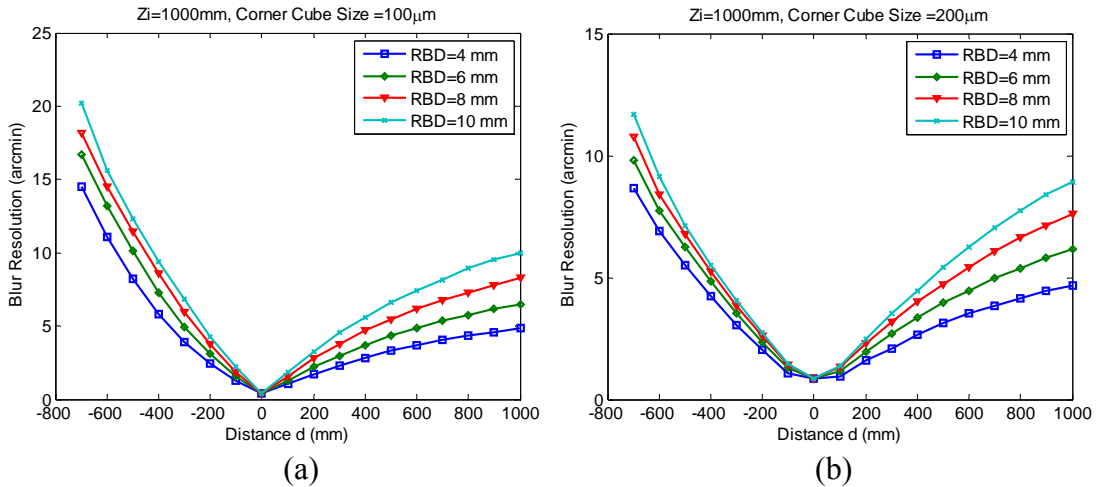


Figure 6.14 Angular resolution at the project image distance z_i of 1m as a function of the distance d and the ray bundle size (RBD) when the corner cube size is equal to (a) $100 \mu\text{m}$ and (b) $200 \mu\text{m}$

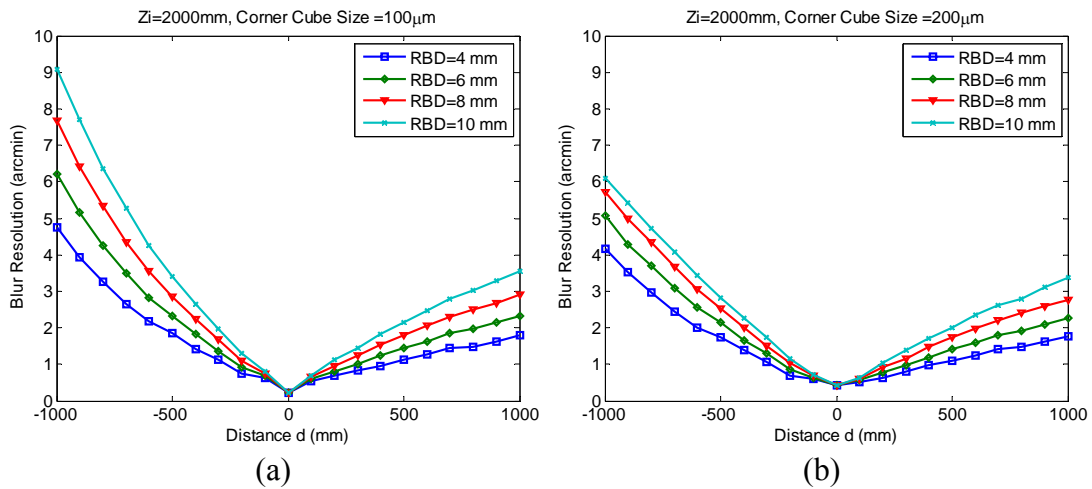


Figure 6.15 Angular resolution at the project image distance z_i of 2m as a function of the distance d and the ray bundle size (RBD) when the corner cube size is equal to (a) $100 \mu\text{m}$ and (b) $200 \mu\text{m}$

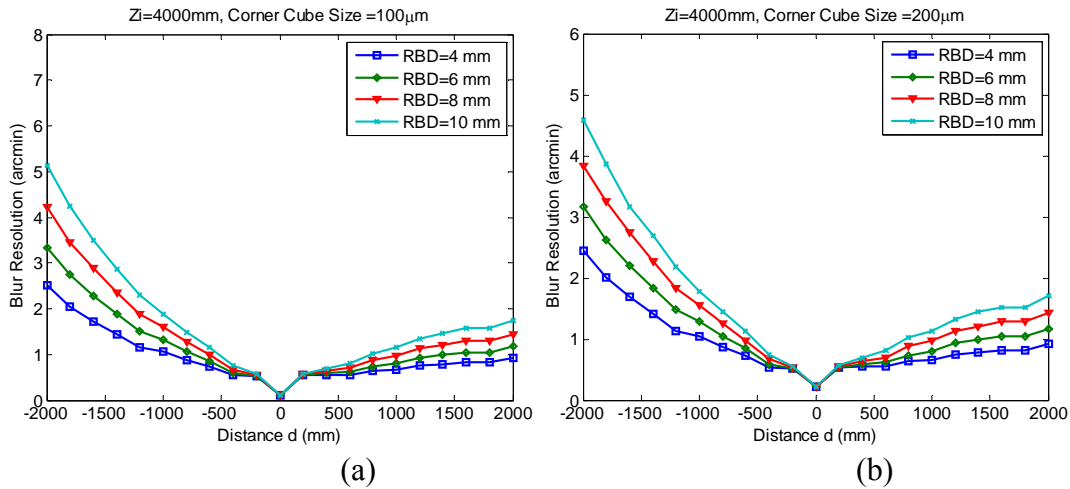


Figure 6.16 Angular resolution at the project image distance z_i of 4m as a function of the distance d and the ray bundle size (RBD) when the corner cube size is equal to (a) $100\mu\text{m}$ and (b) $200\mu\text{m}$

Figure 6.14 (a) and (b) plot the angular resolution at the focusing distance of 1m as a function of distance d and the ray bundle size when the corner cube size is equal to $100\mu\text{m}$ and $200\mu\text{m}$, respectively. Similarly Figure 6.15 (a) and (b) plot the angular resolution at the focusing distance of 2m and Figure 6.16 (a) and (b) plot the angular resolution at the focusing distance of 4m. The results indicate that the angular resolution of the screen degrades with an increase of the distance between the projected image plane and the retroreflective screen. In other words, when other parameters remain constant, the best image resolution is achieved when the projected image plane coincides with the retroreflective screen. With the increase of the ray bundle diameter (RBD) from the projection lens, the blur size increases. For instance, in an arm-length application (i.e. $z_i=1\text{m}$), the angular resolution of a retroreflective screen with the CCR size of $200\mu\text{m}$ can be as large as around 8.6 arc minutes for RBD=4mm when the distance d is -0.7m . Under the same distance d , the results suggest that the blur size increases to 11.6 arcmin for

RBD=10mm. Furthermore, the results suggest that a larger focusing distance z_i helps to reduce the blurring effects when the other parameters are fixed. Thus a p-HMPD user is expected to observe images with more blurring effects in arm-length applications than in far-field applications, which agrees with our experience in the SCAPE visualization system. Figure 6.14, 6.15 and 6.16 further indicate the image resolution of the screen varies with the corner cube size. In the case of $|d|=0$, the angular resolution of the screen degrades with the increase of the cube size due to 180° rotation effect. In the case of $|d|>d_0$, the angular resolution of the screen degrades with the decrease of the cube size due to the diffraction effect.

6.5.3 Tolerance distance in an HMPD

Similar to other head-mounted displays, a motion tracking device is typically attached to an HMPD system, offering a user the ability to walk around in a 3D environment. Under a fixed focusing setting for the projection optics, the distance d between the projection image plane and the retroreflective screen varies depending on the user's location in the environment. Consequently, the image resolution observed by a user depends on his or her physical distance to the screen.

One of the critical parameters to be established is the tolerance range of a user's movement in a 3D environment. Within this range, the image resolution of an HMPD/p-HMPD will not be degraded by the image blur of a retroreflective screen. To establish the range, a rule of thumb which is widely used in the lens design, is used. To avoid the image degradation caused by a retroreflective screen, the angular resolution of

the image blur through the retroreflective screen in a p-HMPD should be smaller than the angular resolution of the display pixel. The tolerance range analysis not only provides an overall evaluation of the display resolution, but also offers guidance to the design of a display environment suitable for a particular application scenario.

Assume the angular resolution subtended by a single pixel of the projection system to be η_0 , which is given by

$$\eta_0 = 2 \arctan\left(\frac{D}{2f}\right) = 2 \arctan\left(\frac{D'}{2z_i}\right), \quad (6.27)$$

where D is the pixel size of the microdisplay, D' is the magnified pixel size through the projection optics, and f is the focal length of the projection lens. The angular resolution of the display pixel in our newly developed p-HMPD prototype is 2.1 arc minutes (Zhang & Hua, 2008). To avoid image degradation caused by a retroreflective screen, the angular resolution of a retroreflective screen in a p-HMPD should be no greater than η_0 .

The tolerance range can be obtained when the angular resolution of the image blur is equal to the display angular resolution. Since the average ray bundle diameter in the current p-HMPD across different directions is approximately 6mm, in an arm-length application (e.g. $z_i=1\text{ m}$), the tolerance range of the user's movement is from -17.8cm to 22.2cm for a p-HMPD with 2.1 arc-minute resolution using a retroreflective screen with the corner cube size of 200 μm . In a mid-range application ($z_i=2\text{ m}$), the tolerance range is from -49.1cm to 90.4cm. In a far-field application, the ranges is from 147.3cm to over 200cm. Realistically, this limitation on user mobility without compromising image resolution is barely acceptable for an interactive 3D environment. Therefore, the imaging

artifacts of a retroreflective screen are the limiting factors for the existing HMPD technology to be adopted for high-resolution 3D display systems.

6.5.4 Optimization of the corner cube size

As shown in Figure 6.14~6.16, the minimum angular resolution can be obtained when $|d|=0$ and the corresponding angular spot size is $\eta = 2 \arctan\left(\frac{a_{eff}}{z_i}\right)$. Meanwhile the image blur increases with the larger CCR size when $d=0$ due to 180° rotation effect while the blur size decreases with the larger CCR size when $|d|>d_0$ due to the diffraction effect. To obtain the maximum tolerance range, the corner cube size should be as large as $z_i \tan\left(\frac{\eta_0}{2}\right)$ so that the image artifact caused by the local 180° rotation effect is as large as the pixel size and meanwhile the diffraction effect is minimized. For example, for our current p-HMPD setup with $z_i=1\text{m}$ and $\eta_0=2.1\text{arcmin}$, the corner cube size can be optimized to be $305\mu\text{m}$ and the improved tolerance range is between -22.6cm and 27.8cm , comparing with the range between -17.8cm to 22.2cm for the corner cube size of $200\mu\text{m}$.

6.6 SUMMARY

In chapter 6, the image properties of a single CCR are studied. The image blur of a retroreflective screen, caused by the geometrical effect and the far field diffraction effect, are characterized. The angular resolution of a retroreflective screen in an HMPD/p-HMPD system as a function of multiple parameters, such as the projected image distance, the corner cube size, the incident ray bundle size and the position of the a

retroreflective screen, is further evaluated using a numerical simulation method. Based on the analysis results, the tolerance range of a user's movement in a 3D environment, within which the image resolution of a p-HMPD may not be degraded by a retroreflective screen, is calculated. To increase the tolerance range, an optimal corner cube size is suggested.

CHAPTER 7

ASSESSMENT OF A P-HMPD SYSTEM

In the design process of a p-HMPD system, it is critical to evaluate the system performance using user-centered assessment protocols. Chapter 7 presents two assessment tests to evaluate a p-HMPD prototype in terms of its perceived spatial resolution and perceived depth rendering accuracy. Both tests employed human-in-the-loop evaluation methods.

7.1 ASSESSMENT OF PERCEIVED SPATIAL RESOLUTION

7.1.1 Introduction

The perceived spatial resolution is an essential performance metrics for a display system. It becomes even more critical for many task-driven demanding applications, such as surgical planning or training, where the capability of resolving high levels of details is required.

Many factors may affect the perceived spatial resolution of a p-HMPD system. First, like other types of HMD systems, the perceived resolution of a p-HMPD system is limited by the native angular resolution of the system, which is determined by the microdisplay resolution, system FOV and spatial resolution of the projection lens. The p-HMPD prototype we developed has a limiting angular resolution of 2.1

arc minutes per pixel. Second, different from conventional eyepiece-based HMDs, the perceived spatial resolution through a p-HMPD is further affected by the imaging properties of a retroreflective screen. As discussed in Chapter 6, a retroreflective screen in a p-HMPD system may cause significant degradation on the spatial resolution of an HMPD or p-HMPD system. The analysis results showed that the image degradation caused by a retroreflective screen varies with the distance between the screen and the projected image plane of the projection system. The image degradation caused by the retroreflective screen is minimized when the screen coincides with the projected image plane. In a typical HMPD system configuration, while the retroreflective screens is placed at fixed locations, the focusing distance of the projection system may be configured to meet different applications. For instance, it is established that the focusing distance of an HMD system should match with the average depth of the rendered 3D scene to limit the well-known convergence-and-accommodation conflicting issue in stereoscopic displays. As a result, the focusing distance should be set to be about 1m for arm-length applications, or to be optical infinity for far-field applications. Therefore, the distance between the screen and the focusing plane not only varies with the user distance to the screens as he or she moves around to explore a 3D environment but also with the focusing setting of the display tailored for specific applications. Finally, the contrast levels of visual stimuli, which may be affected by the surrounding digital contents and the physical objects on which the digital stimuli are superimposed, play significant roles in the resolution performance.

In this section, we evaluated the perceived spatial resolution of an in-house developed p-HMPD prototype using visual acuity metrics. The main factors to be investigated in our study include the contrast levels of visual stimuli and the distance between the retroreflective screen and the focusing plane. Two different stimuli were adopted in the test and two data analysis methods were employed to calculate visual acuity scores.

7.1.2. Related work

Various visual performance tests have been performed for evaluating the performance of visual instruments such as night vision goggles and HMDs. Several of the previous studies with HMD displays reported that the perceived resolution may be lower than the resolution native to the display itself. For instance, the Virtual Environment Performance Assessment Battery (VEPAB) used a Snellen chart for visual acuity measurement in a 3D virtual environment (Lampton, 1994). The test was performed using a Virtual Research Flight Helmet display with a resolution of 238 x 234 pixels and a FOV of 50°x 41° which corresponds to a Snellen score of 20/250. The test reported that the mean Snellen score of 24 users is 20/860. Augmented Reality Performance Assessment Battery (ARPAB) was designed to evaluate the visual acuity of a user's real view through an optical see-through HMD (Kirkley, 2003). A user was asked to look at a Snellen chart in the real environment through different types of AR displays. The results reported that the users' visual acuity drops through the AR displays and the measured Snellen scores varied from 20/30 to 20/40

depending on the AR displays and the corresponding setups.

Few studies have been pursued with HMPD-type systems. Recently, Fidopiastis *et al.* reported a study to evaluate the resolution performance of their in-house built HMPDs under different lighting levels and different contrast levels (Fidopiastis *et al.* 2005). Modified Landolt C was used as the stimuli for visual acuity test. Threshold theory and Probit analysis were employed to evaluate the threshold values of visual acuity. The result showed that the lighting levels did not have significant effects on the visual acuity. The type of the retroreflective screen affected performance at a low contrast level. Different from our study described below, the HMPD system used in their test has a lower resolution of 4.2 arcmin and a smaller FOV of 52°. The effect of the retroreflective screen position, which might be the dominant factors on the perceived image resolution, was not considered in their test.

7.1.3 Experimental design

As discussed earlier, different from conventional eyepiece-based HMDs, the perceived spatial resolution through a p-HMPD is not only affected by the display devices, the optical components and the surrounding environment, but also by the imaging properties and the position of a retroreflective screen. This study aims to account for the combined effects of a retroreflective screen and the projection system on the visual acuity performance through a p-HMPD system. Particularly, we aim to evaluate the perceived resolution of a p-HMPD as a function of the position of a retroreflective screen and image contrast. We further compared the effects of using two different visual

stimuli and two different data analysis methods, which helps to establish guidelines for designing visual performance assessment with HMDs.

7.1.3.1 Visual stimuli design

Visual acuity (VA) metrics, defined as the ability to see fine details, have been commonly adopted for evaluating the resolution performance of visual instruments, while some prior studies have also adopted contrast sensitivity metrics with sine-wave contrast targets for AR display evaluation (Livingston, 2006). The visual stimuli commonly used for display visual acuity assessment include Snellen chart letters and modified Landolt C. Due to the lack of a conclusive guidance on the appropriateness of these two stimuli types for electronic display assessment, we performed tests with both types of visual stimuli for comparison.

Landolt C is adopted as a standard for visual acuity assessment of human visual systems by the National Academy of Sciences (NAS-NRC, 1980). It is a perfectly circular C with varied gap size and orientation. However, when it is applied to generate stimuli on electronic displays with discrete square pixels, it is difficult to generate a circular ring in a 5 x 5 grid without creating significant aliasing effects. To solve this problem, a squared C in a 5x5 grid was designed instead and the corresponding gap was a 1x1 grid (Fidopiastis, *et al.* 2005). Instead of using an eight-alternative forced choice (8AFC) in the standard Landolt C test, a 4AFC was used in the test to avoid aliasing effects. Figure 7.1 shows the revised Landolt C in four different directions.

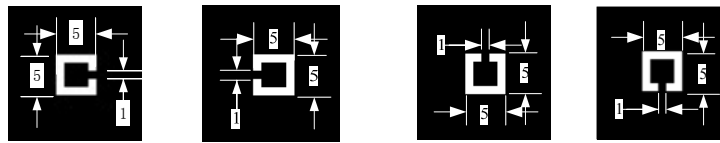


Figure 7.1 Revised Landolt C stimulus in four directions

However, based on a pilot study we performed and previous work in (Pinkus & Task, 1999), the Landolt C test has tendency to give higher resolution results than that of an actual display. A user could possibly make a correct judgment based on a perceived brighter area around the gap even without reliably seeing the C letter. For this reason, we chose to limit the presentation time of each stimuli to 3 seconds and cross-compare its results with a Snellen chart test.

The Snellen chart is the most common type of stimuli for visual acuity test. One major problem with this test is that each letter has different legibility. For example, Letter “L” is easier to recognize than Letter “E”. Both Sloan and British Standard Institution letters have equal legibility and are equivalent to Landolt rings (Ricci, 1998). Sloan Letters include eight 5 x 5 non-serifed letters: S, O, C, D, K, V, R, H, N and Z (Sloan, 1959). British Standard Institution suggests that only C, D, E, F, H, K, N, P, R, U, V, and Z should be used for the testing of vision based upon equal legibility of the letters (BSI, 2003).

Since it is difficult to generate some of the letters in a 5 x 5 grid without causing significant aliasing effects, eight letters from British Standard Institution optotypes were selected for the test and they were letter C, D, E, F, H, K, U, and Z. The letters were generated in a 5 x 5 pixels cell as shown in Figure 7.2, among which letters C, D, K, U and Z were revised to avoid aliasing effect. Although British Standard Institution

optotypes were used in the test, in the following sections they are still referred as Snellen chart letters since the basic idea of this method was the same as the Snellen chart test.

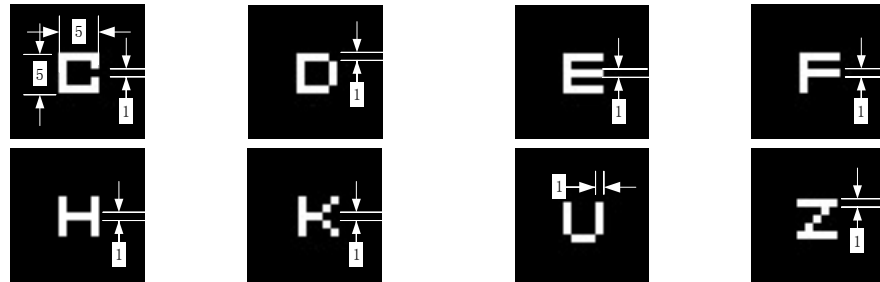


Figure 7.2 Eight revised British Standard Institution optotypes

7.1.3.2 Variables and hypotheses

Two independent variables are considered in the test: position of a retroreflective screen, and stimuli contrast level.

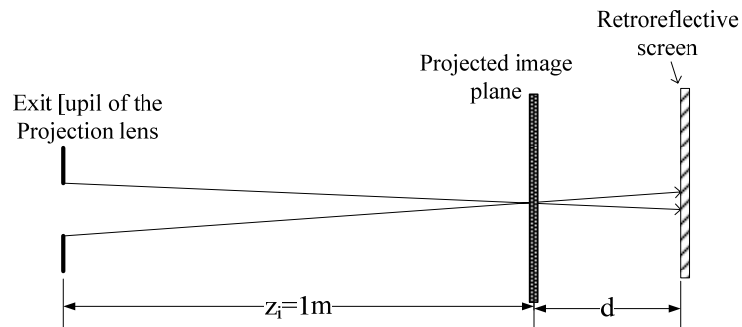


Figure 7.3 Simplified setup of p-HMPD

Position of the retroreflective screen: Figure 7.3 illustrates a simplified view of a p-HMPD setup, where a projection image plane is formed at a distance of z_i from the eye position of a viewer. Based on the theoretical model in Chapter 6, a retroreflective screen has more significant effects in arm-range applications where the projection system is set at a closer focusing distance to the viewer than far-field applications. Therefore, we chose

to set the focusing distance of z_i to be 1m away from the viewer ($z_i=1m$), which corresponds to a working region for an arm-length application. The retroreflective screen is then altered at eight different positions centered around the projection image plane. The distance d is defined as the distance from the projection image plane to the retroreflective screen. Distance d is negative when the screen is closer to the user than the projection image plane and otherwise d is positive. Eight d values are listed in table 7.1, corresponding to eight different positions from p1 to p8. It is worth noting that the selected positions on both sides of the projection image plane are not symmetric because the theoretical model in Chapter 6 predicts that the resolution degradation by a retroreflective screen is more significant when the screen is in front of the projection image plane than when is behind. We hypothesize that a lower VA score which correspond to better perceived resolution would be obtained for a smaller $|d|$ value. The optimal VA through our test is 2.1 arcmin, which is the native resolution of a p-HMPD projection system without accounting for the effects of retroreflective screens.

Table 7.1 Eight positions of the retroreflective screen.

Position	p1	p2	p3	p4	p5	p6	p7	p8
d (cm)	-70	-55	-40	-25	0	35	70	100

Contrast level: The test was performed at two contrast levels with $contrast=1$ and $contrast=0.5$. The contrast is defined by

$$Contrast = \frac{L_{sti} - L_{background}}{L_{sti} + L_{background}} \quad (7.1)$$

where L_{sti} represents the normalized luminance of the stimuli and $L_{background}$ represents the normalized luminance of background. The normalized luminance is obtained through the function $L=(CL/255)^\gamma$ while CL is the command level of the pixels and γ is gamma value of the display, which is 1.41 based on the measurement in chapter 5. As a result, for the contrast of 1, CL equals 255 for the stimuli and CL equals 0 for the background; For the contrast of 0.5, CL equals 208 for the stimuli and equals 95 for background. We expect a lower VA score which corresponds to better VA for higher contrast target. The main reason for introducing the contrast variable is to gage the display performance at a lower contrast level. Another benefit is to increase the range of VA scores for better analysis on the effects of retroreflective screen position and stimuli types.

Other parameters: For each contrast level, the stimuli are presented at three different levels of resolution. To produce three different resolution levels, i.e. 2.1 arcmin, 4.2 arcmin and 6.3 arcmin, a unit grid in the stimuli would be composed of 1x1 pixel, 2x2 pixels, and 3x3 pixels, respectively.

The tests were repeated with both Landolt C and Snellen chart stimuli. At each resolution level, there were four random repetitions for each gap orientation for the Landolt C test, while there were two random repetitions of the same letter for the Snellen chart test. Both tests had a total number of 16 trials per level of resolution per contrast level per position of the retroreflective screen. The total trials of the experiment for each subject would be 16 trials x 3 resolutions x 2 contrast levels x 8 positions x 2 stimuli = 1536 trials.

7.1.3.3 Subject

Eight subjects between the age of 21 and 38 participated in the test. To avoid effects potentially introduced by the slight differences of the p-HMPD optics for the right and left eyes, only the right eye was tested. Screened by a Snellen chart test in the lab, the right eyes of all subjects had normal or correct-to-normal visual acuity. No one has taken LASIK eye surgery. All subjects received \$10/hour compensation for their time.

7.1.3.4 Experiment procedure

Each participant took two sessions of tests using the different test stimuli: Session I for the Landolt C and Session II for the Snellen letters. Four subjects were randomly selected to start with the session I and the other four started with Session II. For each trial, a Landolt C or a Snellen letter was presented at the center of the field of view through the right-arm optics of a p-HMPD. The participant was asked to verbally tell the experimenter the direction if the Landolt C was used or to read the letter if the Snellen chart was used. The experimenter recorded the answers into a computer log file. Each stimulus was presented for 3 sec before a blank screen at the same gray level as the background of the stimuli was shown. No time limit was set for the participant to respond. In other words, a user could either make a judgment within 3 sec or take longer time. A user was required to make a response to each stimulus to move to the next stimulus and thus the blind guess was allowed.

7.1.3.5 Experiment setup

The experiment was performed on an optical bench. To stabilize the eye position of a viewer to the display, a p-HMPD prototype was fixed at the edge of the optical bench and a user fits his/her head into the p-HMPD prototype to view the displayed stimuli. A retroreflective screen with the size of 1 meter by 1 meter can be moved accurately on an optical rail along the z direction. Around the optical table, black curtains formed an enclosed space and the experiment was performed in the dark enclosed environment to avoid the disturbance by stray lights. Before the test, the focusing distance of the p-HMPD was calibrated to be 1 meter and the colorimetric calibration was also performed using the method described in chapter 5.

7.1.3.6 Scoring method

For every 16 trials per contrast level per resolution level per position of the retroreflective screen, the percent of correct trials p can be obtained. Since the blind guess was allowed in the test, chance alone would result in 25% of correct answers for Landolt C test and 12.5% correct answers for Snellen chart test. The percent of correct trials adjusted for chance, p_r , is given by

$$p_r = \frac{4 \times (p - 0.25)}{3} \quad (p_r = 0 \text{ if } p < 0.25) \quad \text{for Landolt C test}$$

and

$$p_r = \frac{8 \times (p - 0.125)}{7} \quad (p_r = 0 \text{ if } p < 0.125) \quad \text{for Snellen chart letter.}$$

The visual acuity scores can be calculated either using “threshold curve” or “letter-by-letter” visual acuity scoring methods. Both methods are commonly used for the

visual acuity test with an eye chart (Arditi & Caganello, 1993). We explored and compared the two methods to provide guidelines on the data analysis method for future HMD tests.

A threshold curve method is based on the psychometric functions which represent the relationship between the user's visual capability and the levels of resolution. In our test, Probit analysis was used to fit the psychometric function which is a smooth s-curve through the test data. The percent of correct trials adjusted for chance was converted to normal equivalent deviates (NED). An NED is the value of a standard normal variable whose cumulative probability equals the percent adjusted for chance. Since NED can't be calculated for $p_r=0$ or $p_r=1$, p_r is set to be 1% or 99% correspondingly (Pinkus & Task, 1998). The NED values were used as the dependent variable in a linear regression with visual acuity as independent variable. A linear relationship between NED and VA, $NED = b_0 + b_1 \times VA$, can be established. The VA score corresponding to 50% percent correct trials adjusted for chance is the threshold visual acuity score, which can be obtained using linear interpolation method (Finney, 1980).

In a letter-by-letter scoring method, all visual acuity levels were converted to the logMAR format by taking the \log_{10} of the visual acuity data. For example, when the gap of Landolt C is 1 pixel size which corresponds to an angular resolution of 2.1 arcmin, the resolution is equivalent to 0.322 ($\log_{10}2.1$) in the logMAR unit .

An interpolated logMAR acuity score can be obtained for both stimuli using the equation

$$VA_{LogMAR} = \log_{10}(8.4) - \sum_{c=1}^3 p_r(c)L_c, \quad (7.2)$$

where $p_r(c)$ is the percent of correct trials adjusted for chance at the resolution level c and L_c is the difference of logMAR values between the resolution level c and the resolution level $c+1$. The constant $\log(8.4)$ is a bias term and is the VA score if none of the letter at different resolutions is correctly identified. The corresponding L_c values for the three resolution levels, i.e. 2.1arcmin, 4.2arcmin and 6.3arcmin, are $\log(4.2)-\log(2.1)$, $\log(6.3)-\log(4.2)$ and $\log(8.4)-\log(6.3)$, respectively. Based on the VA_{logMAR} , the letter-by-letter VA score can be calculated in a unit of arcmin through the equation

$$VA = 10^{VA_{logMAR}}. \quad (7.3)$$

VA scores obtained from threshold method and letter-by-letter method describe the resolvability of a user through a p-HMPD. A lower VA score corresponds to better visual acuity.

7.1.4 Results and discussion

The mean value and the standard deviation (SD) of VA scores obtained from eight participants are listed in the Table 7.2, in which p1 to p8 represent the eight different positions of the retroreflective screen defined in Table 7.1. Fig 7.4 (a) and (b) plot the mean VA scores at different contrast levels using threshold curve method and Fig 7.5 (a) and (b) plot the results using letter-by-letter method.

Table 7.2 Mean and standard deviation (SD) of visual acuity scores obtained from eight participants (the unit is in arcmin).

		Positions of RR screen		p1	p2	p3	p4	p5	p6	p7	p8
Threshold curve	Landolt C	Contrast=1	Mean	2.957	2.185	2.122	2.100	2.100	2.257	2.457	2.711
			SD	0.360	0.118	0.058	0.000	0.000	0.283	0.401	0.520
		Contrast=0.5	Mean	4.229	2.640	2.100	2.100	2.100	2.571	3.165	3.354
			SD	0.886	0.460	0.000	0.000	0.000	0.718	0.641	0.581
	Snellen	Contrast=1	Mean	2.863	2.218	2.100	2.100	2.100	2.183	2.271	2.529
			SD	0.244	0.207	0.000	0.000	0.000	0.218	0.218	0.446
		Contrast=0.5	Mean	3.644	2.705	2.187	2.100	2.100	2.299	2.903	3.385
			SD	0.672	0.392	0.154	0.000	0.000	0.417	0.593	0.399
		Positions of RR screen		p1	p2	p3	p4	p5	p6	p7	p8
Letter by Letter	Landolt C	Contrast=1	Mean	3.950	2.862	2.434	2.116	2.100	2.724	3.242	3.495
			SD	0.373	0.323	0.361	0.041	0.000	0.678	0.523	0.561
		Contrast=0.5	Mean	5.091	3.570	2.401	2.165	2.165	3.244	3.881	4.224
			SD	0.868	0.534	0.216	0.132	0.132	0.771	0.492	0.601
	Snellen	Contrast=1	Mean	3.771	2.881	2.154	2.100	2.100	2.537	2.909	3.320
			SD	0.243	0.460	0.077	0.000	0.000	0.496	0.523	0.584
		Contrast=0.5	Mean	4.534	3.628	2.512	2.169	2.174	2.921	3.846	4.324
			SD	0.599	0.404	0.504	0.111	0.195	0.649	0.611	0.372

As shown in Figure 7.4 and Figure 7.5, VA scores based on the threshold curve method are generally lower than the results based on the letter-by-letter method. The results were expected since the letter-by-letter method is more strict in the scoring. For example, to get 2.1 arcmin VA score, a user is required to provide 100% of correct answer in the letter-by-letter analysis method while only 50% of correct answers are needed using threshold curve method.

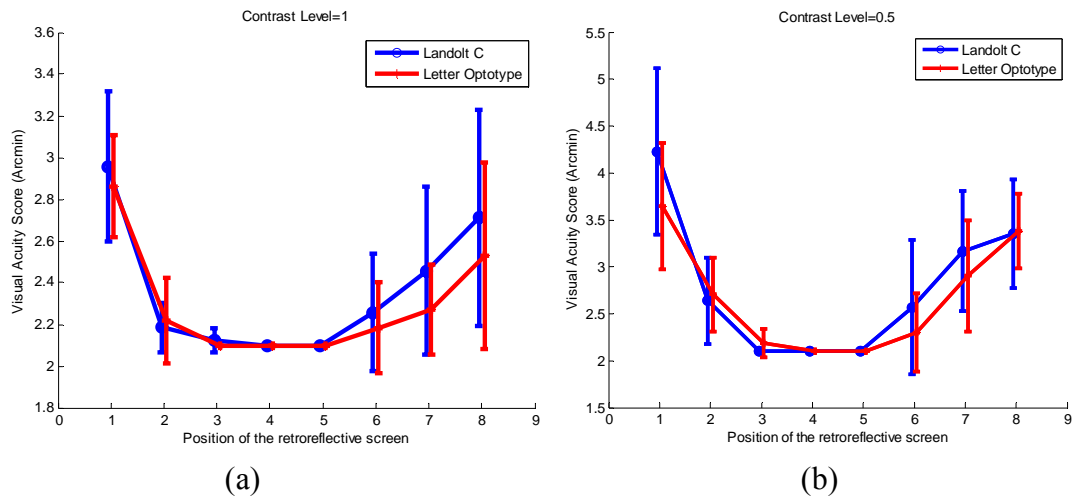


Figure 7.4 Mean VA scores at (a) the contrast of 1 and (b) the contrast of 0.5 using the threshold curve method

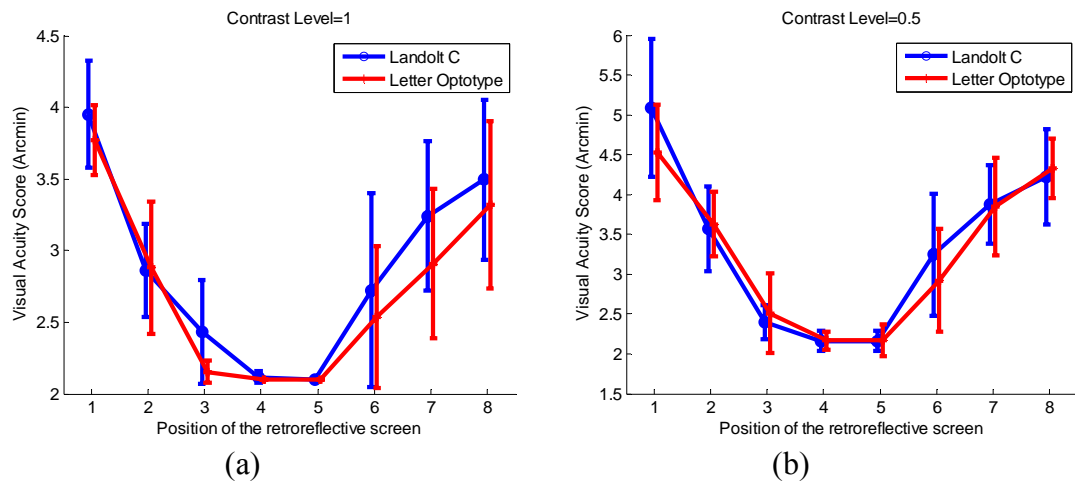


Figure 7.5 Mean VA scores at (a) the contrast of 1 and (b) the contrast of 0.5 using the letter-by-letter method

Our further data analysis started with evaluating the effectiveness of the threshold curve method. The Tukey grouping test was used to evaluate if any position groups were not significantly different using the threshold curve method. The results show that the VA scores for the position 2, 3, 4, 5, 6, 7 were not significantly different, which did not agree with our model prediction in Chapter 6 and our experiences that significant differences

through a p-HMPD have been observed between position 2 and position 5.

Further analysis of the test results shows that the threshold curve method is not an effective method to evaluate the VA performance of the display under test. For example, as shown in Figure 7.6, a participant got 56.25% correct response at position 3 and got 80.21% correct response for position 2 at the resolution level of 2.1 arcmin. The same participant also got 100% correct response for both positions at the resolution of 4.2 arcmin. If the threshold curve method was used, although position 3 and position 2 had different effects on the user's visual acuity, the VA scores at both positions are 2.1 arcmin, since the percent of correct response for both positions are higher than 50%. The method is unable to provide effective results that indicate the difference between the two positions.

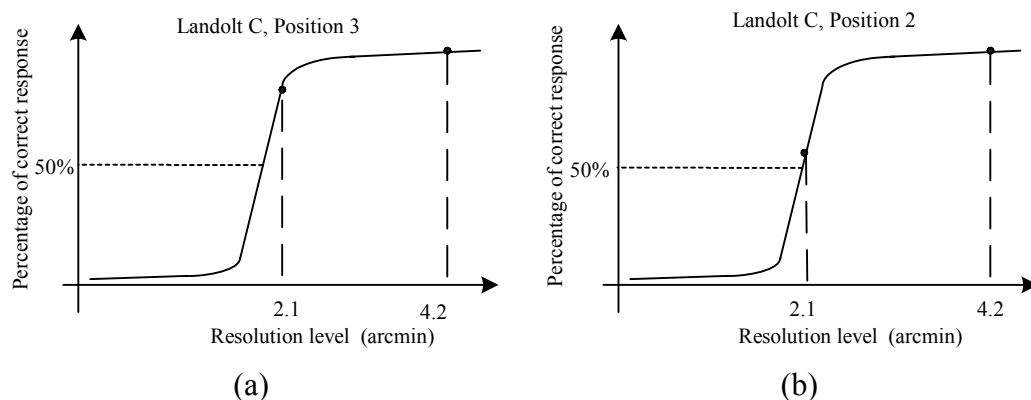


Figure 7.6 Results of the threshold curve method for positions 3 and 2.

In order to make the threshold curve method effective, the following requirement should be met. At least two data points should be distributed on the linear part of the S curve. One data point should have less than 50% correct response and another point should have more than 50% correct response. In the current p-HMPD prototype, however,

the main limiting factor of the system is the resolution of the displays, especially when the retroreflective screen locates at p3, p4, p5 and p6. The percent of correct response is generally higher than 50% at the resolution level of 2.1 arcmin. Meanwhile, the step size between two resolution levels is 2.1 arcmin, which is too large to obtain at least two points at the linear part of S curve. As a result, only one or less data point distributes on the linear part of the S curve. Therefore, we conclude that the threshold-curve method is inadequate for the VA test of the p-HMPD and other resolution-limited electronic displays in general.

In the following part, only the results based on the letter-by-letter method are further analyzed. As shown in Table 7.2, the lowest VA scores are obtained when the retroreflective screen locates at position 5 and position 4 for both contrast levels and for both types of stimuli. The mean VA values increase when the retroreflective screen is away from the position 5 which is also the position of the projected image plane. Moreover, the degradation of the VA scores is more significant when a retroreflective screen is placed closer to the user than the projection image plane (i.e. negative d values). These results agree with our theoretical analysis on Chapter 6.

A within subject ANOVA was used to analyze the VA scores. The ANOVA results showed that the two types of visual stimuli have only marginal effect on the VA scores ($F(1,7)=5.17$, $p=0.057$). The VA scores produced by Landolt C are slightly higher than those by Snellen letters. Both methods might be considered as being equivalent for evaluating the resolution performance of HMDs. The 3 seconds limitation of the stimuli presentation time may help to improve the reliability of the Landolt C stimuli. The

ANOVA showed that the contrast levels had a significant effect on the VA scores ($F(1, 7) = 139.65, p < .0001$). The ANOVA also showed that the position of the retroreflective screen had a significant effect on the VA scores ($F(7, 49) = 45.55, p < .0001$). These results agreed with our theoretical analysis.

The Tukey grouping test was used to evaluate if the results at any position groups are not significantly different. Tukey grouping test was performed at two different contrast levels respectively and the results are shown in Table 7.3.

Table 7.3 Tukey Grouping results for (a) contrast=1 and (b) contrast=0.5

(a)					(b)				
Tukey Grouping		Mean	N	Distance	Tukey Grouping		Mean	N	Distance
	A	3.8608	16	1		A	4.8126	16	1
	A					A			
B	A	3.4072	16	8	B	A	4.2745	16	8
B					B				
B	C	3.0755	16	7	B	C	3.8638	16	7
B	C				B	C			
B	C	2.8717	16	2	D	C	3.5989	16	2
	C				D				
D	C	2.6304	16	6	D	E	3.0829	16	6
D					D	E			
D		2.2939	16	3	F	E	2.4564	16	3
D					F				
D		2.1078	16	4	F		2.1695	16	5
D					F				
D		2.1000	16	5	F		2.1670	16	4
					F				

Although we would not get clear conclusion on the grouping of the different positions due to the overlapping of multiple groups, we were still able to figure out the groups which did not show significantly different results with position 5. As shown in Table 7.3, when contrast =1, position 3, 4, 5, 6 is formed as a group. The results indicate that the VA scores of the display are not significantly degraded when the screen position varies from -40cm to 35cm relative to the focusing plane. When contrast=0.5, position 3, 4, 5 are formed as a group which corresponds to the screen position from -40cm to 0cm relative to focusing plane. Position 6, corresponding to the distance of 35cm, is not in the

group. Since the image luminance is lower when the retroreflective screen is further away due to the diffraction effect, it is reasonable to say that the VA scores can be affected more at lower contrast level when the retroreflective screen is further away.

Interaction between contrast levels and positions of retroreflective screen was also studied using a within-subject ANOVA. The contrast levels and positions of the retroreflective screen significantly interact with each other ($F(7, 49) = 8.29, p < 0.0001$). The result indicated that the effects of contrast levels were different for different screen positions. The effect of contrast levels was more significant for the position away from the focusing plane than the positions closer to the focusing plane. At the focusing plane, i.e. p5, the display resolution is the limiting factor of the visual capability through a p-HMPD and the VA score is barely affected by the contrast levels. However, at a position that is away from the focusing plane, the resolution degradation caused by the retroreflective screen becomes the limiting factor and the VA scores can be easily affected by contrast levels due to the shift of the threshold MTF frequencies.

The interaction between contrast levels and stimuli was not significant ($F(1, 7) = 0.59, p = 0.4681$). The interaction between stimuli and positions of retroreflective screen was not significant ($F(7, 49) = 1.11, p = 0.3696$).

7.1.5 Summary

We used visual acuity metrics to evaluate the spatial resolution performance of an in-house built p-HMPD prototype. Both Landolt C and Snellen chart letters were used as the stimuli in the test. Two data processing methods were employed to calculate VA

scores. Through the analysis of test results, we suggest to use a letter-by-letter scoring method in the future test especially when the display resolution is the limiting factor of the image resolution. The results also indicated that there is no significant difference between Landolt C and Snellen chart letters. Both contrast levels and the positions of the retroreflective screen, as we expected, had significant effects on VA scores. The p-HMPD has a lower VA score which corresponds to better VA when the retroreflective screen is close to the focusing plane and the VA is getting worse when the retroreflective screen is away from the focusing plane, which agrees with our theoretical analysis presented in Chapter 6.

7.2 DEPTH PERCEPTION ASSESSMENT

7.2.1 Introduction

OST-HMDs have been explored extensively for AR applications and examples include scientific visualization, medical training and surgery planning. It is an essential goal in AR applications using OST-HMDs that users perceive the depth and spatial layout of both virtual and real objects in a way which conforms to the predictive model. The error in the depth judgment could lead to the failure of AR tasks, especially in medical applications which may require high depth perception accuracy. This section characterizes the accuracy of the depth judgment through a p-HMPD.

Several prior efforts investigated the depth perception judgment accuracy in AR environment employing conventional eyepiece-based OST-HMDs (Kirkley, 2003, Swan, *et al.* 2007; Jones, *et al.* 2008). Different from the conventional eyepiece-based

OST-HMDs, a retroreflective screen, which is a unique part in the HMPD systems, brings more complexity in the process of depth perception. A user's depth perception through an HMPD could be affected by the following factors. First, a user perceives the projected image through a retroreflective screen and the existence of a retroreflective screen introduces an extra depth cue, which may affect the depth perception judgment. Second, in a typical AR application setting, a user, wearing an HMPD, may constantly move around or may manipulate the position of a virtual object to gain different viewing perspective of a 3D scene. As a result, the distances among the projected image plane, the rendered object plane, and the retroreflective screen, can be constantly changed. The effect caused by the presence of a retroreflective screen on the depth perception may depend on such dynamic changes. Third, based on the study in Chapter 6 and the test results in Chapter 7.1, the image resolution of a p-HMPD is affected by the position of a retroreflective screen, which may further affect a user's depth judgment. Therefore, it is necessary to evaluate how these factors may affect an HMPD user's depth perception and provide guidance for the application development.

This section will start with a more detailed analysis on the various factors that may affect depth perception accuracy, followed by reporting the design and results of a depth perception assessment test using an in-house developed p-HMPD prototype. The main factors to be evaluated include the depth judgment accuracy at different viewing distances and the effect of the retroreflective screen on the depth judgment.

7.2.2 Contributing factors to depth perception accuracy

Many factors may affect a user's depth perception accuracy through a stereoscopic display, including conflicting or missing depth cues, stereoacuity, display resolution, and interpupillary distance (IPD). This section focuses on reviewing the effects of these factors on the depth perception accuracy.

7.2.2.1 Depth cues

The human visual system relies on multiple cues to make a depth judgment. The most commonly cited depth cues are binocular disparity, convergence, accommodation, occlusion, motion parallax, aerial perspective, relative size, height in the visual field, linear perspective, shading and texture gradient (Cutting, 1997). The significance of different cues varied depending on the viewing distance of the object. For the viewing distance smaller than 1.5m, the most important cues, which are listed in the order of significance, are occlusion, binocular disparity, relative size, convergence and accommodation. For the viewing distance between 1.5m and 30m, the most important cues are occlusion, height in the visual field, binocular disparity, motion perspective and relative size.

Each depth cue provides a certain amount of information for depth perception. In the real world, the eye may combine some or all of these depth cues and the depth judgment can be made in a consistent way. In an AR environment, the inconsistency and inaccuracy of the depth perception may rise with missing or conflict of certain depth cues. For instance, in an HMPD system, the virtual image is perceived through a retroreflective screen and the image plane typically does not coincide with the screen location as a user

may move. The physical presence of the screen may introduce a conflicting depth cue especially when a virtual object is rendered to appear behind the screen (here the perception that a physical screen does not occlude an object appearing behind is contradictory to a natural perception).

It is generally very challenging to separate and quantify the contribution of each involved depth cue to a user's depth judgment, especially when conflicting cues are present. The combined effects of the depth cues rendered through a display system can be more effectively evaluated through user assessment experiments.

7.2.2.2 Stereoacuity

Like most binocular OST-HMDs, perhaps binocular disparity cue is the most salient depth cue in a p-HMPD and it is commonly defined by the angular disparity which is the difference between the vergence angles of the eyes at the point of fixation and the object of interest. The stereoacuity characterizes the smallest, perceptible angular disparity between two 3D objects separated in depth. It varies from 1.8 seconds of arc to 120 seconds of arc among different users. The value of 30 seconds of arc is considered as a typical value for stereoacuity threshold. The corresponding discernable depth, Δz_p , is given by

$$\Delta z_p = \frac{z_p^2}{IPD} \eta \quad (7.4)$$

where z_p is the viewing distance of a 3D object, η is the stereoacuity threshold angle, and IPD is the interpupillary distance of the observer (Howard & Rogers, 1995). For instance,

assuming an IPD of 65mm and visual acuity of 30arcmin, the smallest discernable depth is around 2.2mm for a viewing distance of 1m, while 35.8mm for a viewing distance of 4 meters.

7.2.2.3 Display pixel resolution

Display pixel resolution plays a significant role in the depth rendering accuracy of a 3D display system. As displays are discretized into pixels, the smallest angular disparity that can be rendered is limited by the pixel size. As shown in Figure 7.7, to render a 3D point P_0 , the projected points on the image plane P_L for the left eye and P_R for the right eye need to be rounded-up to the nearest pixels which can be slightly different from their ideal projection points due to the limited resolution of the display. The round-up error can be up to 1 pixel and as a result the perceived point can be point P_i instead. The amount of depth errors caused by the display pixellation is given by,

$$\Delta z_p = \frac{z_p^2}{IPD} \eta_0 \quad (7.5)$$

where η_0 is the effective angular resolution subtended by a single pixel of the display. In our p-HMPD prototype to be tested, the angular resolution per pixel on the microdisplay is 2.1 arc minutes. However, as modeled in chapter 6, a retroreflective screen introduces additional degradation to the pixel resolution of an HMPD system and the level of degradation varies with the distance between the retroreflective screen and the focusing plane. As a result, the position of a retroreflective screen could potentially affect the depth rendering accuracy of an HMPD system and therefore depth judgment.

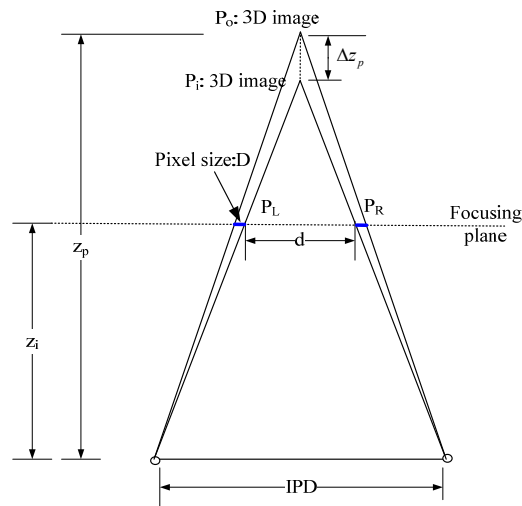


Figure 7.7 Depth perception error caused by pixel resolution

7.2.2.4 IPD mismatch

Depth perception accuracy is further affected by the difference among the IPD of a display setup, the IPD of the computational model used to render the projection points, and the IPD of a viewer. Any mismatch among the three IPD values causes depth perception errors. Here we assume that a careful calibration procedure can be done (See Chapter 5) to ensure that the IPD of a display setup matches with the IPD in the computational model. We mainly examine the effects when there is a mismatch between the IPD of the display and the viewer's IPD. As shown in Figure 7.8, a 3D image point P is generated by fusing the point P_L observed by the left eye and the point P_R observed by the right eye. Here IPD refers to the actual IPD of a binocular display while IPD' is a user's IPD. Due to the IPD mismatch, the perceived 3D point shifts from point P to P' . The shift distance, which is the error of depth perception, can be calculated by

$$\Delta z_p = -\frac{z_p(z_p - z_i)}{IPD \cdot z_i} \cdot \Delta IPD \quad (7.6)$$

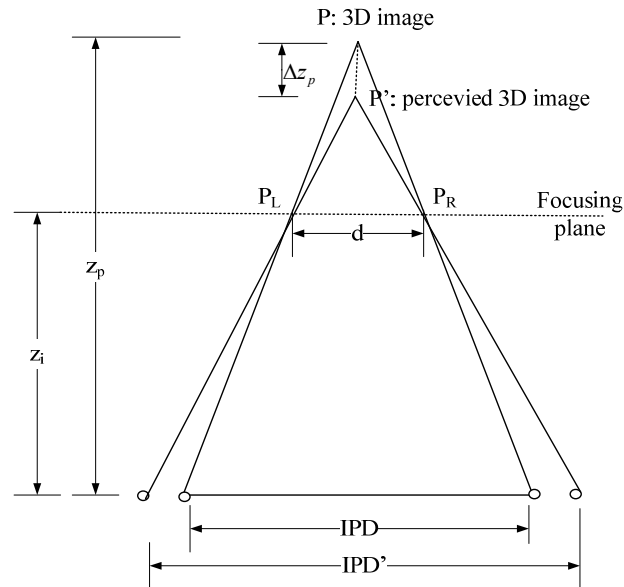


Figure 7.8 Depth perception error caused by IPD mismatch

To further demonstrate the effects of stereoacuity, display resolution, and IPD mismatch, Figure 7.9 plots the depth perception errors caused by these factors as a function of the 3D point distance z_p from 0.4m to 3.2m. The IPD of the display is set to be 65mm, ΔIPD is 1mm, η_0 is 2.1arcmin and η is 30 arcsec. Since the error caused by IPD mismatch varies with the focusing plane distance z_i , Figure 7.9 plots the errors of IPD mismatch for $z_i=1m$ with z_p varying from 0.4m to 1.6m and for $z_i=2m$ and with z_p varying from 0.8m to 3.2m. Here the range of z_p in the plot is the movement range of the reference object in the test described later. The plots suggest that the error caused by the pixel resolution dominates the perceived depth error, especially when the object distance is further. It is worth noting that the plots only show the perceived depth error for the

worst scenario.

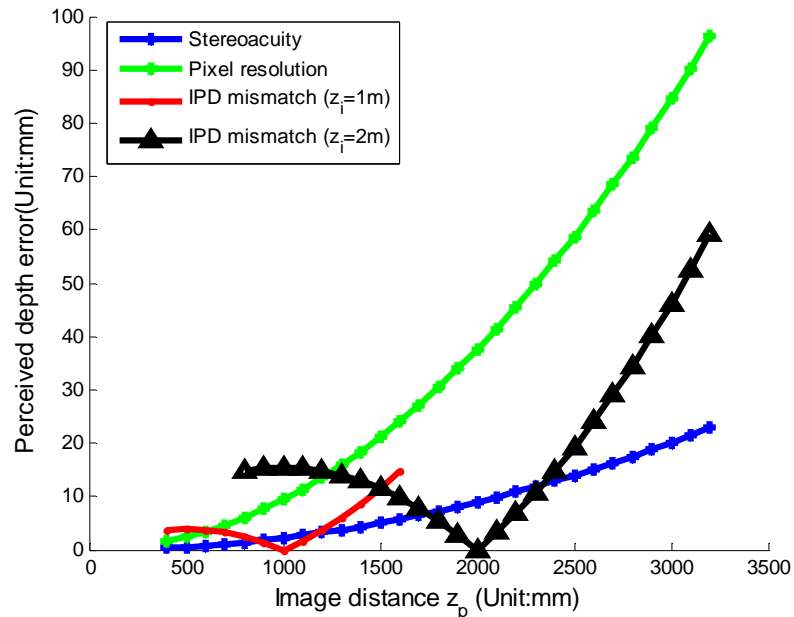


Figure 7.9 Perceived depth errors related with binocular disparity

7.2.3 Depth perception assessment methods

Three methods, including verbal report method, walking methods and perceptual matching method (Swan *et al.* 2007), are commonly used to measure the perceived depth or the judged egocentric distance of a visual stimuli, which refers the distance measured from the user's point of view. In the verbal report method, subjects are asked to estimate the perceived distance of a visual stimuli verbally using the units they are familiar with, such as meters, feet, centimeters and inches (Kirkley, 2003; Swan *et al.* 2007). The results from the verbal reports tend to be noisy and usually are subject to a variety of biases. Walking methods perhaps are the most commonly used methods. There are different forms of walking methods. One form of the method is called direct walking

method (Loomis & Knapp, 2003; Swan *et al.* 2007; Jones *et al.* 2008). A virtual object at a certain distance is presented to a subject for a short-time duration and the subject with the eyes covered is asked to walk to the object position directly. The walking distance is taken as the judged egocentric distance. The method turns out to be quite accurate for the distance range within 30 meters. Other forms of walking methods include triangulated walking, treadmill walking method and imaged visually directed walking (Thompson *et al.* 2004; Witmer & Sadowski, 1998; Plumert *et al.* 2004). In the perceptual matching method, a subject is asked to move the position of a target object so the position of the target object is perceptually matched with a reference object (Swan *et al.* 2006, Rolland *et al.* 1995; Swan *et al.* 2007; Ellis & Menges, 1998). The method tends to be effective and accurate for a relatively short-range application compared with the various walking methods.

The methods discussed above have been applied by several researchers to explore the depth judgment in an AR environment using eyepiece-based OST-HMDs. Rolland *et al.* evaluated the depth judgment for both virtual and real objects at distances of 0.8m and 1.2m using a two-alternative-forced-choice (2AFC) method, which is a revised version of the perceptual matching method. Results were reported that the depth of a virtual object was overestimated in comparison with a real object (Rolland *et al.* 1995). Ellis and Menges examined the depth judgment errors of virtual objects as a function of viewing conditions and scene content using a perceptual matching method for the distance from 0.4m to 1.0m (Ellis & Menges, 1998). The effect of the presentation mode of the virtual objects, accommodation, participants' age, and the position of physical surfaces were

examined. In the AR performance assessment battery designed by Kirkley, the verbal report method was used to study depth judgment under the effects of environmental cues and the level of the objects (Kirkley, 2003). A large object pool was used in the test including 2D/3D geometrical virtual objects, 3D virtual objects with texture and real objects. Swan *et al.* used the perceptual matching method to study the depth judgment for the distances from 5.25m to 44.31m. The effect of the x-ray vision and the effect of display FOV were studied in the test (Swan, *et al.* 2006). Swan *et al.* further studied the depth judgment using verbal report and blind walking method for the distances between 3m and 7m in four different environments. The results showed that blind walking method provided more accurate and consistent results (Swan, *et al.* 2007). Jerome and Witmer evaluated the depth judgment using a verbal report method and a perceptual matching method and they found the perceptual matching method provided more accurate results comparing with verbal report method.

7.2.4 Experiment design

7.2.4.1 Experiment task

The perceptual matching method discussed in Section 7.2.3 was adopted in our test considering different factors, such as distance range of the test, the space limitation and the accuracy of the method. For each trial, a virtual object, which is a gray sphere, was rendered at a randomly selected distance with a specific range contingent to the focusing distance of the display. A real reference object, which is a white cylinder, was moved to a target position by the experimenter. The user was asked to move the virtual sphere using a keypad interface until its perceived depth matches that of the real object. There was no

time limit in the depth matching process. The sphere could be moved further away by pressing “9” and “7” in the number keypad and could be moved closer by pressing “1” and “3”. “7” and “1” were used for a coarse movement which corresponds to 10cm per step while “9” and “3” were used for a fine adjustment which corresponds to 0.5cm per step. Participants could press the middle button of the mouse to finalize the depth judgment and to initial a new trial. The egocentric distance of the virtual sphere, which was the z coordinate of the sphere, was recorded as the judged distance. The judged distances were saved in a log file.

7.2.4.2 Variables

As discussed in the Chapter 6, the focusing distance z_i is typically set to match the requirements of an application in order to minimize viewing discomfort and to minimize stereo fusion difficulty caused by the accommodation-convergence depth discrepancy plaguing most existing stereoscopic displays. For this test, we focus on evaluating the depth perception accuracy in the arm-length range, corresponding to workbench-type applications and surgical visualization, and the mid-range, corresponding to immersive walk-through applications (Hua, *et al.* 2004). Correspondingly, the depth perception assessment was performed at two different focusing distances, with $z_i=1\text{m}$ and $z_i=2\text{m}$.

For both focusing settings, two independent variables were considered in the test: position of retroreflective screen, and reference object distance.

Position of retroreflective screen: The use of a retroreflective screen makes HMPD unique from other types of HMDs and the presence of the screen may affect a user’s

depth perception. Moreover, based on the study in chapter 6, the effective image resolution of the display degrades with the increase of the distance between the retroreflective screen and the focusing distance. In the test, for each display focusing distance, the retroreflective screen was placed at three different locations—one position overlapped with the focusing plane while the other two positions were in front of and behind the focusing image plane, respectively. The distance between the observer and retroreflective screen for the two different focusing distances are indicated in the Figure 7.10(a) and (b), respectively.

Reference object distance: The reference object distance was defined as the egocentric distance of the real object. The range of the reference object distance was tailored for each focusing setting. When the display was focused at 1m, the reference object was placed between 0.4m to 1.6m while for focusing distance of 2m the range was from 0.8m to 3.2m. In each display focusing setting and each screen location, the reference object was placed at seven different positions around the focusing plane, one coinciding with the focusing plane, three in front and three after the focusing plane. The placements of the reference objects are illustrated in Figure 7.10(a) and (b). At each real object distance, five repetitions would be performed.

In summary, with seven reference object distances and five repetitions, there were a total of 35 trials for each screen position. For each display focusing setting, there were a total of 3 (positions of the reflective screen) x 7 (reference object positions) x 5 (repetitions) = 105 trials. Each subject would perform a total of 210 trials.

There are three dependent variables, including the judged distance, the signed error

and distance ratio, while signed error and distance ratio are given by the following equations

Signed error= judged distance-actual distance

Distance ratio= judged distance/actual distance.

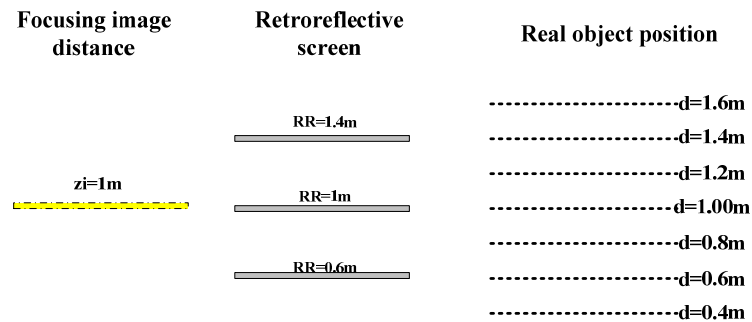


Figure 7.10(a). Test session 1 for arm length setup

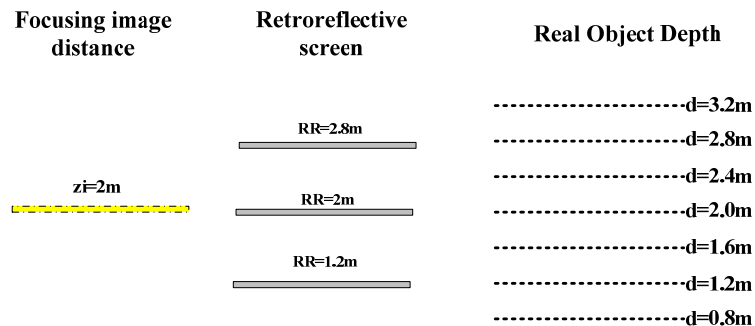


Figure 7.10(b). Test session 2 for mid-range setup

7.2.4.3 Experiment setup

The experiment was performed on an optical bench. As shown in Figure 7.11(a), the p-HMPD helmet was fixed on the optical table to avoid the head movement. As shown in Figure 7.11(b), a retroreflective screen was set to be above the real object so that the screen would not block the real object even when the real object was behind the screen.

Meanwhile we also ensure the user is able to see the whole virtual object through the retroreflective screen. Previous research suggests that the perceived depth of the points on an apparent Fronto-parallel plane varies with the horizontal FOV (Foley, 1991). To make the perceptual matching method more accurate, both the virtual and real objects were placed at the center of the horizontal FOV and the virtual object was on the top of the real object.

To obtain better accuracy of the depth judgment, it was suggested that the size of objects being small (Rolland & Arthur, 1997). The diameter of the real object, which is a white cylinder, is 25mm for $z_i=1\text{m}$ and 50mm for $z_i=2\text{m}$, to ensure that they appear to be similar size. In each trial, a virtual sphere was rendered at a random position within the range of the real object distance so that a user's judgment will not be affected by the last trial. To avoid that users make the depth judgment by directly comparing the relative size of a virtual object and a real object, the diameter of the virtual sphere varied from 20mm to 32mm for $z_i=1\text{m}$ and varied from 40mm to 64mm for $z_i=2\text{m}$ in different trials.

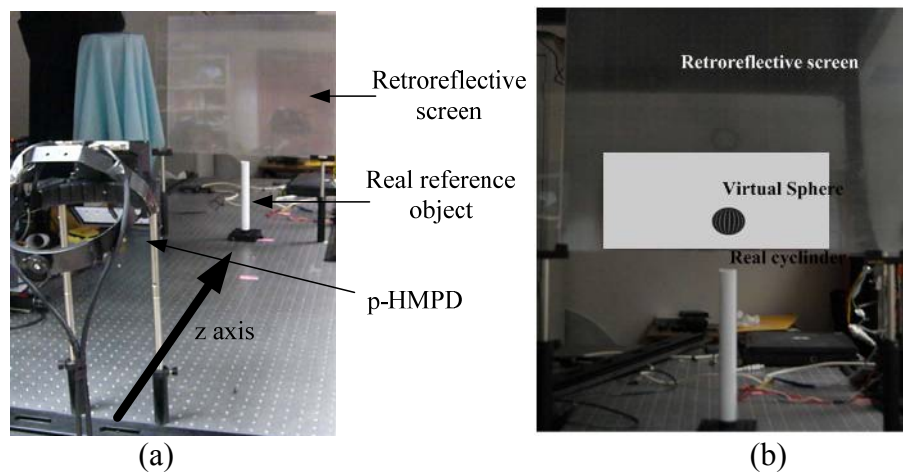


Figure 7.11 (a) Experiment setup and (b) Example view through one side of the display: a virtual sphere and a real cylinder

The vertical distance, which is defined as the distance from the center of the virtual sphere to the top surface of the real cylinder is approximately a fixed value. The distance was 40mm for $z_i=1\text{m}$ and was 80mm for $z_i=2\text{m}$.

7.2.4.4 System calibration

The IPD of the p-HMPD prototype under test needs to be adjusted for each subject to minimize depth rendering errors caused by IPD mismatch. A careful calibration of the display is required after each adjustment. Chapter 5 summarized the calibration process of a typical HMPD system which has a head tracking sensor attached to track a user's head motion. Since this test was performed on a fixed platform for evaluating a user's egocentric depth perception and a head tracking sensor was not necessary, a modified calibration procedure was implemented. As shown in Figure 7.12, the p-HMPD is fixed on the optical bench through two optical posts. The left pupil of the display optics is defined as the origin of the global coordinate and the forward direction is defined as the z axis which is also aligned with a line of holes on the optical bench. The x axis, which is perpendicular to the z axis, is parallel with the optical rail.

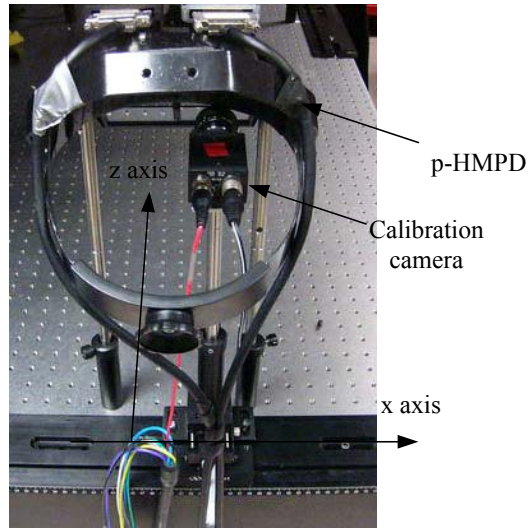


Figure 7.12 Calibration setup

The calibration method was based on the method summarized in chapter 5 (Gao, *et al.* 2003). Since the p-HMPD was fixed, no tracking system was needed in the test. The goal of calibration was to obtain the transformation matrix from EVP (defined in Chapter 5) coordinates of both eyes to the global coordinate with the origin at the left pupil. A calibrated camera was used to obtain the transformation matrix. Similar to the procedure in the chapter 5, the camera was mounted on the optical rail and the entrance pupil of the camera was aligned with the left pupil of the p-HMPD. The orientation of the camera was well adjusted so that the camera coordinate is overlapped with the global coordinate. By taking a picture of the checkerboard displayed through the p-HMPD and using the method described in the chapter 5, the transformation matrix from the EVP of the left eye to camera, $T_{EPV \rightarrow camera}^L$ could be obtained. Since the camera coordinate coincides with the global coordinate, the transformation matrix from the EVP to global coordinate $T_{EPV \rightarrow Global}^L$ could be obtained. Then the camera was moved along the optical rail so

that the entrance pupil of the camera matched with the right eye pupil of the p-HMPD. Similarly the transformation from the EPV of the right eye to the camera, $T^R_{EPV \rightarrow camera}$ could be obtained. Since the transformation from the camera coordinate at the right eye to the global coordinate was a translation matrix with a movement of an IPD value along x axis, the $T^R_{EPV \rightarrow Global}$ can be calculated. With both transformation matrices and the intrinsic parameters of the projection optics, the projected point on the microdisplays could be obtained for any target virtual point within the FOV.

7.2.4.5 Subject

Six subjects between the age of 22 and 26 participated in the test. Screened by a Snellen chart test in the lab, all subjects had normal or correct-to-normal visual acuity for both eyes. All subjects verbally reported at least one 3D movie experience. Before the test, the IPD of each subject was measured and the p-HMPD was adjusted and calibrated based on the measured IPD data so that the error caused by the IPD match would be minimized. The IPD values of six subjects range from 62mm to 67mm. No one had taken LASIK eye surgery. All subjects received \$10/hour compensation for their time.

7.2.4.6 Test procedure

The test was divided into two sessions, with $z_i=1m$ for session 1 and with $z_i=2m$ for session 2. Session 1 was performed in week 1 while session 2 was performed in week 2. For each session, the retroreflective screen was placed at three different distances. Six random permutations of the three different positions were generated and were randomly

assigned to six different subjects. The distance of a real reference object was randomly selected from the 7 positions for each trial. The same reference distance would not be selected consecutively.

Before the test, the participants completed three practice trials so that they could fully understand the task. The reference object distance of the three practice trials were randomly selected within the distance range of the task. A 2-minute break was given to participants after every 35 trials when the retroreflective screen was moved to another distance. The total time for each session is around 1 hour.

7.2.5 Result analysis and discussion

7.2.5.1 Overall performance

Figures 7.13(a) and (b) plot the mean value and the standard deviation of the judged distance as a function of the reference distance for Session 1 and 2, respectively. The broken black line is the reference line which represents the theoretically perfect performance. Through the linear regression analysis, the mean values of the judged distances for session 1 and session 2 can be fit linearly by

$$y = 1.038x - 0.0494 \quad (r^2 = 0.9991)$$

and (7.7)

$$y = 1.198x - 0.2502 \quad (r^2 = 0.9979),$$

respectively, where x is the reference object distance and r^2 is a measure of goodness-of-fit of linear regression.

Distance underestimation and overestimation occurred in both focusing settings. For

Session 1, the results indicate that the distance underestimation occurs in the range of 0.4m to 1.2m and the distance overestimation occurs at the reference distance of 1.6m and perhaps beyond. The reference distance of 1.4m is the transition point between distance underestimation and overestimation. For Session 2, the distance underestimation occurs at the reference distance of 0.8m and 1.2m while the distance overestimation occurs at the range from 1.6m to 3.2m. Using the linear interpolation method, the transition point from underestimation to overestimation is estimated to be 1.4m for both arm-length and mid-range application scenarios. The similar transition has been observed in the previous studies (Swan *et al.* 2007). This transition point could be caused by weaker binocular disparity cue at a larger distance. In our test, HMPD users mainly rely upon binocular disparity cue, relative size of the object and other depth cues to make the judgment. The effectiveness of the binocular cue reduces with the increase of the viewing distance while the effectiveness of the relative size is constant with the distance. It is likely that an observer relies more on the depth due of relative size of a virtual object at a further distance, which may cause the transition from underestimation to overestimation. The over- and under-estimation may also be partially attributed to the accommodation-convergence depth discrepancy in stereoscopic displays. Some recent studies by Liu *et al.* have demonstrated accurate depth perception through a vari-focal plane display which accounted the accommodation-convergence depth discrepancy (Liu, *et al.*2008).

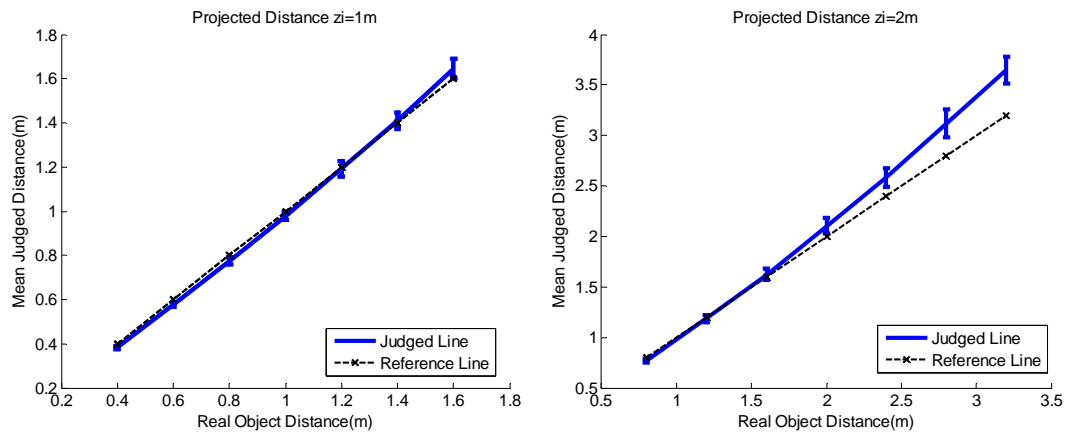


Figure 7.13 Judged distance as a function of reference object distance (a) when $z_i=1\text{m}$ and (b) when $z_i=2\text{m}$

The standard deviation of the judged distance increases with the distance of the reference object. Figure 7.14 (a) and (b) show that the standard deviation increases linearly with the real object distance while $r^2=0.9658$ for Session 1 and $r^2=0.9663$ for Session 2.

In order to further examine the relation between the judged distance and the real object distance, we evaluated the ratio of the judged distance over the real object distance as a function of the real object distance. As shown in Figure 7.15 (a) and (b), the ratio increases linearly with the object distance for both scenarios. In the arm-range scenario, the distance ratio as a function of object distance is given by

$$y = 0.058x + 0.93$$

with $r^2=0.9526$. In the mid-range scenario, the distance ratio as a function of the object distance is given by

$$y = 0.074x + 0.9$$

with $r^2=0.9973$.

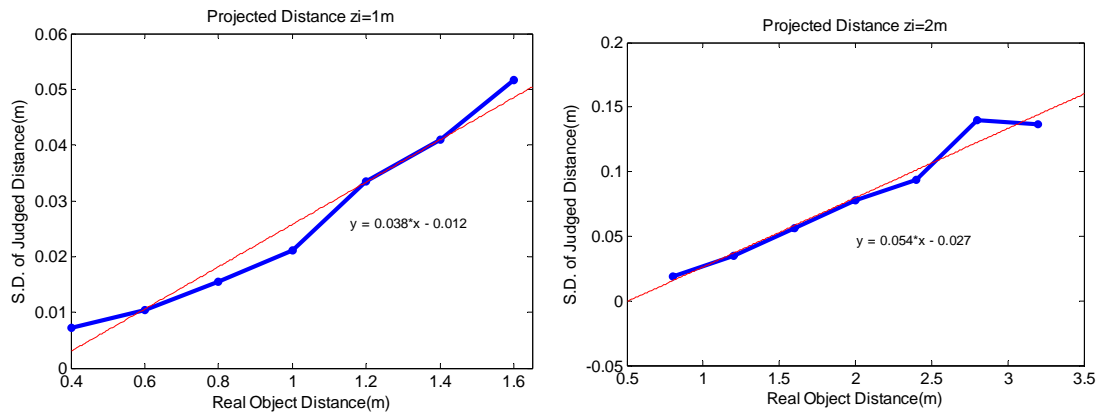


Figure 7.14 Standard deviation of judged distance as a function of real object distance (a) when $z_i=1\text{m}$ and (b) when $z_i=2\text{m}$

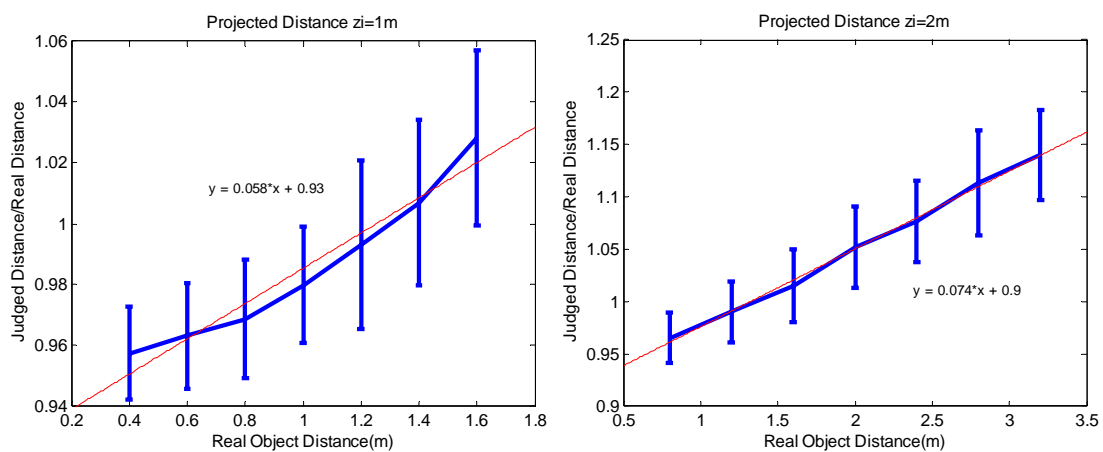


Figure 7.15 Distance ratio as a function of reference object distance (a) when $z_i=1\text{m}$ and (b) when $z_i=2\text{m}$

7.2.5.2 Effect of the retroreflective screen

We further evaluated the effect of a retroreflective screen on a user's depth perception judgment. Figures 7.16 and 7.17 plot the mean value and the standard deviation of the signed error as a function of reference object distance with the retroreflective screen at three different distances for $z_i=1\text{m}$ and $z_i=2\text{m}$, respectively.

In Session 1, as shown in Figure 7.16 (a), the signed error for the screen distance of

0.6m is larger than the results at the other two positions for the reference object distances that are larger than 0.8m. As shown in Figure 7.16 (b), compared with the other two screen positions, the standard deviations of the judged distances at the retroreflective screen position of 0.6m are generally larger, except for the reference object distance of 0.4m. Moreover, the transition from depth underestimation to overestimation can be observed for all three screen positions. The transition point is closer to user when the retroreflective screen is at a closer distance.

A within-subject ANOVA was used to analyze the effects of the screen position on the signed errors. The results show that the screen position does not have a significant effect on the signed error ($F(2,10)=3.25$, $p=0.082$, $N=630$). Furthermore the ANOVA was used to analyze the effect of the screen position at each reference object distance. In Table 7.4, the ANOVA results are listed. It shows that the signed error is significantly affected by the screen position at the reference object distance of 1.4m and 1.6m ($p<0.05$). The Tukey grouping test shows that the signed errors at the screen position of 0.6m are significantly different from the results at the other two screen positions for the reference object distances of 1.4m and 1.6m.

Table 7.4 ANOVA results at different reference object distances

reference distance(m)	0.4	0.6	0.8	1.0	1.2	1.4	1.6
F(2,10) (N=90)	0.84	0.54	1.26	0.77	1.67	7.33	4.6
P	0.4597	0.5979	0.3243	0.4904	0.2376	0.011	0.0383

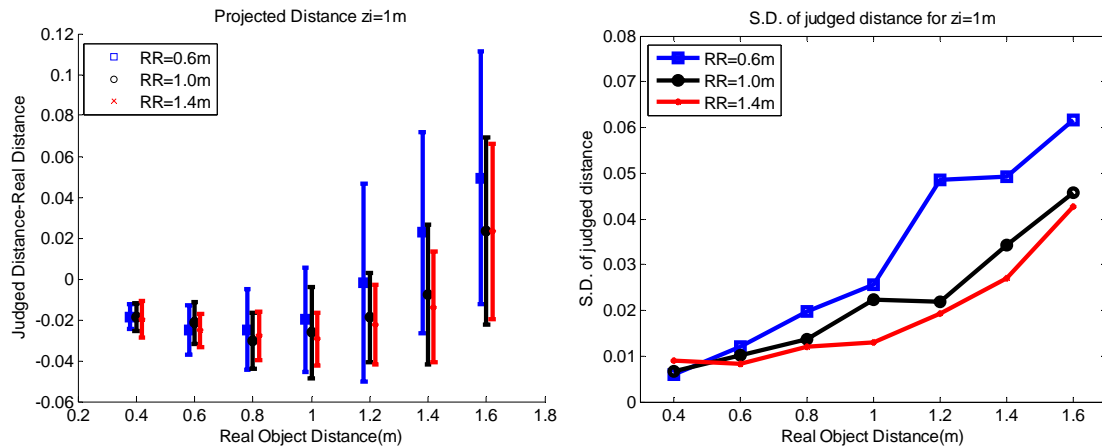


Figure 7.16 (a) Signed error and (b) Standard deviation as a function of real object distance when $z_i=1\text{m}$ (RR: Retroreflective screen)

The analysis results in Session 1 shows that the retroreflective screen might affect the results in two ways. First, due to the scattering effect on the surface of the retroreflective screen, the screen itself can be perceived as an extra depth cue in the depth judgment. Since the depth cue brought by the retroreflective screen does not exist in the real world, it may reduce the consistency of the depth judgment. When the retroreflective screen is closer, the more significant scattering effect could be observed. Thus, the depth cue of a retroreflective screen is stronger when the screen is closer to the user. As we expected, in the test the standard deviations of the judged distance are generally larger when the screen position is at 0.6m. Second, only at the reference object distance of 1.4m and 1.6m, the screen position has a significant effect on the signed error of the depth judgment. This significant effect might be related with the transition point from underestimation to overestimation which is at 1.4m.

Figure 7.17(a) shows the test results in Session 2 with the retroreflective screen at different distances. When the screen is at 1.2m, the signed error is larger than those at the

other two screen positions. Figure 7.17(b) shows the standard deviation of judged distances. In overall, the standard deviation is smaller when the retroreflective screen is at 1.2m. This might be related with the luminance efficiency of the retroreflective screen. Due to the diffraction property of a retroreflective screen, the luminance level is lower when the retroreflective screen is further away, which could lead to less consistent performance in the depth judgment.

A within-subject ANOVA was used to analyze the effect of the retroreflective screen position on the signed errors. The results show that the screen position did not have a significant effect on the signed error ($F(2,10)=2.56$, $p=0.1266$, $N=630$). Furthermore the ANOVA was also used to analyze the effect of the screen position at each reference object distance and the ANOVA results are listed in the Table 7.5. It shows that the screen position effect is significant at the reference distance of 1.2m ($p<0.05$). The Tukey grouping test shows that the results at the screen position of 2.8m are significantly different from those at the other two positions when the reference object distance is 1.2m. At this reference object distance, the average signed errors for the screen position of 1.2m and 2.0m are -0.4mm and -0.8mm, respectively, while the result for the screen position of 2.8m is -23mm. The significant difference between the position of 2.8m and other two positions could be caused by the transition point from underestimation to overestimation. The transition point is around 1.2m for the screen position of 1.2m and 2m while the transition point is 1.6m for the screen position of 2.8m. Thus the differences between the signed errors for the three screen positions become significant around the transition point while such statistically significant difference could not be observed at the other reference

distances.

Table 7.5 ANOVA results at different object distances when $z_i=2\text{m}$

reference distance(m)	0.8	1.2	1.6	2.0	2.4	2.8	3.2
F(2,10) N=90	0.15	8.38	2.17	1.73	2.54	1.5	1.99
P	0.859	0.0073	0.1654	0.2261	0.1279	0.2692	0.1869

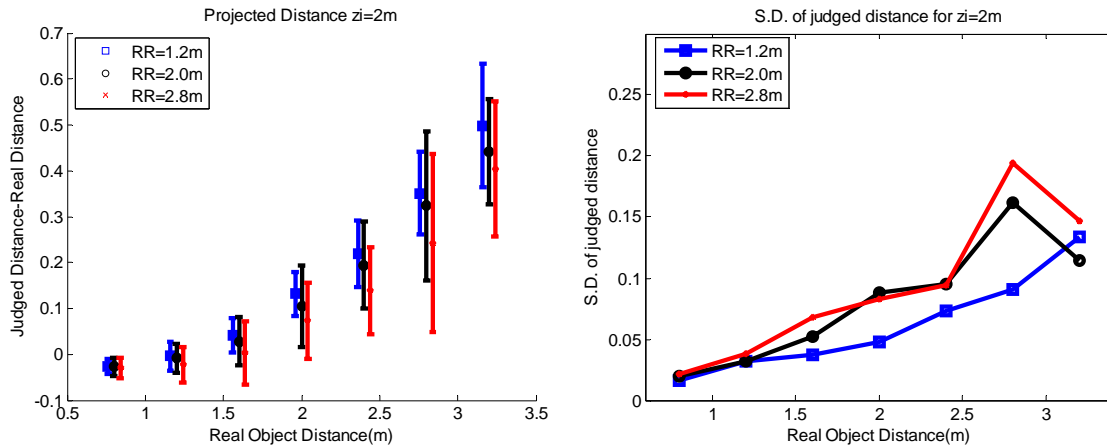


Figure 7.17 (a) Signed error and (b) Standard deviation as a function of reference object distance (RR: Retroreflective screen)

7.2.6 Discussion

The test studied the depth perception accuracy of an HMPD and mainly focused on the effect of the retroreflective screen on the depth perception judgment. To our best knowledge, this test is the first study of the depth perception judgment on an HMPD or p-HMPD in an AR environment. The unique properties of the retroreflective screen make it a difficult task to understand the depth judgment through an HMPD. This test initiates the depth perception study on an HMPD and explores different factors that may affect the depth judgment.

The overall performance of an HMPD was first evaluated without considering the effects brought by the retroreflective screen. It is found that the judged distance increases

linearly with the reference object distance while the standard deviation of the judged distance also increases linearly with the reference object. A transition effect from depth underestimation to overestimation has also been observed around the reference object distance of 1.4m. The effect could possibly be caused by the weaker effectiveness of the binocular disparity cue when the object distance is longer. Further test needs to be done to explore the effect of the binocular disparity cue and the depth cue of relative size on the perceived depth judgment in an AR environment.

Through the comparison of the results at different screen positions for both focusing settings, we found some common effects brought by a retroreflective screen. First, the mean values of the judged distance increase when the retroreflective screen is closer to an HMPD user if the reference object distance that is larger than 0.8m. The test results suggest that a closer retroreflective screen might bring the perceived depth of a virtual object closer, which results in a larger judged depth. Second, there existing a transition point around 1.4m, where depth underestimation switches to overestimation. The transition point varies from 1.2m to 1.6m depending on the position of the retroreflective screen. The position of the retroreflective screen has a significant effect on the signed error of the judged depth around the transition point. Third, the effect of a retroreflective screen on the depth judgment could be different depending on its position. If the retroreflective screen is too close to the observer, i.e. $RR=0.6m$, larger standard deviation of the judged depth can be obtained. It suggests that the depth cue introduced by the retroreflective screen might be more significant due to a stronger scattering effect on the surface of the screen at a closer distance. If the retroreflective screen is too far from the

user, i.e. $RR \geq 2m$, larger standard deviation of the judged depth can also be obtained. The reduced luminance through the screen at a farther distance might result in less consistency in the depth judgment. Lastly, whether or not the retroreflective screen coincides with the focusing plane does not affect the depth perception significantly. In other words, the degradation of the image resolution of a p-HMPD may not reduce the depth perception accuracy significantly. This conclusion matches with the results in previous research, in which it was found that the effect of the display resolution on the depth perception was not significant (Jaeae-Aro & Kjell Dahl, 1997; Thompson *et al.* 2004).

7.2.7 Summary

In this section, the depth perception accuracy through a p-HMPD is evaluated using a perceptual matching method. The overall depth judgment through a p-HMPD is evaluated and characterized. Moreover, the effects of a retroreflective screen on the depth perception judgment are characterized and discussed.

CHAPTER 8

CONCLUSIONS AND SUGGESTIONS OF FUTURE WORK

8.1 CONCLUSIONS

In this dissertation, a polarized head mounted projection display (p-HMPD) using an FLCoS microdisplay technology was developed and evaluated.

The polarization performance through a p-HMPD was characterized using Mueller matrices. Based on the measurement results, the overall display performance, including luminous optical efficiency, contrast, luminance uniformity and color uniformity, was studied and evaluated.

Using a pair of FLCoS microdisplays, we have designed a p-HMPD prototype. The two key elements of a p-HMPD, a compact illumination unit and a compact plastic projection lens, were designed and fabricated. Study was done to mitigate the birefringence effects caused by plastic elements of the projection lens. Following the prototype implementation, a series of calibrations were performed to obtain correct color presentation, desired focusing setting, and optical system characteristics necessary for achieving accurate registration between virtual objects and their counterparts in the real world. Currently, two p-HMPD prototypes are fabricated and used extensively in the research of AR applications and user interface studies in 3DVIS Lab.

The imaging properties of a retroreflective screen, including both geometrical imaging effect and the diffraction effect, were examined, and their effects on the image

resolution of a p-HMPD system were further analyzed. Based on these effects, we have established the movement range of a p-HMPD user from a retroreflective screen, within which the image resolution degradation caused by a retroreflective screen may be neglected. This knowledge is particularly useful for guiding the configuration of an HMPD/p-HMPD system to meet different application needs.

The perceived image resolution of a p-HMDP prototype was evaluated using visual acuity metrics. The test results showed that the perceived resolution degraded when the retroreflective screen was moved further away from the focusing plane. We further explored the effects of different stimuli and different data processing methods on the evaluation results, which help to establish guidelines for designing visual performance assessment with HMDs. Meanwhile, the depth perception test was performed on a p-HMPD. The depth perception accuracy of a p-HMPD was characterized and the effects of the retroreflective screen on the depth judgment were explored.

In summary, a p-HMPD system was developed, studied and evaluated. The work in this dissertation would provide guidance on the future development and evaluation of HMDs. Moreover, the research on the AR applications and user interface studies performed in 3DVIS Lab directly benefit from high performance p-HMPD systems.

8.2 SUGGESTIONS OF FUTURE WORK

In the dissertation, the imaging properties of a retroreflective screen have been studied and an optimal corner cube size was suggested to obtain larger tolerance range. However, the image degradation caused by a retroreflective screen is still a limiting

factor to apply a p-HMPD in AR applications requiring high resolution and large range of user mobility. Moreover, the image degradation of a retroreflective screen is also a limiting factor to design a high performance mobile HMPD (Rolland, *et al.* 2005). As a result, it is desirable to develop a practical and effective method to reduce the image blur caused by a retroreflective screen and to extend the tolerant movement range of a p-HMPD.

The performance of a p-HMPD system is directly related to the image source of the system. With the development of new microdisplay technology and LED technology, the p-HMPD system with better image resolution and higher luminance can be developed by employing microdisplays with higher resolution and LED source with higher luminance.

APPENDIX A

CALCULATION OF THE EFFECTIVE AREA OF A CCR

In the Appendix A, the effective area of a CCR is calculated using a raytracing method. Based on the boundary constraints of a CCR and raytracing results, a set of equations are obtained to define the boundary of an effective aperture of a CCR as a function of incident angle.

Figure A1 illustrates a single CCR, which is an assembly of three reflective surfaces that are mutually orthogonal to each other. The vertex, O , of the corner cube is defined as the origin of the coordinate system while the perpendicular dihedral edges OA , OB , and OC are defined as the X , Y , and Z axis, respectively. The triangle ABC forms the aperture of the corner cube and the side length of the equilateral triangular aperture is denoted as a . A hollow corner cube is assumed for simplicity.

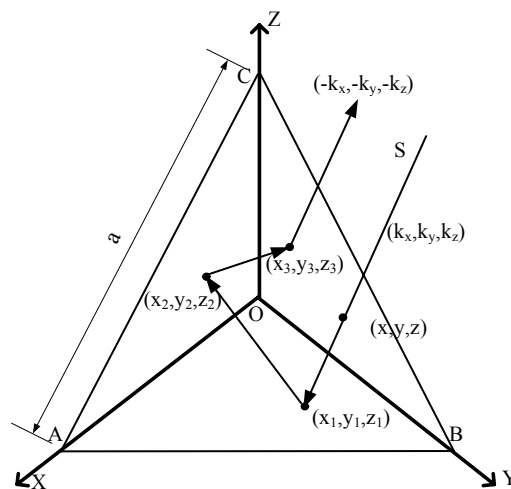


Figure A1. Ray tracing in a corner cube reflector

As shown in Figure A1, incident light with a direction of (k_x, k_y, k_z) is incident on the CCR aperture ABC at point (x,y,z) . k_x , k_y and k_z are defined as cosine of the angle between the incident light and x , y , z axis, respectively, where $k_x < 0$, $k_y < 0$, $k_z < 0$, $x > 0$, $y > 0$ and $z > 0$. There are six possible reflective sequence orders in which a beam of light can pass through a corner cube, with the optical path depending on the direction and position of the incident ray. The following discussion is categorized into six different cases depending on the value of x/k_x , y/k_y and z/k_z .

Path 1: AOB-> AOC->BOC

If the incident light meets the constraint of

$$\frac{z}{k_z} > \frac{y}{k_y} > \frac{x}{k_x}, \quad (\text{A1})$$

the light will be reflected by three planes consecutively following the order of AOB, AOC and BOC. The incident coordinates at three planes are

$$\left(x - \frac{k_x}{k_z}z, y - \frac{k_y}{k_z}z, 0\right) \text{ for plane of AOB,}$$

$$\left(x - \frac{k_x}{k_y}y, 0, -z + \frac{k_z}{k_y}y\right) \text{ for plane of AOC,}$$

$$\text{and } \left(0, -y + \frac{k_y}{k_x}x, -z + \frac{k_z}{k_x}x\right) \text{ for plane of BOC.}$$

Since the three incident points must be constrained within the region of each reflecting surface of the CCR, the following constraints should be met

$$x - \frac{k_x}{k_z}z + y - \frac{k_y}{k_z}z < \frac{a}{\sqrt{2}} \quad (a)$$

$$x - \frac{k_x}{k_y}y - z + \frac{k_z}{k_y}y < \frac{a}{\sqrt{2}} \quad (b) \quad . \quad (A2)$$

$$-y + \frac{k_y}{k_x}x - z + \frac{k_z}{k_x}x < \frac{a}{\sqrt{2}} \quad (c)$$

Since the incident point (x,y,z) is on the aperture plane of the CCR, (x,y,z) should meet the constraint

$$x + y + z = \frac{a}{\sqrt{2}}. \quad (A3)$$

By combining three equations A1, A2 and A3, the following constraints define the effective area for the path 1:

$$\begin{aligned} x &> \frac{k_x}{k_y}y \\ y &> \frac{k_y}{k_z}z \\ x &< \frac{\sqrt{2}k_x}{k_x + k_y + k_z}a. \\ x + y + z &= \frac{a}{\sqrt{2}} \\ x &> 0, y > 0, z > 0 \end{aligned} \quad (A4)$$

Path 2: AOC->AOB-> BOC

If the incident light meets the constraint of

$$\frac{y}{k_y} > \frac{z}{k_z} > \frac{x}{k_x}, \quad (A5)$$

the light will be reflected by three planes consecutively following the order of AOC, AOB and BOC. Similarly with path 1, the following constraints define the effective

area for path 2:

$$\begin{aligned}
 x &> \frac{k_x}{k_z} z \\
 z &> \frac{k_z}{k_y} y \\
 x &< \frac{\sqrt{2}k_x}{k_x + k_y + k_z} a . \\
 x + y + z &= \frac{a}{\sqrt{2}} \\
 x > 0, y > 0, z > 0
 \end{aligned} \tag{A6}$$

Path 3: BOC->AOB-> AOC

If the incident light meets the constraint of

$$\frac{x}{k_x} > \frac{z}{k_z} > \frac{y}{k_y} \tag{A7}$$

the light will be reflected by three planes consecutively following the order of BOC, AOB and AOC. The following constraints define the effective area for the path 3:

$$\begin{aligned}
 y &> \frac{k_y}{k_z} z \\
 z &> \frac{k_z}{k_x} x \\
 y &< \frac{\sqrt{2}k_y}{k_x + k_y + k_z} a . \\
 x + y + z &= \frac{a}{\sqrt{2}} \\
 x > 0, y > 0, z > 0
 \end{aligned} \tag{A8}$$

Path 4: AOB->BOC-> AOC

If the incident light meets the constraint of

$$\frac{z}{k_z} > \frac{x}{k_x} > \frac{y}{k_y}, \quad (\text{A9})$$

the light will be reflected by three planes consecutively following the order of AOB, BOC and AOC. The following constraints define the effective area for the path 4:

$$\begin{aligned} y &> \frac{k_y}{k_x} x \\ x &> \frac{k_x}{k_z} z \\ y &< \frac{\sqrt{2}k_y}{k_x + k_y + k_z} a . \\ x + y + z &= \frac{a}{\sqrt{2}} \\ x &> 0, y > 0, z > 0 \end{aligned} \quad (\text{A10})$$

Path 5: BOC->AOC->AOB

If the incident light meets the constraint of

$$\frac{x}{k_x} > \frac{y}{k_y} > \frac{z}{k_z} \quad (\text{A11})$$

the light will be reflected by three planes consecutively following the order of BOC, AOC and AOB. The following constraints define the effective area for the path 5:

$$\begin{aligned} z &> \frac{k_z}{k_y} y \\ y &> \frac{k_y}{k_x} x \\ z &< \frac{\sqrt{2}k_z}{k_x + k_y + k_z} a \\ x + y + z &= \frac{a}{\sqrt{2}} \\ x &> 0, y > 0, z > 0 \end{aligned} \quad (\text{A12})$$

Path 6: AOC->BOC-> AOB

If the incident light meets the constraint of

$$\frac{y}{k_y} > \frac{x}{k_x} > \frac{z}{k_z}, \quad (\text{A13})$$

the light will be reflected by three planes consecutively following the order of AOC, BOC and AOB. The following constraints define the effective area for the path 6:

$$\begin{aligned} z &> \frac{k_z}{k_x} x \\ x &> \frac{k_x}{k_y} y \\ z &< \frac{\sqrt{2}k_z}{k_x + k_y + k_z} a \\ x + y + z &= \frac{a}{\sqrt{2}} \\ x &> 0, y > 0, z > 0 \end{aligned} \quad (\text{A14})$$

For a parallel beam in the direction of (k_x, k_y, k_z) , the incident aperture can be divided into six regions and light passing through different region has different light path. By combining six regions defined by Equations A4, A6, A8, A10, A12 and A14, the combined effective area is defined as

$$\begin{aligned}
 x &< \frac{\sqrt{2}k_x}{k_x + k_y + k_z} a \\
 y &< \frac{\sqrt{2}k_y}{k_x + k_y + k_z} a \\
 z &< \frac{\sqrt{2}k_z}{k_x + k_y + k_z} a
 \end{aligned} \tag{A15}$$

Taking the light normally incident on the CCR aperture for example, as shown in Figure A2, six regions are formed on the aperture plane of the CCR. The combined effective area is in a hexagon shape and the side length is $\frac{a}{3}$.

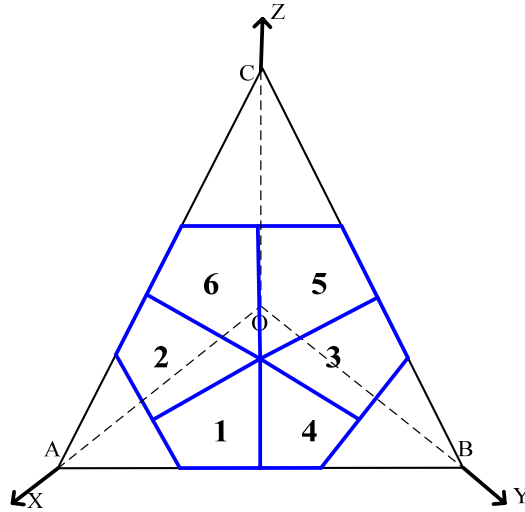


Figure A2. Six sectors on the CCR aperture corresponds to six paths

For a collimating beam, the shape of the effective area of a CCR varies with the incident angle of the beam. The boundary of the effective area is defined by Equation A15 and the boundaries of the CCR aperture. The effective aperture of a CCR can be either in a hexagon shape or a parallelogram shape, depending on the

incident angle.

Case I: If $|k_x+k_y|>|k_z|$ & $|k_y+k_z|>k_x$ & $|k_z+k_x|>k_y$, the effective aperture is in hexagon shape. As shown in Figure A3(a), three side lines of the hexagon effective aperture are the side lines of the triangle aperture while the other three side lines of the hexagon are imposed by the constraints in Equation A15.

The ratio of the effective area over the aperture area is given by

$$P = 1 - \{a^2 + b^2 + c^2\} \quad (A16)$$

$$a = \left(\frac{k_y + k_z - k_x}{k_y + k_z + k_x} \right), b = \left(\frac{k_x + k_y - k_z}{k_y + k_z + k_x} \right), c = \left(\frac{k_x + k_z - k_y}{k_y + k_z + k_x} \right)$$

Since $a+b+c=1$, the maximum value of Ratio P can be obtained when $a=b=c$. Thus, when the light is normally incident onto the aperture plane of the CCR, the effective area reaches its maximum value which is 66.7% of the entire aperture.

Case II: If $|k_x+k_y|<|k_z|$ or $|k_y+k_z|<|k_x|$ or $|k_z+k_x|<|k_y|$, the effective aperture is in parallelogram shape. For this case, two side lines of the parallelogram are the side lines of triangle aperture while the other two side lines are imposed by the constraints in equation A15. Figure A3(b) shows the effective aperture when $|k_x+k_y|<|k_z|$.

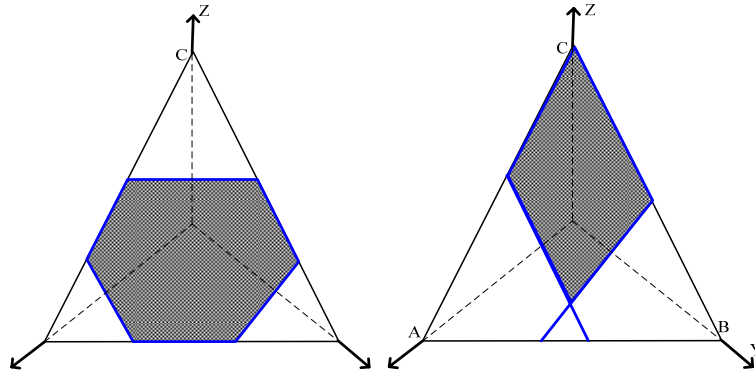


Figure A3. (a) Effective area in Hexagon shape (b) Effective area in parallelogram shape

The area ratio of the effective aperture over the whole aperture is given by

$$P = \begin{cases} \frac{8k_x k_y}{(k_x + k_y + k_z)^2} & \text{if } |k_x + k_y| < |k_z| \\ \frac{8k_z k_x}{(k_x + k_y + k_z)^2} & \text{if } |k_x + k_z| < |k_y| \\ \frac{8k_y k_z}{(k_x + k_y + k_z)^2} & \text{if } |k_y + k_z| < |k_x| \end{cases} \quad (\text{A17})$$

Based on the Equation A16 & A17, the calculation results are plotted as a function of (θ, φ) , which is defined in figure A4(a). An $X'Y'Z'$ coordinate is defined, in which Z' axis passes through the vertex of the CCR and is perpendicular to the aperture plane while Y' axis goes through the point A is vertical to the line BC. The polar angle θ is defined as the angle between the ray and Z' axis while the azimuthal angle φ is the angle between the ray projected on the $X'Y'$ plane and X' axis. The maximum effective aperture is obtained when the light is normally incident on the retroreflective aperture. The maximum area ratio of effective aperture over triangle aperture is 66.7%.

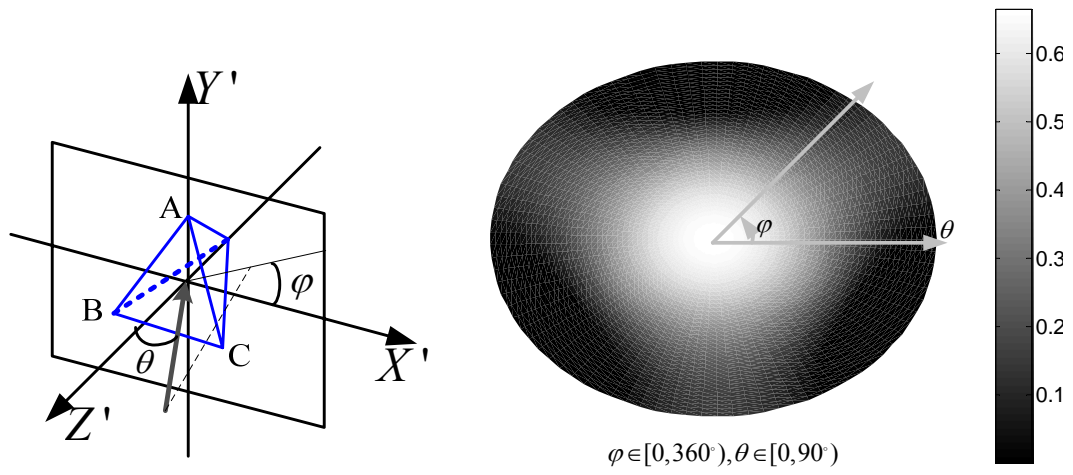


Figure A4 (a) (θ, φ) is defined in the $X'Y'Z'$ coordinate (b) The ratio of the area of the effective aperture to the physical aperture as a function of θ and φ .

REFERENCE

Arditi, A, and Caganello, R., “On the statistical reliability of letter-chart visual acuity measurements,” *Invest Ophthalmol Vis Sci*, 34:120–129, 1993.

Azuma, R., “A Survey of Augmented Reality,” *Presence: Teleoperators and Virtual Environments*, 6(4): 355-385, August 1997.

Barrett, H. H. and Jacobs, S. F., “Retroreflective arrays as approximate phase conjugators,” *Opt. Lett.*, 4: 190-192, 1979.

Baumer, S., “Handbook of plastic optics”, Willey-VCH, Weinheim, 2005.

Bolder Vision Optik, <http://www.boldervision.com/> .

British Standards Institution, Test charts for clinical determination of distance visual acuity — Specification”, BS 4274-1:2003.

Brown, L. and Hua, H., “Magic Lenses for augmented virtual environments,” *IEEE Computer Graphics and Applications*, 26(4), pp.64-73, July/August 2006.

Central Bureau of the CIE, Vienna, Austria, “Colorimetry,” CIE Publication No. 15.2, 1986.

Central Bureau of the CIE, Vienna, Austria, “Industrial color difference evaluation,” CIE Publication No. 116-1995, 1995.

Chang, R., Currie D., and Alley, C., “Far-Field Diffraction Pattern for Corner Reflectors with Complex Reflection Coefficients”, *JOSA* 61(4), pp431-438, 1970.

Chipman, R., “Depolarization index and the average degree of polarization,” *Applied Optics*, 44(13), 2490-2495, 2005.

Chipman, R., Shamir, J., H. Caulfield, J, and Zhou, Q., "Wavefront correcting properties of corner-cube arrays," *Appl. Opt.* 27, 3203-3209, 1988.

Cruz-Neira, C., Sandin, D. J., and DeFanti, T. A., “Surround-screen projection-based virtual reality: the design and implementation of the CAVE”, *Proc. of SIGGRAPH 1993*, ACM Press/ACM SIGGRAPH, New York, NY, USA. 135-142, 1993.

Cutting, J.E., “How the Eye Measures Reality and Virtual Reality”, *Behavior Research Methods, Instrumentation, and Computers*, 29, pp. 29–36, 1997.

CVI Melles Griot, <http://www.cvimellesgriot.com/>

Daniel, K., "Speed May Give Ferroelectric LCOS Edge in Projection Race," *Display Devices Fall '05*, 2005.

DeBoo, B., Sasian, J. and Chipman, R., "Depolarization of diffusely reflecting man-made objects" *Applied Optics*, 44(26), 5434-5445, 2005.

Howard I.P. and Rogers B.J., "Depth Perception", *Seeing in Depth*, Vol. 2, I. Porteus, Ontario, Canada, 2002.

Eckhardt, H., "Simple Model of Corner Reflector Phenomena," *Applied Optics*, Vol. 10-7, pp. 1559-1566, 1971.

Ellis, S.R. and Menges, B.M., "Localization of Virtual Objects in the Near Visual Field", *Human Factors*, 40(3), September, 1998.

Emagin, www.emagin.com

Ferguson, J., "Optical system for head mounted display using a retro-reflector and method of displaying an image," U.S. patent 5,621,572, April 15, 1997.

Fidopiastis, C., Fuhrman, C., Meyer, C. and Rolland J., "Methodology for the iterative evaluation of prototype head-mounted displays in virtual environments: Visual acuity metrics," *Presence: Teleoperators and Virtual Environments*, 14(5):550-562, October 2005.

Fisher, R., "Head-mounted projection display system featuring beam splitter and method of making same," US Patent 5,572,229, 1996.

Foley, J. M., "Stereoscopic Distance Perception", in SR ELLIS, M KAISER, AJ GRUNWALD (EDS), *Pictorial Communication in Virtual and Real Environments* (2nd Ed), Taylor & Francis, 1991.

Forth Dimensional Displays Limited, <http://www.forthdd.com>.

Fisher, R., "Head-mounted projection display system featuring beam splitter and method of making same," US Patent 5,572,229, 1996.

Fresnel Technologies, Inc., <http://www.fresneltech.com>.

Gleckman P., "Light source utilizing diffusive reflective cavity", US patent 6,043,591, Mar. 28, 2000.

Gao, C., Hua H., and Ahuja, N., "Easy calibration of a head-mounted projective display for augmented reality systems," *Proceedings of IEEE VR 2003*, Los Angeles, CA, March 2003.

Ha, Y., Hua, H., Martins, R. and Rolland, J. P. "Design of a wearable wide-angle projection color display" *Proceedings of SPIE 4832*, 67-73, (2002).

Haschberger, P. and Tank, V., "Optimization of a Michelson interferometer with a rotating retroreflector in optical design, spectral resolution, and optical throughput," *J. Opt. Soc. Am. A* 10, 2338–2345 (1993).

Howard, I.P.; Rogers, B.J. *Binocular Vision and Stereopsis*; New York: Oxford, 1995.

Hua, H., Girardot, A., Gao, C. and Rolland, J. P., "Engineering of head-mounted projective displays". *Applied Optics*, 39 (22), pp.3814-3824 (2000).

Hua, H., Gao, C., Biocca, F. and Rolland, J. P., "An Ultra-light and Compact Design and Implementation of Head-Mounted Projective Displays", *Proc. of IEEE-VR 2001*, 175-182, 2001.

Hua, H., Gao, C. and Rolland, J. P., "Study of the imaging properties of retro-reflective materials used in head-mounted projective displays," *Proceedings of SPIE (Aerosense 2002)*, Vol. 4711, pp.194-201, 2002.

Hua, H., Brown, L. and Gao, C., "A new collaborative infrastructure: SCAPE," in *Proceedings of IEEE VR 2003* (IEEE, 2003), pp. 171–179, 2003

Hua, H., Ha, Y., and Rolland, J. P., "Design of an ultra-light and compact projection lens," *Applied Optics*, 42(1), 1-12, 2003.

Hua, H., Brown, L. and Gao, C., "SCAPE: supporting stereoscopic collaboration in augmented and projective environments," *IEEE Computer Graphics Applications*, 24, 66–75, 2004.

Hua, H. and Gao, C., "A Polarized Head-Mounted Projective Display," *ACM International Symposium on Mixed and Augmented Reality*, 32- 35, (2005).

Hua, H., "Merging the worlds of atoms and bits: augmented virtual environments," *Optics and Photonics News*, 17(10), 26-33, October 2006.

Hua, H. and Gao, C., "Design of a bright polarized head-mounted projection display" *Applied Optics*, 46(14), 2600-2610, 2007.

Hua, H., Gao, C and Ahuja, N., "Calibration of an augmented reality system using

head-mounted projective displays,” *IEEE Transactions on Systems, Man, Cybernetics* (Part A: Systems), 37(3), 416-30, May 2007.

Imatest, <http://www.imatest.com>.

Inami, M., Kawakami, N., Sekiguchi, D., Yanagida, Y., Maeda, T. and Tachi, S., “Visual-haptic display using head-mounted projector,” *Proceedings of IEEE Virtual Reality 2000*, pp. 233– 240, 2000.

Inami, M., Kawakami, N. and Tachi, S., “Optical camouflage using retro-reflective projection technology,” *Proceedings of ISMAR 2003* (ISMAR, 2003), pp. 348 –349, 2003.

Jaeae-Aro, K. and Kjelldahl, L., “Effects of Image Resolution on Depth Perception in Stereo and Non-Stereo Images.” *Stereoscopic Displays and Applications VIII*, 3012 (February 1997).

Jones, A., Swan II J. E., Singh, G., and Kolstad E., “The Effects of Virtual Reality, Augmented Reality, and Motion Parallax on Egocentric Depth Perception”, *Proceedings of IEEE Virtual Reality 2008*, pp. 267–268, March 2008.

Kawakami, N., Inami, M., Sekiguchi, D., Yangagida, Y., Maeda, T. and Tachi, S., “Object-oriented displays: a new type of display systems—from immersive display to object-oriented displays,” in *Proceedings of IEEE SMC 1999, IEEE International Conference on Systems, Man, and Cybernetics*, Vol. 5, pp. 1066 –1069.

Kijima, R., and Ojika, T., 1997, “Transition between virtual environment and workstation environment with projective head-mounted display”, *Proc. of IEEE VR 1997*, Los Alamitos, CA, USA, 130-137, 1997.

Kim, H. and Lee, B., Optimal design of retroreflection corner-cube sheets by geometric optics analysis, *Optical Engineering* 46(09), 2007.

Kirkley, S., Augmented Reality Performance Assessment Battery (ARPAB), PhD Dissertation, Instructional Systems Technology, Indiana University, 2003.

Lampton, D.R., Knerr, B. W., Goldberg S. L., Bliss, J. P., Moshell, J. M. and Blau, B. S., “The virtual environment performance assessment battery (VEPAB): Development and evaluation”, *Presence: Teleoperators and Virtual Environments*, 3(2):145–157, 1994.

Loomis, J. M., and Knapp, J. M., “Visual perception of egocentric distance in real and virtual environments,” *Virtual and Adaptive Environments: Applications, Implications, and Human Performance Issues*, L. J. Hettinger and J. W. Haas, Eds. Lawrence Erlbaum Associates, Mahwah, NJ, USA, 21–46, 2003.

Livingston, M. A., "Quantification of visual capabilities using augmented reality displays", *The IEEE and ACM International Symposium on Mixed and Augmented reality (ISMAR 2006)*, 2006,

Liu, J. and Azzam, R. M. A., "Polarization properties of cornercube retroreflectors: theory and experiment," *Appl. Opt.* 36, 1553–1559 (1997).

Liu, S., Cheng, D. and Hua, H. "An Optical See-Through Head Mounted Display with Addressable Focal Planes." *The seventh IEEE and ACM International Symposium on Mixed and Augmented reality (ISMAR 2008)*, Cambridge, UK, Sept 2008.

Lu, S. and Chipman, R., "Interpretation of Mueller matrices based on polar decomposition," *J. Opt. Soc. Am. A*, 13, 1106-1113, 1996

Melzer, J. and Moffitt, K., "Head mounted displays: designing for the user", McGraw-Hill, 1997

3M: <http://www.mmm.com>

Minato, A. and Sugimoto, N., "Design of a four-element, hollow-cube-corner retroreflector for satellites by use of a genetic algorithm," *Appl. Opt.* 37, 438–442 (1998).

Moxtek, inc., <http://www.moxtek.com/>

National Academy of Science National Research Council (NASNRC). Recommended standard procedures for the clinical measurement and specification of visual acuity. Report of working group 39. *Adv Ophthalmol* 1980;41 103-48.

Nanba, N., "Objective lens and image pickup device using the same", US patent 6,236,521, May 22, 2001.

O'Brien, D. C., Faulkner, G. E., and Edwards, D. J., "Optical Properties of a Retroreflecting Sheet," *Appl. Opt.* 38, 4137-4144 (1999).

Optical Research Associate, <http://www.opticalres.com>

Palmer, D. A., "Retroreflective materials and optical imaging," *Appl. Opt.* 24, 1413-1414 (1985)

Parsons, J. and Rolland, J. P., "A non-intrusive display technique for providing real-time data within a surgeons critical area of interest," *Proceedings of Medicine Meets Virtual Reality 1998 (1998)*, pp. 246–251, 1998

Pinkus, P. and Task, H. L., "Measuring Observers' Visual Acuity Through Night Vision Goggles", ASC98-1884, 1998

Pinkus, P. and Task, H. L., "Reproducibility of Night Vision Goggle Visual Acuity Measurements Using Landolt C's", ASC99-2057, 1999

Pister, K. S. J., Gunawan, D. S., and Lin, L., "Micromachined corner cube reflectors as a communication link," *Sens. Actuators A* 46–47, 580–583, 1995.

Plumert, J.M., Kearney J.K., Cremer J.F., and Recker K., "Distance Perception in Real and Virtual Environments", *ACM Transactions on Applied Perception*, 2(3), 2004.

Poizat, D. and Rolland, J. P., "Use of Retro-reflective Sheets in Optical System Design," Technical report TR98-006, 1998

Ricci, F., Cedrone, C. and Cerulli, L., "Standardized measurement of visual acuity," *Ophthalmol Epidemiol* 5: 41–53, 1998.

Rolland J. P., Biocca F., Hamza-Lup, F., Ha, Y., and Martins, R., "Development of head-mounted projection displays for distributed, collaborative, augmented reality applications," *Presence: Teleoperators and Virtual Environments* 14, 528 –549, 2005..

Rolland, J.P., Gibson, W., Ariely, D., "Towards Quantifying Depth and Size Perception in Virtual Environments", *Presence*, 4(1), pages 24–49, 1995.

Rolland, J.P. and Arthur, K. "Study of Depth Judgments in a See-Through Mounted Display" *Proceedings of the SPIE, Aerosense*, 3058, 66-75, 1997.

Rolland, J. P. and Hua, H., "Head-mounted displays," in *Encyclopedia of Optical Engineering*, R. Barry Johnson and Ronald G. Driggers, Eds, 2005.

Robinson, M., Chen, J., and Sharp, G., *Polarization Engineering for LCD Projection*. John Wiley & Sons, Ltd. England, 2005

Ruda, M. C., Stuhlinger, T. W. and Garcia, K. J., "Solid state light engine optical system", US patent application 20050036119, Feb.17, 2005.

SAYANA K., "Pinhole Imagery", *JOSA*, Vol. 57, No. 9, 1967

Schwiegerling, J., *Field Guide to Visual and Ophthalmic Optics*, SPIE press, 2004

Segre, S. E. and Zanza, V., "Mueller calculus of polarization change in the cube-corner retroreflector," *J. Opt. Soc. Am. A* 20, 1804-1811, 2003.

Sharma, G., "LCDs Versus CRTs—Color-Calibration and Gamut Considerations", *Proc. of the IEEE*, Vol. 90, No.4, pp. 605-622, April 2002.

Sloan, L.L., "New test chart for the measurement of visual acuity at far and near distance", *Am J Ophthalmol*, 48:807-13, 1959

Stokes, M., Anderson, M., Chandrasekar, S. and Motta, R., "A Standard Default Color Space for the Internet – sRGB" <http://www.w3.org/Graphics/Color/sRGB>, 1996.

Sugihara T., et al, "An evaluation of Visual fatigue in 3D displays: focusing on the mismatching of convergence and accommodation," *IEICE Trans on Electronic Displays*, Vol. 82-E, No.10, 1999.

Swan II, J. E., Livingston, M. A., Smallman, H. S., Brown, D., Baillot, Y., Gabbard J. L., and Hix, D., "A Perceptual Matching Technique for Depth Judgments in Optical, See-Through Augmented Reality", *Proc. of IEEE VR 2006*, pp. 19–26, 2006.

Swan II, J. E., Jones, A., Kolstad, E., Livingston, M. A., and Smallman, H. S., "Egocentric depth judgments in optical, see-through augmented reality", *IEEE Transactions on Visualization and Computer Graphics (TVCG)* 13, 3, 429 – 442, 2007.

Teledyne Lighting & Display Products, <http://www.teledynelighting.com/>

Texas Instrument, <http://www.ti.com>

Thompson, W.B., Willemsen, P, Gooch, A.A., Creem-regehr, S.H, Loomis, J.M., Beall, A.C., "Does the Quality of the Computer Graphics Matter when Judging Distances in Visually Immersive Environments?", *Presence: Teleoperators & Virtual Environments*, 13(5), October 2004.

Witmer, B. G and Sadowski, W, "Nonvisually guide locomotion to a previously viewed target in real and virtual environments", *Human Factors* 40, 3, 478–488, 1998

Zhou, G., Alfrey, A., and Casperson, L. W., "Modes of a laser resonator with a retroreflecting corner cube mirror," *Appl. Opt.* 21, 1670–1674 (1982).

Zhang, R., Hua, H., "Design of a polarized head-mounted projection display using FLCOS microdisplays," *Proceedings of SPIE* 6489, 64890B (2007).

Zhang, R., Hua, H., "Characterizing polarization management in a p-HMPD system," *Applied Optics*, 47(5):1-11, February 2008

Zhang, R. and Hua, H., "Design of a polarized head-mounted projection display using ferroelectric liquid-crystal-on-silicon microdisplays," *Applied Optics*, 47(15), pp.

2888-2896, April 2008

Zhang, R., Hua, H., "Design of a Compact Light Engine for FLCOS Microdisplays in a p-HMPD System," Society for Information Display 2008 International Symposium, *Seminar and Exhibition (SID2008)*, Los Angeles, CA, May 2008

Zhang, R., Hua, H., "Imaging Quality of a Retroreflective Screen in Head Mounted Projection Displays," *JOSA A*, A 26, 1240-1249, May 20, 2009